# Nonlinear Optimal Control for Aircraft Ground Manoeuvres

by
Zexin Huang

**A Doctoral Thesis**

Submitted in partial fulfilment of the requirements for the award of
Doctor of Philosophy of Loughborough University



April 2019

# Abstract

Despite recent advances in flight control systems, aircraft ground manoeuvres are still conducted manually. This thesis aims to improve the efficiency and safety of airport operations by developing a real-time optimal controller for ground operations, especially high-speed runway turnoff. A reliable and robust controller is able to improve airport traffic capacity and reduce runway events of incursion, excursion, and confusion.

A high-fidelity fully-parameterised aircraft model is developed to capture aircraft ground dynamics. The nonlinearities enter the system via sub-models of tyres and aerodynamics. A numerical continuation method is used to compute and track steady-state solutions under the variation of parameters, providing a global picture of the system stability within a typical operation envelop. Dynamic simulations are carried out to analyse transient behaviours which are not captured by the bifurcation analysis.

Three controllers are employed to investigate the automation of aircraft runway exit manoeuvres. An Expert Pilot Model is developed to represent manoeuvres that are manually operated by pilots. To evaluate the optimality of the proposed Expert Pilot Model (EPM), Generalised Optimal Control (GOC) is employed to numerically investigate the optimal solutions for aircraft runway exit manoeuvres. A formal solution of real-time optimal steering control problem is desired in light of the gap between the Expert Pilot Model and Generalised Optimal Control. Therefore, Predictive Steering Control is developed based on Linear Quadratic method with lookahead, which is able to deliver near-optimal manoeuvres.

# Acknowledgements

I would like to thank my supervisors, Dr. Matt Best and Dr. James Knowles, for their continued support and encouragement. Without their guidance and expertise this PhD would not have been possible. They led the way for me, being patient and insightful throughout. During my time with the Aeronautical & Automotive Engineering Department I have made too many friends to mention, safe to say I couldn't have done it without you. Thanks to everyone that made my time in Loughborough so unique. I would like to thank my family in China and in the United Kingdom, who have been right behind me every step of the way. Lastly, I would like to thank my beloved wife Dandan for her patience and company: a massive thank you.

# Contents

# List of Figures

# Nomenclature

| | |
|---|---|
| $\alpha_{N,R,L}$ | slip angle of the nose, right and left gear |
| $\alpha_{optN,R,L}$ | optimal slip angles of the nose, right and left gear |
| $\beta$ | aerodynamic slip angle |
| $\delta$ | steering angle |
| $\delta_{zN,R,L}$ | vertical tire deflection |
| $\mu_{xR,L}, \mu_{yR,L}$ | coefficient of friction of main-gears |
| $\Omega_R, \Omega_L$ | angular velocity of mean-gears |
| $\psi, \theta, \varphi$ | yaw angle, pitch angle and roll angle of the aircraft |
| $\rho$ | air density |
| $c_{rr}$ | coefficient of rolling resistant |
| $C_{xR,L}, C_{yR,L}$ | corning stiffness of main-gears |
| $c_{zM}$ | damping coefficient of the main-gear |
| $c_{zN}$ | damping coefficient of the nose-gear |
| $CG$ | aircraft centre of gravity |
| $d_L$ | signed deviation from the target path |

| | |
|---|---|
| $F_{rR,L}$ | resultant normalized friction force of main-gears |
| $F_{xA}, F_{yA}, F_{zA}$ | aerodynamic force components at the aerodynamic centre of the aircraft |
| $F_{xL}, F_{yL}, F_{zL}$ | tyre/ground force components on left-gear |
| $F_{xN}, F_{yN}, F_{zN}$ | tyre/ground force components on nose-gear |
| $F_{xR}, F_{yR}, F_{zR}$ | tyre/ground force components on right-gear |
| $F_{xTR}, F_{xTL}$ | right and left engine thrust force |
| $F_{ymaxN,R,L}$ | maximum lateral force of the nose, right and left gear |
| $F_{zW}$ | aircraft weight at the centre of gravity |
| $I_{MG}$ | moment of inertia of mean-gears |
| $I_{xx}, I_{yy}, I_{zz}$ | aircraft's moment of inertia |
| $k_{R,L}$ | combined slip of main-gears |
| $K_{ug}$ | understeer gradient |
| $k_{zM}$ | stiffness coefficient of the main-gear |
| $k_{zN}$ | stiffness coefficient of the nose-gear |
| $L$ | aircraft wheelbase |
| $l_{mac}$ | mean aerodynamic chord |
| $l_{xA}$ | x-distance to the aerodynamic centre |
| $l_{xN}$ | x-distance to the nose gear |
| $l_{xR,L}$ | x-distance to the right/left gear |
| $l_{xT}$ | x-distance to the thrust centre |

| | |
|---|---|
| $l_{yR,L}$ | y-distance to the right/left gear |
| $l_{yTR,L}$ | y-distance to the thrust centre |
| $l_{zA}$ | z-distance to the aerodynamic centre |
| $l_{zN}$ | z-distance to the nose gear |
| $l_{zR,L}$ | z-distance to the right/left gear |
| $l_{zT}$ | z-distance to the thrust centre |
| $m$ | aircraft total mass |
| $M_{xA}, M_{yA}, M_{zA}$ | aerodynamic moments at the aerodynamic centre of the aircraft |
| $R_{wheel}$ | wheel radius of the main-gear |
| $S_w$ | aircraft wing area |
| $S_{R,L}$ | slip ratio of main-gears |
| $T_p$ | preview time |
| $T_{brake}$ | brake torque applied on mean-gears |
| $V_x, V_y, V_z$ | aircraft translational velocities |
| $V_{xG}, V_{yG}, V_{zG}$ | aircraft translational velocities in the ground coordinate system |
| $V_{xL}, V_{yL}, V_{zL}$ | left-gear velocity components in the local tyre coordinate system |
| $V_{xN}, V_{yN}, V_{zN}$ | nose-gear velocity components in the local tyre coordinate system |

| | |
|---|---|
| $V_{xR}, V_{yR}, V_{zR}$ | right-gear velocity components in the local tyre coordinate system |
| $W_x, W_y, W_z$ | aircraft angular velocities |
| $W_{xG}, W_{yG}, W_{zG}$ | aircraft angular velocities in the ground coordinate system |
| $X, Y, X$ | global position of aircraft centre of gravity |

# Chapter 1

# Introduction

## 1.1 Research motivation and objectives

Recent years have seen a rapid increase in air passengers, yet their numbers are predicted to double to 7.8 billion by 2036 according to The International Air Transport Association (IATA) [1]. It is a huge challenge for airports and airlines to improve existing aviation infrastructure and meet this essential demand over the next two decades. Whilst great emphasis has been placed on navigation and automation in flight, aircraft ground manoeuvres are still made solely based on visual perception, with taxiing systems (thrust, steering and braking) operated manually by pilots. Conducting these manoeuvres manually leaves this phase of an aircraft's journey vulnerable to human errors. A recent study of commercial aviation accidents shows that 11% of all fatal accidents occurred when the aircraft was on the ground [2]. Additionally, other non-fatal ground-based incidents typically lead to long delays, costing airlines money as planes are grounded for longer than planned. Despite the impact of fatal and non-fatal ground-based incidents, they still occur frequently: the International Air Transport Association (IATA) recorded 50 accidents over the period 2010-2014 [3]; the International Civil Aviation Organization (ICAO) found that 90% of scheduled commercial air transport accidents from 2008-

2016 were runway-based.

A reliable automation of ground manoeuvres could help to reduce this significant contributor to aviation incidents. Automated ground manoeuvres could improve the efficiency, safety and reliability of airport operations under different weather and road conditions. A highly reliable and robust controller would allow more stable and efficient ground manoeuvres than a pilot could achieve. In addition, there are associated economic benefits; for example the occupation time of the runway for each aircraft could be minimized so as to increase airport traffic capacity. In view of this, the overall objective of this research is to design a real-time optimal controller to automate aircraft ground manoeuvres, specifically high-speed runway turnoff.

The design of controllers heavily relies on the knowledge of aircraft ground dynamics. The applicability of control strategies to real-life applications depends on the accuracy of the model. Therefore, a high-fidelity aircraft model is essential for the controller design and verification. Since nonlinear effects are known to play a significant role in the aircraft ground dynamics [4, 5], a 6 Degrees-of-Freedom (DOF) nonlinear model is needed to capture these nonlinearities accurately. To simulate movement of a pilot-controlled aircraft, and more importantly, to gain better understanding of how a pilot normally conducts a runway exit manoeuvre, we aim to develop a pilot model that represents an expert pilot. This pilot model provides one possible solution for aircraft ground manoeuvring control despite not being an optimal controller. To evaluate the optimality of the pilot model and any other controllers designed in the future, we also implement an off-line optimal controller, which can be used to numerically investigate the actual optimal solution for specific ground manoeuvres. The optimal controller does not need to be implemented in real-time as long as it shows good convergence; its solution provides a benchmark against which the effectiveness of a controller may be judged. The ultimate goal of this work is to develop an optimal controller that is suitable for real-time implementation, and also stable in the presence of disturbances and uncertainties.

## 1.2 Review of existing work

Modern aircraft are increasingly reliant on sophisticated flight computers to aid and protect aircraft in flight. Over the past forty years, the spectrum of flight control has greatly expanded from the original concept of mechanical control linkages and autopilot to the multi-disciplinary control integration. Fly-by-wire is a system that replaces conventional manual flight controls with an electronic interface [6, 7, 8]. It interprets the pilot's control input as a desired outcome and calculates the control surface activities required to deliver the outcome via different combinations of rudder, elevator, aileron, flaps and throttle. The fly-by-wire system continually stabilises the aircraft and adjusts its flying characteristics to prevent the aircraft operating outside of its safe performance envelope. Two aircraft manufacturers, Airbus and Boeing, produce commercial passenger aircraft with flight computers that can perform under different flight control modes, e.g. normal, alternate, direct and mechanical mode. Each mode has different sub-modes, e.g. ground mode, flight mode, flare mode, back-up mechanical mode. These sub-modes depend on the stage of flight, including taxiing, take-off, climb, cruise, descent, flare, and landing [6, 7, 8]. In ground mode, there is a direct response of the elevators to the sidestick input. The horizontal stabiliser is set to 4° up until the wheels leave the ground, and then flight mode takes over from ground mode. Flight mode is operational from take-off to shortly before landing. It provides five types of protection: pitch attitude, load factor limitations, high speed, high angle of attack (AOA) and bank angle. When the radar altimeter indicates 100 feet above ground, flare mode is automatically engaged, providing high-AOA protection and bank angle protection.

While fly-by-wire is already a mature technology, limited attention has been paid to the control of aircraft when on the ground. An automatic wheel-based hydraulic brake system, Autobrake, is available on advanced aircraft [9]. It is normally enabled during landing and takeoff, when the aircraft's longitudinal deceleration is handled automatically. One of the main advantages of engaging

the autobrake as opposed to manually pressing on brake pedals is the uniform deceleration mechanism. The aircraft automatically decelerates at the selected level using a variety of braking methods, such as thrust reversers or spoilers.

Currently, there is no existing automatic control system available for aircraft ground manoeuvres, however, plenty of control strategies offer potential methods to address this problem. Model predictive control (MPC) has been used in a wide range of advanced control systems in vehicle applications. Lenain et al. use an MPC approach to follow a path with high accuracy [10], where a control law is designed to correct vehicle behavior in the presence of sliding. The proposed controller is able to compensate for different delays due to actuators and inertial effects. Faulwasser et al. present a nonlinear model predictive control (NMPC) framework to design a controller for output path following problems under constraints on states and control inputs [11]. The geometric nature of path following is investigated for nonlinear systems based on the transverse normal forms, which are used to stabilise terminal regions and end penalties. Since the aircraft model in this research is a highly nonlinear and complex dynamical system, MPC may become computationally expensive and hence difficult to implement for real-time applications.

An alternative approach, also widely implemented for motion control in vehicles, is the linear quadratic (LQ) method. Unlike in MPC where the control input is optimized in a closed-loop system, in the LQ method the optimal control sequence can be directly obtained from full state feedback. Cole et al. present a preview-based LQ controller for reference-tracking motion control, which is able to balance tracking performance effectively with available actuation capacity in an automotive application [12]. The optimal feed-forward solution is applied to the feedback controller independently using a polynomial/spectral factorization formulation. Sharp et al. present a structure for optimal linear car steering control problems using the LQ method joined with a road preview model [13][14]. The road preview data observed by the driver is updated via a shift register operation; in this way the path information enters the system, incorporated with the vehicle's dynamic model.

In order to develop a real-time optimal controller, a realistic aircraft model is needed for the purpose of prediction and test. To evaluate the effectiveness of a controller, a pilot model illustrates typical operations of a human pilot; in addition, a numerical optimal controller provides the best possible solution for a specific manoeuvre. The rest of the literature review is organised as follows: existing aircraft models are reviewed in section 1.2.1; driver models that are suitable for an aircraft application are introduced in section 1.2.2; optimal control theory and potential control methods are discussed in section 1.2.3; a summary is given in section 1.2.4.

### 1.2.1 Aircraft Mathematical Model

Mathematical modelling and simulation is widely used in engineering disciplines due to its relative low cost and risk. It helps to explain a system and to study the effects of different components, and to make predictions about behaviour. The application of multibody system methods is well established in a large number of engineering fields of research including vehicle dynamics [15, 16] and aerospace engineering [17, 18]. The advantage of multibody system software packages, such as ADAMS [15] and SimMechanics [19], is that models can be developed, validated and simulated within a complete framework provided by the software. Khapane [20] presents a simulation of an asymmetric landing case and typical ground manoeuvres for large transport aircraft which is modelled as a multibody system in the simulation tool SIMPACK. In a standard rolling case with a curved path, it is able to calculate the lateral forces on the tyres using this model. Coetzee et al. present a study of the turning characteristics as determined from a simplified three-dimensional and nonlinear SimMechanics Model of the Airbus A320 [21]. The specific aim of their analysis is to see what effects the tyres, oleos and aerodynamics have on the dynamic behaviour of an aircraft model.

Thanks to the white-box nature, a physics-based mathematical model provides full accessibility to all system states and intermediate variables. Part

of the challenge facing researchers working on aircraft ground control is that there is a limited number of aircraft mathematical models that have been developed in the literature. Rankin et al. present a 6-DOF nonlinear model for aircraft ground dynamics [22], where nonlinearities are included in the lateral tyre dynamics, aerodynamics and shock absorber dynamics. The model is derived from the GARTEUR model [23], an industrially-validated SimMechanic model which is known to produce accurate representations of aircraft ground dynamics. Rankin et al. use their model to conduct a comprehensive bifurcation analysis of the aircraft lateral dynamics [24], highlighting how boundaries associated with the lateral stability of steady-state turning solutions vary with operational parameters such as thrust level and CG position.

Since nonlinearities are known to play a significant role in aircraft ground dynamics, it is important to incorporate them as part of the model. Nonlinear effects enter the system via specific properties of components, such as tyres and aerodynamics; particularly, the tyre/ground forces have a dominant effect over aerodynamic forces when the aircraft is taxiing at lower speeds. Tubeless radial tyres are generally used for aircraft in view of their improved failure characteristics over bias-ply tyres [25]. To investigate ground dynamics, a GARTEUR action group developed a tyre model to calculate force elements acting on the tyres [23]. It is a simplified model with quadratic functions fitting the measured maximum lateral force and optimal slip. Another basic and easily obtainable representation of tyre characteristics is provided by the Fiala tyre model, which is generally used in automotive applications [26, 27]. This model uses an empirical formulation which requires 10 parameters to represent the force elements. The parameters can be easily and rapidly obtained from measured tyre test data without using special software. A disadvantage of these models is that they do not deal with combined braking and cornering. Alternatively, the Magic Formula tyre model resulting from the widely recognised work of Pacejka et al. [28, 29, 30, 31] represents the tyre forces as functions of either longitudinal slip for tractive forces or slip angle for lateral forces. The traction circle is a way of decomposing the total grip on a specific

tyre [25]. The resultant force falls within the traction circle and reaches a maximum at the circle boundary. This model is most established among the existing empirical models and is widely used by both industry and academia. More recently, Wood et al. presented a low parameter tyre model which is able to produce highly representative results when compared to aircraft tyre test data [32]. It is specifically intended to replicate the aircraft tyre behaviour associated with aircraft manoeuvres on a runway.

### 1.2.2 Pilot model

A pilot model can be employed to enable closed-loop simulations and explore pilot-aircraft interactions, providing a candidate controller for ground manoeuvres. Nowadays, mathematical representations of human control behaviour have played a critical role in manned aviation, e.g. in the definition of aircraft handling qualities requirements. Pilot modelling has evolved into a wide engineering field with contributions from many disciplines that consider interaction with human beings. Particular aspects, including sensory, bio-dynamic and control, are considered to be fundamental to modelling manual control dynamics exhibited by aircraft pilots. In this section, we will focus on the control aspect and review existed control-theoretic pilot models.

McRuer proposed the underlying principle in manual control theory during 1970s as a fundamental assumption in the formulation of the crossover model of the human operator [33]. The crossover model led to the development of various other quasi-linear models [34, 35, 36]. The appeal of such models is their simplicity and the ease with which they can be applied within a control framework. In the context of modern control, Wierenga [37] and Kleinman [38] et al. developed the optimal control model (OCM) which assumes that a well-trained and motivated human operator behaves in an optimal manner whilst remaining subject to inherent psycho-physical limitations. To conduct comparative studies with classical models and also to simplify the OCM algorithm, the modified OCM (MOCM) [39] and the fixed order OCM [40] are developed.

Both produce transfer function representations that retain the most important features for frequency domain analysis and comparison. Motivated by the desire to improve flight simulator cueing, the descriptive model is proposed by Hosman during 1990s which is aimed at understanding the influence of visual and vestibular simulation on pilot's perception and control behaviour [41].

Whilst pilot modelling for aircraft in flight has been comprehensively studied, ground manoeuvres has received very little attention. For pilot modelling on the ground, the idea of a driver model can be borrowed from the automotive area. Path following is one of the core elements of a driver model. The resulting control input should minimise the difference between the reference path and actual path with respect to lateral deviation and the vehicle heading. The most popular two types of methods for path following are geometric methods and model-based methods. In geometric methods, steering control laws are derived from simple geometric relations which can extend from simple circular arc calculations to much more complex geometric theorems, such as the pure pursuit algorithm [42]. Geometric path following algorithms are simple to implement, robust to path curvatures, and suitable for low speed driving. At higher speed, however, where nonlinearities of vehicle dynamics have to be considered, model-based methods are generally better. Model Predictive Control (MPC) has been successful in semi-autonomous and autonomous driving [43, 44, 45, 46]. MPC can handle Multi-Input Multi-Output systems with input and state constraints while taking into account nonlinear dynamics. Published MPC schemes use dynamic vehicle models combined with linear, Pacejka, and Fiala tyre models. This method is computationally expensive due to the complexity of the overall model.

There are many other existing driver models that are potential candidates for aircraft steering control. The earliest driver model of note is the 'cross-over' model [47]. It represents driving as a small perturbation regulation task which mainly concerns travelling in a straight line under crosswind disturbance. Attempts to extend its domain to cover more general driving appear contrived and only marginally effective [48]. In a recent work of Best [49], a simple

realistic driver model is developed for an automotive application. It is based on a single preview point with the steering control law solely based on correction of a previewed deviation from the target path.

Driver models based on preview of the road ahead achieve effective path following control [50] by minimising error at multiple preview points. MacAdam presents an optimal preview control model which offers a useful and direct method for representing closed-loop behaviour of linear driver/vehicle systems [51]. It suggests that driver automobile steering control can be viewed as a time-lagged optimal preview control process. Substantial progress in driver modelling is made in this work, however, it is still in a linear world. The main weakness of this method is pointed out by Guo and Guan [50] that it assumes constant steering input over the preview interval to estimate the vehicle position. In a later work by MacAdam and Johnson [52], they demonstrate elementary neural network structures for modelling and representing driver steering behaviour in path regulation control tasks. The adaptive nature of neural networks can be used effectively under a wide range of operational conditions. Sharp et al. set up a particular driver model, combining multiple preview points and yaw control [53]. The structure of their model derives from linear optimal discrete time preview control theory, but it deals with the nonlinear vehicle operating regime. Saturation properties are introduced into the controller, to match the saturation properties of the vehicle tyres. Its parameter values are obtained by heuristic methods, using insight gained from linear optimal control theory. Ungoren and Peng [54] provide a similar approach to achieve an adaptive lateral preview driver model. They propose a driver model developed based on the adaptive predictive control (APC) framework. It uses predicted vehicle information to determine the optimal steering action; a tunable parameter is defined to assign relative importance to lateral displacement and yaw error in the cost function to be optimized.

Recently, driver models have increased to support advanced driver assistance systems (ADAS) and autonomous vehicle research with emphasis on better understanding and replication of the driver dynamic system. Keen and

Cole propose a multiple-model structure to a driver's internal model combined with a model predictive steering controller [55]. This structure provides a straightforward way to represent a range of driver expertise. Cole improves an existing driver model with neuromuscular dynamics on the vehicle response to lateral force disturbances [56]. This shows that steering torque feedback has a significant influence on the driver's reflex response to disturbances. Bi et al. also present a driver model based on cognitive architecture to capture the dynamic interaction between the vehicle steering system and the driver's neuromuscular system [57]. More recently, a new model of driver steering control incorporating human sensory dynamics is proposed by Nash and Cole [58], with an extension to represent the control of a nonlinear vehicle.

### 1.2.3 Bifurcation analysis

Continuation is a numerical method used to compute and track steady-state solutions of a dynamical system under the variation of parameters [59]. Based on continuation, bifurcation analysis is able to identify safe parameter regions in which the dynamical system follows a stable solution. Also, it is possible to follow unstable solutions, leading to the identification of physical phenomena which might not be detected with time-history simulations alone.

Bifurcation analysis has been used successfully to investigate the longitudinal behaviours of low-order road vehicle models with periodic forcing [60] and driver feedback control [61, 62]. The lateral dynamics of road vehicle were studied based on bifurcation theory by Nguyen et al. [63]. The first application of bifurcation analysis in aerospace was in the area of flight mechanics [64]. It has also been identified by NASA as a key technology for the analysis of aircraft flight dynamics in off-nominal conditions [65]. Additionally, bifurcation techniques have been comprehensively used to study nose gear wheel shimmy based on low-order mathematical models [66, 67, 68, 69, 70].

The application of bifurcation and continuation methods is still a new subject in the area of the aircraft ground manoeuvres. The usefulness of bifur-

cation analysis in this area was firstly demonstrated by Coetzee [21]. Further studies by Rankin identified safe ground operating regions for the A320 using industrially developed models and a simplified mathematical model [22, 24, 71]. More recently, a study by Coetzee expands on the statically determinate gear arrangement of the A380 by analysing different ground manoeuvres and additional mass cases [72].

### 1.2.4 Optimal control theory

As an extension of the calculus of variations, optimal control is a mathematical optimisation method for deriving control policies. It deals with the problem of finding a control law for a given system that optimises a specific performance index while satisfying any constraints on the motion of the system. Optimal control problems (OCP) are generally solved numerically due to the complexity and variety of applications. The methods for numerically solving optimal control problems can be grouped into two main categories: indirect methods and direct methods. A comprehensive summary of optimal control approaches and numerical solution methods can be found in [73, 74, 75, 76].

Indirect methods rely on Pontryagin's Maximum Principle [77]. The conditions for optimality are defined as a set of ordinary differential equations with both initial and final boundary conditions. The optimal control law is then derived from this two-point boundary value problem coupled with a minimisation problem. Various numerical techniques can be used to solve such a problem. An iterative simulation-based method known as Generalized Optimal Control [78, 79] is used to identify optimal control inputs by minimizing a user-defined cost function. These control inputs can be optimized simultaneously for any smoothly nonlinear system, as demonstrated in a recent study of collision-avoidance strategies for cars by Best [80]. The time-optimal inverse simulation of car handling is investigated by Hendrikx et al. [81] using the gradient method after formulating the problem as one of optimal control. Based on nonlinear car and tyre models, the driver actions which are required

to perform specific manoeuvres in as short a time as possible are identified. Bertolazzi et al. present a method for the symbolic derivation of the equations of the OCP applied to a generic multibody system [82]. By using Lagrange multipliers and penalty functions, the constrained problem is transformed into a nonconstrained problem. Through the use of this technique, Tavernini et al. investigate minimum time cornering strategies on different road surfaces with different transmission layouts in [83] and handbrake cornering strategy in [84]; Bianco et al present minimum lap time simulation of a GP2 car with a multibody car model and enhanced load transfer dynamics [85]. As one of the most effective optimal control software based on an indirect method, Pins is used here to solve the optimal control problems.

In direct methods, OCP is transferred into a nonlinear programming problem (NLP) also known as direct transcription. Controls and states are discretised in different numerical schemes. It is a sequential collocation if only controls are discretised and a full collocation if controls and states are all discretised. One of the most efficient sequential collocation methods is direct multiple shooting (also known as parallel shooting) which is successfully applied to a minimum time problem in [86] with gear choice using MUSCO-II software. Indeed, methods based on full collocation are more widely spread. The software IPOPT [87] based on a primal-dual interior-point algorithm can be used to solve the resulting NLP. This is the solver for all the approaches whatever discretisation method is used. In [88], simultaneous collocation is used to discretise continuous-time variables on an equidistant grid of the time horizon with $Ne$ elements; in each element, the optimisation variables are approximated by Lagrange Polynomials at $Np$ collocation points (Radau points). In [89], a MATLAB-based optimal control transcription toolbox ICLOCS [90] is used with trapezoidal integration to approximate integral cost and the constraints associated with the system dynamics. A direct orthogonal collocation method based on the Radau pseudo-spectral scheme by means of the software package GPOPS-II [91] is used to investigate the optimal usage of energy recovery systems on fuel consumption saving in [92] and the optimal aerosuspension

interactions and adjustments on the lap-time performance of a car in [93].

### 1.2.5 Summary

Rankin's model provides a white-box structure with reasonable complexity and accuracy[22]. Therefore, in this research, a high-fidelity aircraft model is developed based on Rankin's model, with the addition of a combined-slip tyre model. To conduct closed-loop simulations, a pilot model is proposed, borrowing the idea of a simple realistic driver model developed by Best [49], which is effective, efficient, and easy to implement. Improved with an additional yaw rate control, this pilot model can be used to perform mechanistic path following tasks and represent a pilot's manual operation. To pursue a real-time optimal controller for aircraft steering control, the Linear Quadratic method with lookahead is considered, which is originally proposed by Sharp [13] in an automotive application. In terms of numerical optimal control, the indirect method Generalised Optimal Control (GOC) [80] has better modifiability compared to most existing toolboxs that are based on direct method, providing easy access to intermediate results, e.g. slip angles. In view of this, GOC is used to numerically investigate the optimal solution, providing a benchmark against which the optimality of a controller can be evaluated.

## 1.3 Thesis overview

In Chapter 2, a fully parameterised nonlinear aircraft model is presented in the form of a system of coupled ordinary differential equations. A rigid tricycle body is considered as the airframe layout with parameters chosen to represent a mid-sized single-aisle passenger aircraft, e.g. A320. Nonlinear effects are included in the tyre model and aerodynamic model. The aircraft model offers an appropriate level of accuracy and complexity with full accessibility to system states and intermediate variables. A bifurcation analysis is performed to gain a global picture of steady-state solutions of the dynamical system within a typical

operational envelope. Steering angle is chosen as a continuation parameter to illustrate how turning circle solutions vary with thrust, CG position and coefficient of friction. On the other hand, dynamic simulations are conducted to capture transient behaviours. Two scenarios are considered where transient behaviours cause the aircraft to lose directional control can be observed.

In Chapter 3, an Expert Pilot Model (EPM) is developed based on a simple realistic driver model originally designed for an automotive application. It enables closed-loop simulations of the pilot/aircraft dynamical system, which in turn helps to provide a deeper understanding of manually operated ground manoeuvres. The steering control is based on correction of the lateral deviation at a single preview point which is located by projecting along a steady turning circle. To overcome large delays due to the aircraft's massive yaw moment of inertia, the pilot model is improved by an additional control with respect to yaw rate. Taking advantage of this yaw rate control, the oscillatory system responses are significantly reduced. To follow a given path on the ground, either the nose-gear or CG can be used as a reference point. We provide some guidance for the setting of controller parameters. The proposed pilot model can be tuned via a couple of parameters, and the optimisation of these parameters is given in detail.

In Chapter 4, Generalised Optimal Control is employed to numerically investigate the optimal solutions for aircraft runway exit manoeuvres. GOC is an indirect method of optimal control based on a gradient descent implementation of Pontryagin's Maximum Principle. For a specific manoeuvre-cost function combination, GOC minimizes a Hamiltonian function with respect to system states and co-states. Three scenarios are investigated: path following with minimum lateral deviation, fast runway exit with minimum runway occupancy time, and minimum tyre wear. GOC provides proper convergence of off-line optimisations despite not being the most state-of-the-art method. Indeed, its optimal solution is a benchmark against which the effectiveness of future controllers can be judged.

In Chapter 5, Predictive Steering Control (PSC) is developed to fill the

gap between EPM and GOC, offering a realisable near-optimal real-time controller. The aircraft model is linearised at every discrete instant, then the optimal control gain sequence is obtained by interpolating between a set of precomputed control gains using lateral acceleration as the measurement. To evaluate how much benefit the aircraft could get from using this real-time optimal controller, it is compared with EPM in different runway geometries and at different speeds. PSC delivers near-optimal solutions which are more effective and intelligent than the pilot could achieve. Finally, a comprehensive robustness study is carried out. A compact version of PSC based on a constant control gain sequence is tested and compared with the original version. From the robustness study we can see that the proposed controller is robust to uncertainties in mass, CG position, and road condition and disturbances of crosswind.

This study makes contributions to the literature on control of aircraft ground manoeuvres in following ways. Firstly, the Expert Pilot Model is specifically designed for aircraft steering control on the ground, which limited research has been conducted on. The simple Proportional-Integral control algorithm based on steady-state prediction achieves better path following performance compared with average pilots. Secondly, the optimal control strategy for runway exit manoeuvres is revealed for the first time by using Generalised Optimal Control. It provides a benchmark for controller design in the future. Thirdly, the proposed Predictive Steering Control (PSC) provides advantages over the original LQ controller via an extended prediction horizon of 20s based on steady-state handling equation. It is suitable for real-time implementation and able to achieve near-optimal solutions.

# Chapter 2

# Aircraft Mathematical Model

## 2.1 Introduction

In order to design a controller, it is important to create a mathematical model for the target dynamical system with an appropriate level of fidelity and complexity. In this chapter a fully parameterised nonlinear model is developed to capture the aircraft ground dynamics. This model is based on Rankin's model [22] which was initially developed from an industrially validated SimMechanics model [23]. It takes the form of a system of coupled ordinary differential equations (ODEs). The model parameters are chosen to represent a typical mid-sized, single-aisle, passenger aircraft, e.g. A320. The airframe is considered as a rigid body tricycle with 6 degrees-of-freedom. Three landing gears are attached to the airframe: two main-gears are connected with translational joints (moving in the vertical axis only); the nose gear is connected using a cylindrical joint (moving in and rotating around the vertical axis). Nonlinearities enter the system via sub-models of tyres and aerodynamics which are modelled in accordance with industry experience and test data. The overall mathematical model provides a suitable trade-off between accuracy and complexity. Moreover, the white-box nature of this model ensures that all the parameters, both design parameters (such as dimensions of the aircraft)

and operational parameters (such as total mass and CG position), are fully accessible.

For ground manoeuvres, one of the most important nonlinear effects is the tyre/ground friction forces. Aircraft typically use tubeless radial tyres in view of better failure characteristics compared with bias-ply tyres [25]. The force elements acting on the tyres are calculated with a combined-slip tyre model developed from a tyre model proposed by GARTEUR action group, which only considers lateral slip. To incorporate the control inputs of brake torques, longitudinal slip is modelled by adding additional freedoms of wheel speeds for both main landing-gears. The fundamental work behind this model can be found in [31]. Since there is no brake mechanism on the nose-gear, the tyre can be modelled without longitudinal slip. Considering each gear has two tyres and the separation distance is small, they are assumed to act as one. In addition to tyre forces, aerodynamics are also nonlinear because they are proportional to the square of aircraft speed and the aerodynamic coefficients are nonlinear functions of sideslip angle and attack angle. In the case of ground manoeuvres, the attack angle remains relatively steady. The aerodynamic model consists of six force components (three translational and three moments) which are all assumed to act at the aerodynamic centre of the aircraft, defined as 25% along the mean aerodynamic chord from its leading edge.

A numerical continuation method can be used to compute and track steady-state solutions of a dynamical system of nonlinear ordinary differential equations under the variation of parameters. In combination with the technique of bifurcation analysis, one can perform a stability analysis by following solutions and detecting the change of stability (bifurcation). Bifurcations can then be followed in more parameters to identify regions in parameter space that correspond to different behaviour of the system. In this chapter, the steering angle is used as a continuation parameter to compute how the turning circle solutions change as the steering angle is varied. The engine thrust is used as a second parameter despite it being kept constant for individual continuation runs. Then continuation runs are performed across a range of discrete

thrust levels. In addition to steer and thrust, bifurcation analysis is further conducted based on operational parameters, for example total mass, CG position and coefficient of friction. The continuation method used to produce this bifurcation analysis is able to identify safe regions of parameters where the aircraft follows a stable turning circle. Furthermore, it is possible to follow unstable solutions, revealing physical phenomena which otherwise might not be identified by running simulations alone. A state variable can be plotted against parameters in bifurcation diagrams, which illustrate how stability changes at bifurcation points. This provides a global picture of the dynamics of the dynamical system, to inform about the range of valid operation of the aircraft.

The chapter is organised as follows: In section 2.2 full details of the aircraft model including the tyre model and aerodynamic model are given. An extensive bifurcation analysis of turning solutions of the aircraft with variation of multiple operational parameters is demonstrated in Section 2.3. Finally, conclusions and directions of future work are given in Section 2.4.

## 2.2 Mathematical Model

The proposed aircraft model is able to provide physically-relevant behaviour of aircraft ground dynamics. In this model, the airframe is assumed to act as a rigid body with six degrees-of-freedom (DOF), with a coordinate system consistent with the aircraft's principle axes of inertia. The SAE axis system is adapted: the origin is the centre of gravity; the x-axis is positive towards the nose of the aircraft; the z-axis is positive towards the ground; the y-axis is positive starboard (as defined by the right hand rule). The airframe interfaces with the ground via three landing gears. Two main landing gears are connected to the airframe with translational joints (allowing a relative translation along the vertical axis only), whilst the nose gear is connected with a cylindrical joint (allowing a relative translation along and a rotation about the vertical axis). The aircraft velocities are described in the body coordinate system while the

position and attitude are described in a fixed ground coordinate system.

Since this chapter aims to optimize the application of steering, braking and thrust simultaneously, Rankin's model has been developed with addition of a combined-slip tyre model. The brakes, which are only applied to the main gears, create a difference between the wheel's contact-patch speed and translational speed. This requires another two state variables in the model, to represent the main gears' contact-patch velocities. The control variables considered here include steering angle $\delta$, thrust force of the right/left engine $F_{xTR}/F_{xTL}$, and brake torque $T_{brake}$. The rest of this section provides details of the mathematical model, highlighting developments that have been made in this research.

The aircraft's equations of motion are formulated as a coupled system of ordinary differential equations (ODEs), formed by balancing forces and moments in each degree of freedom. The relative positions and directions of the force elements that act on the aircraft are shown in the three standard projections in Fig.2.1. Additional state coupling occurs via related sub-models such as tyre model aerodynamic model. The aircraft translational and rotational velocities are defined in the local axis system

$$
\begin{aligned}
\dot{V}_x &= (F_{xTL} + F_{xTR} - F_{xR} - F_{xL} - F_{xN}\cos(\delta) - F_{yN}\sin(\delta) - F_{xA} + F_{zW}\sin(\theta))/m \\
&\quad - V_y W_z + V_z W_y \\
\dot{V}_y &= (F_{yR} + F_{yL} + F_{yN}\cos(\delta) - F_{xN}\sin(\delta) + F_{yA} + F_{zW}\sin(\varphi))/m - V_x W_z + V_z W_x \\
\dot{V}_z &= (F_{zW}\cos(\theta)\cos(\varphi) - F_{zR} - F_{zL} - F_{zN} - F_{zA})/m - V_y W_x + V_x W_y \\
\dot{W}_x &= (l_{yL}F_{zL} - l_{yR}F_{zR} - l_{zL}F_{yL} - l_{zR}F_{yR} - l_{zN}F_{yN}\cos(\delta) + l_{zN}F_{xN}\sin(\delta) + l_{zA}F_{yA} \\
&\quad + M_{xA})/I_{xx} + (I_{yy} - I_{zz})W_y W_z \\
\dot{W}_y &= (l_{xN}F_{zN} - l_{zN}F_{xN}\cos(\delta) - l_{zN}F_{yN}\sin(\delta) - l_{xR}F_{zR} - l_{zR}F_{xR} - l_{xL}F_{zL} - l_{zL}F_{xL} \\
&\quad + l_{zT}F_{xTR} + l_{zT}F_{xTL} + l_{zA}F_{xA} + l_{xA}F_{zA} + M_{yA})/I_{yy} + (I_{zz} - I_{xx})W_x W_z \\
\dot{W}_z &= (l_{yR}F_{xR} - l_{yL}F_{xL} - l_{xR}F_{yR} - l_{xL}F_{yL} + l_{xN}F_{yN}\cos(\delta) - l_{xN}F_{xN}\sin(\delta) + l_{xA}F_{yA} \\
&\quad + l_{yT}F_{xTL} - l_{yT}F_{xTR} + M_{zA})/I_{zz} + (I_{xx} - I_{yy})W_x W_y
\end{aligned}
\tag{2.1}
$$

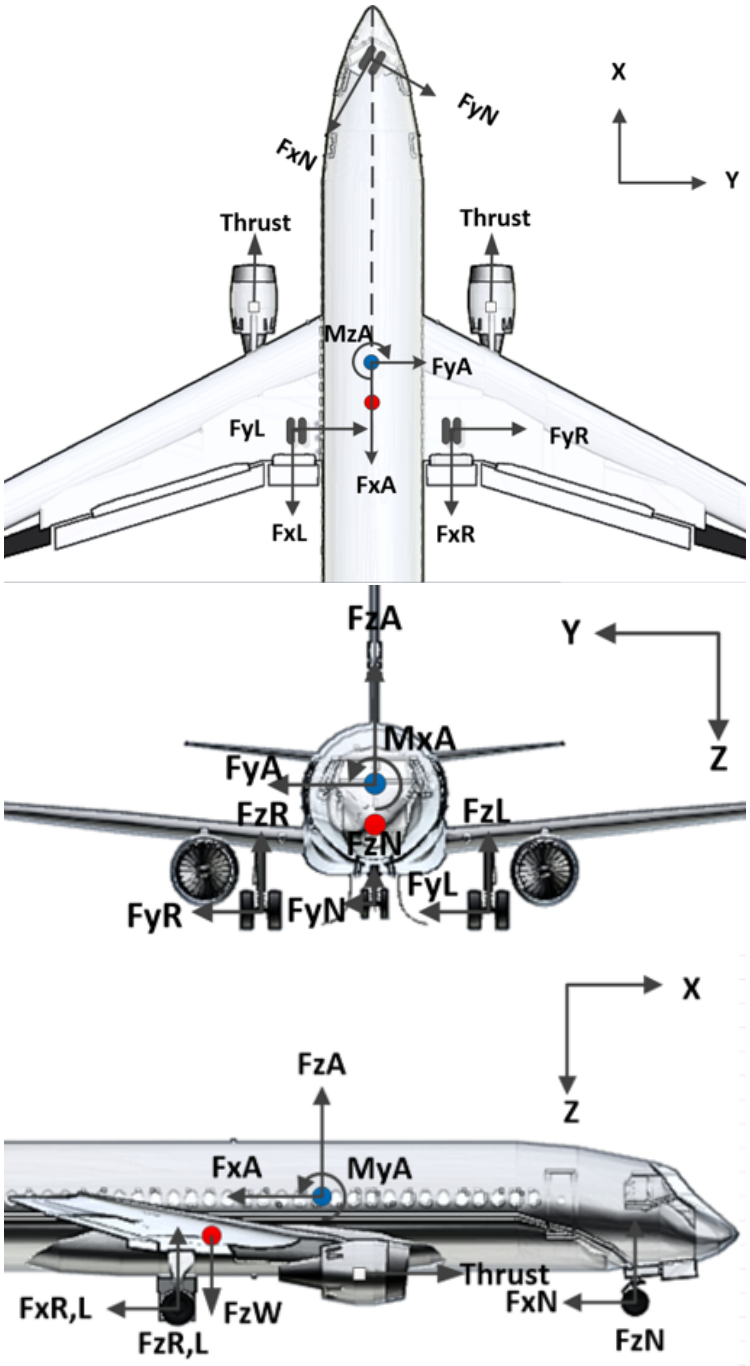


Figure 2.1: Positions and directions of the force elements that act on the aircraft.

Table 2.1: Aircraft parameters and values

| **Symbol** | **Parameter** | **Value** |
|---|---|---|
| $m$ | aircraft total mass | $54500kg$ |
| $CG$ | aircraft centre of gravity | 30% |
| $l_{xN}$ | x-distance to the nose gear | 11.444 $m$ |
| $l_{zN}$ | z-distance to the nose gear | 2.932 $m$ |
| $l_{xR,L}$ | x-distance to the right/left gear | 1.240 $m$ |
| $l_{yR,L}$ | y-distance to the right/left gear | 3.795 $m$ |
| $l_{zR,L}$ | z-distance to the right/left gear | 2.932 $m$ |
| $l_{xA}$ | x-distance to the aerodynamic centre | 1.008 $m$ |
| $l_{zA}$ | z-distance to the aerodynamic centre | 0.988 $m$ |
| $l_{xT}$ | x-distance to the thrust centre | 1.008 $m$ |
| $l_{yTR,L}$ | y-distance to the thrust centre | 5.755 $m$ |
| $l_{zT}$ | z-distance to the thrust centre | 1.229 $m$ |
| $l_{mac}$ | Mean aerodynamic chord | 4.194 $m$ |
| $S_w$ | aircraft wing area | 122.4 $m/s^2$ |
| $\rho$ | air density | 1.225 $kg/m^3$ |
| | | |
| $k_{zN}$ | Stiffness coefficient of the nose-gear | 1190 $kN/m$ |
| $k_{zM}$ | Stiffness coefficient of the main-gear | 2777 $kN/m$ |
| $c_{zN}$ | Damping coefficient of the nose-gear | 1000 $Ns/m$ |
| $c_{zM}$ | Damping coefficient of the main-gear | 2886 $Ns/m$ |
| $c_{rr}$ | Rolling resistance coefficient | 0.02 |
| $R_{wheel}$ | Wheel radius of main-gears | 0.64 $m$ |
| | | |
| $I_{xx}$ | Moment of inertia about x-axis | 1095840 $kg \cdot m^2$ |
| $I_{yy}$ | Moment of inertia about y-axis | 3057600 $kg \cdot m^2$ |
| $I_{zz}$ | Moment of inertia about z-axis | 4002000 $kg \cdot m^2$ |

Two additional ODEs describe the two main-gears' wheel rotations using a moment balance between the brake torque $T_{brake}$ and friction force $F_{xR,L}$ about the wheel's roll axis:

$$I_{MG}\dot{\Omega}_R = -F_{xR}R_{wheel} - T_{brake} \tag{2.2}$$

$$I_{MG}\dot{\Omega}_L = -F_{xL}R_{wheel} - T_{brake} \tag{2.3}$$

The model parameters chosen for this work are given in Table 1. The term CG is the location of the centre of gravity from the leading edge of the wing root, expressed as a percentage of Mean Aerodynamic Chord (MAC). In this paper, the center of gravity is fixed at its forward position of 30% MAC, which corresponds to a lightweight mass case (54500kg). The aircraft's weight ($F_{zW} = mg$) acts at the centre of gravity along the z-axis in the ground coordinate system, so it captures the effects of pitch and roll angles in the body co-ordinate system. The nose gear steering angle is denoted by $\delta$; no other wheels are used to steer the aircraft. Orthogonal tyre forces ($F_{xN,R,L}, F_{yN,R,L}, F_{zN,R,L}$) are defined at the tyre-ground contact patch. The aerodynamic forces ($F_{xA}, F_{yA}, F_{zA}$) and moments ($M_{xA}, M_{yA}, M_{zA}$) act on the aerodynamic centre of the aircraft. The thrust forces ($F_{xTR}, F_{yTR}$) act parallel to the x-axis of the aircraft.

A ground coordinate system is considered in order to describe the aircraft's motion on the ground. The global position of the aircraft CG is defined in a global Cartesian frame $(X, Y, Z)$ while the attitude of the airframe is defined by Euler angles $(\psi, \theta, \varphi)$ , where $\psi$ is the yaw angle, $\theta$ the pitch angle and $\varphi$ the roll angle. The aircraft's translational velocities and angular velocities in the ground coordinate system are defined as $(V_{xG}, V_{yG}, V_{zG})$ and $(W_{xG}, W_{yG}, W_{zG})$ respectively. Transformations from the local body coordinate system to the ground coordinate system are based on the standard sequence of rotations given in Philips [13]. Assuming that the pitch angle and roll angle are relatively small, small angle approximation ($\sin\theta \approx \theta; \cos\theta \approx 1$) is used when calculating

the velocities in the ground coordinate system:

$$V_{xG} = V_x \cos(\psi) - V_y \sin(\psi) + \theta V_z \cos(\psi) + \varphi V_z \sin(\psi) \tag{2.4}$$

$$V_{yG} = V_x \sin(\psi) + V_y \cos(\psi) + \theta V_z \sin(\psi) - \varphi V_z \cos(\psi) \tag{2.5}$$

$$V_{zG} = -\theta V_x + \varphi V_y + V_z \tag{2.6}$$

$$W_{xG} = W_x + \theta W_z \tag{2.7}$$

$$W_{yG} = W_y - \varphi W_z \tag{2.8}$$

$$W_{zG} = W_y \varphi / \cos(\theta) + W_z \tag{2.9}$$

Another six ODEs are therefore introduced to calculate aircraft's position and attitude in the global reference frame:

$$\dot{X} = V_{xG} \tag{2.10}$$

$$\dot{Y} = V_{yG} \tag{2.11}$$

$$\dot{Z} = V_{zG} \tag{2.12}$$

$$\dot{\psi} = W_{zG} \tag{2.13}$$

$$\dot{\theta} = W_{yG} \tag{2.14}$$

$$\dot{\varphi} = W_{xG} \tag{2.15}$$

The position $(X, Y)$ and yaw angle $\psi$ can be used to plot the trajectory of the aircraft CG.

### 2.2.1 Tyre model

At the lower velocities experienced by an aircraft on the ground, the forces generated by tyres have a dominant effect over the aerodynamic forces on the aircraft's motion. Hence, a realistic tyre model is essential to capture the system response accurately. The lateral forces on the tyres are calculated with a tyre model developed by GARTEUR Action Group. The original model's capability is extended here to include longitudinal tyre dynamics. Throughout this section a second subscript N, R or L following x, y or z indicates the nose,

right or left landing gear's local coordinate system with which the velocity or force elements are aligned.

The vertical force on each landing gear is modelled as a spring and damper system:

$$F_{zN} = -k_{zN}(\delta_{zN}) + c_{zN}V_{zN} \tag{2.16}$$

$$F_{zR} = -k_{zR}(\delta_{zR}) + c_{zR}V_{zR} \tag{2.17}$$

$$F_{zL} = -k_{zL}(\delta_{zL}) + c_{zL}V_{zL} \tag{2.18}$$

The stiffness coefficients $k_{zN,R,L}$ and damping coefficients $c_{zN,R,L}$ are listed in Table 1. The vertical velocity of each tyre $(V_{zN}, V_{zR}, V_{zL})$ is calculated in terms of the aircraft's velocities in the local body coordinate system as follows:

$$V_{zN} = V_z - l_{xN}W_y \tag{2.19}$$

$$V_{zR} = V_z + l_{yR}W_x + l_{xR}W_y \tag{2.20}$$

$$V_{zL} = V_z - l_{yL}W_x + l_{xL}W_y \tag{2.21}$$

Making the assumption that the roll axis of each tyre remains parallel to the ground at all time, vertical tyre deflection $(\delta_{zN,R,L})$ can be expressed in terms of the aircraft's CG height, pitch angle and yaw angle:

$$\delta_{zN} = -l_{zN} - Z + l_{xN}\sin(\theta) \tag{2.22}$$

$$\delta_{zR} = -l_{zR} - Z - l_{xR}\sin(\theta) - l_{yR}\sin(\varphi) \tag{2.23}$$

$$\delta_{zL} = -l_{zL} - Z - l_{xL}\sin(\theta) + l_{yL}\sin(\varphi) \tag{2.24}$$

With the vertical load on each tyre defined, it is possible to calculate the lateral and longitudinal forces generated by each tyre. The longitudinal force generated by each tyre consists of two components: rolling resistance and force caused by slip ratio (in the case of braking). Rolling resistance occurs due to hysteresis in the material of the tyre, and is the primary motion resistance force at low speed. The hysteresis in the tyre causes the pressure in the leading half of the contact patch to be higher than that in the trailing half, resulting in the

generation of a horizontal force (rolling resistance) to balance the moments about the roll axis of the tyre. In the aircraft model, rolling resistance is approximated by:

$$F_{rrN,R,L} = c_{rr} F_{zN,R,L} \cos(\alpha_{N,R,L}) \tag{2.25}$$

Here, $c_{rr}$ is the rolling resistance coefficient (specified in Table 1). A cosine function of slip angle ($\alpha_{N,R,L}$) is incorporated to capture two key features. Firstly, the rolling resistance force decreases with an increasing slip angle and drops off to zero when the tyre is moving sideways ($\alpha_{N,R,L} = \pm 90°$); secondly, there is a sign change when the direction of motion changes ($|\alpha_{N,R,L}| > 90°$).

When the wheel is subject to a lateral force, the tyre slips sideways due to deformation in the carcass and tread. As a result, this deflection gives rise to the slip angle which is the angle between the direction in which the wheel is pointing and the direction in which it is actually travelling, as shown in Fig.2.2. The slip angle is defined as the angle between the tyre's forward velocity and resultant velocity:

$$\alpha_{N,R,L} = arctan(\frac{V_{yN,R,L}}{V_{xN,R,L}}) \tag{2.26}$$

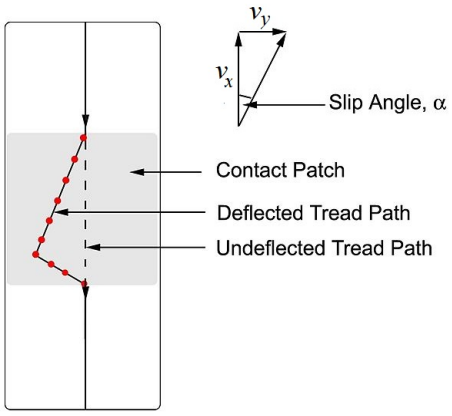


Figure 2.2: Tyre deformation and slip angle.

The slip angle results in a cornering force in the plane of the contact patch. This corning force increases linearly for small slip angles (typically less than 5°), then increases nonlinearly to a maximum before beginning to decrease. Fig.2.3 illustrates the relationship between lateral force and slip angle. It shows how the lateral force (dashed curve) approximates test data for $\alpha \in (0°, 40°)$(solid curve) and how it is extended for $\alpha \in (0°, 180°)$. The lateral force on the nose-gear $F_{yN}$ is defined as a nonlinear function of the slip angle $\alpha_N$ depending on the maximum lateral force $F_{ymaxN}$ attainable at the optimal slip angle $\alpha_{optN}$ [22]:

$$F_{yN} = F_{ymaxN} \frac{2\alpha_{optN}\alpha_N}{\alpha_{optN}^2 + \alpha_N^2} \tag{2.27}$$

$$F_{ymaxN} = -3.53 \times 10^{-6} F_{zN}^2 + 8.83 \times 10^{-1} F_{zN} \tag{2.28}$$

$$\alpha_{optN} = 6.14 \times 10^{-11} F_{zN}^2 + 4.89 \times 10^{-7} F_{zN} + 0.24 \tag{2.29}$$

As this research considers braking on the main-gears, a combined-slip tyre model developed by Milliken [94] is used to determine both longitudinal and lateral tyre forces according to the ratio between longitudinal and lateral slip. When braking is applied on the main-gear, the observed angular velocity of the tyre does not match the expected velocity for pure rolling motion, which means there is sliding between outer surface of the rim and the road. The difference between theoretically calculated forward speed based on angular velocity of the tyre and rolling radius, and actual speed of the wheel, expressed as a percentage, is called slip ratio:

$$S_{R,L} = (\frac{\Omega_{R,L} R_{wheel}}{V_{xR,L}} - 1) \times 100\% \tag{2.30}$$

To combine the slip-angle and slip-ratio, they need to be normalised first:

$$\bar{\alpha}_{R,L} = \frac{C_{yR,L}\alpha_{R,L}}{\mu_{yR,L} F_{zR,L}} \tag{2.31}$$

$$\bar{S}_{R,L} = \frac{C_{xR,L} S_{R,L}}{\mu_{xR,L} F_{zR,L}} \tag{2.32}$$

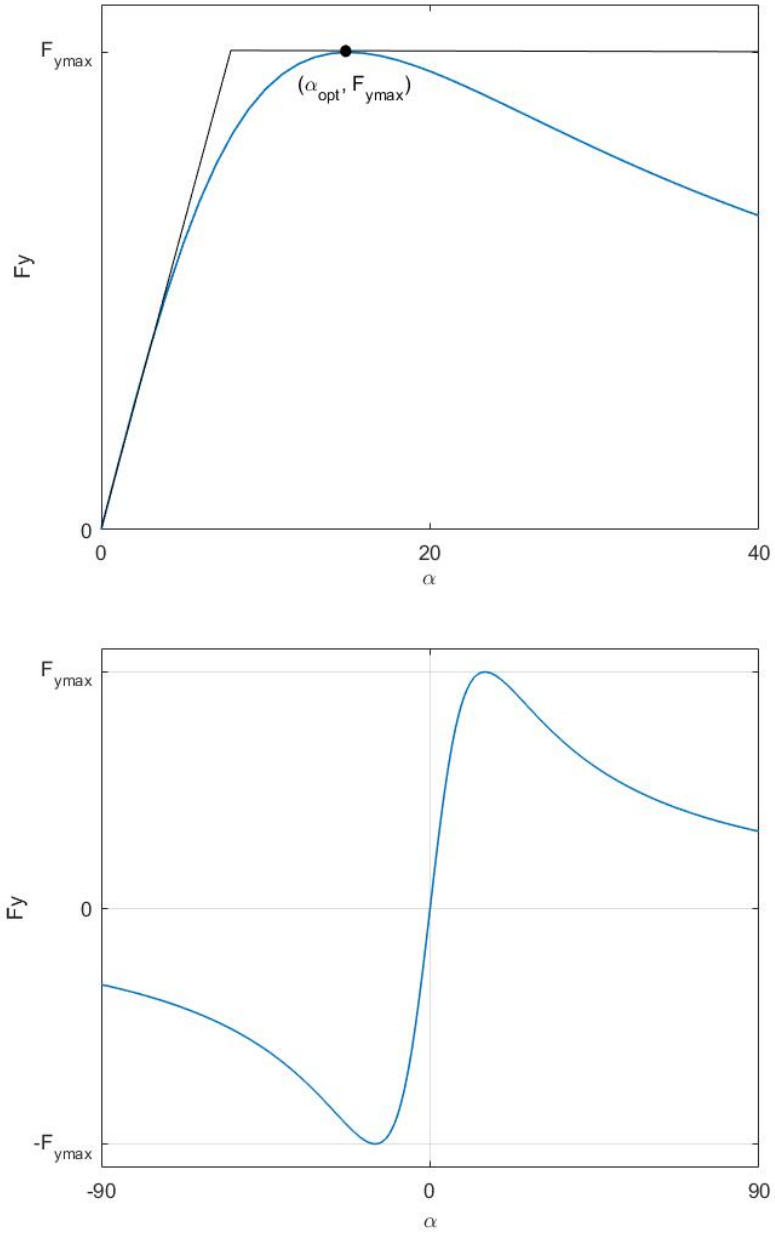


Figure 2.3: Relationship between lateral force and slip angle

The combined slip $k_{R,L}$ can then be defined as:

$$k_{R,L} = \sqrt{\bar{S}_{R,L}^2 + \bar{\alpha}_{R,L}^2} \tag{2.33}$$

According to the model of nose-gear lateral force given by Eqn.2.27, the resultant (normalized) friction force $F_{rR,L}$ can be calculated in a similar way, as a function of the combined slip $k_{R,L}$:

$$F_{rR,L} = \frac{2k_{optR,L}k_{R,L}}{k_{optR,L}^2 + k_{R,L}^2} \tag{2.34}$$

The parameter $k_{optR,L}$ is defined as a quadratic function of the vertical load on the tyre [22]:

$$k_{optR,L} = 1.34 \times 10^{-10} F_{zR,L}^2 + 1.06 \times 10^{-5} F_{zR,L} + 6.72 \tag{2.35}$$

By decomposing the normalized resultant force $F_{rR,L}$, we can find the lateral and longitudinal components $\bar{F}_{yR,L}$ and $\bar{F}_{xR,L}$) from their relationship given by:

$$F_{rR,L} = \sqrt{\bar{F}_{yR,L}^2 + \bar{F}_{xR,L}^2} \tag{2.36}$$

$$\bar{F}_{yR,L} = \frac{\eta_{R,L}\bar{\alpha}_{R,L}}{\bar{S}_{R,L}} \bar{F}_{xR,L} \tag{2.37}$$

Here $\eta_{R,L}$ is a function of the combined slip $k_{R,L}$ that is used to define the above equation for both small and large slip angles and slip ratios, and takes the form:

$$\eta_{R,L} = \begin{cases} \frac{1}{2}(1 + \eta_{0R,L}) - \frac{1}{2}(1 - \eta_{0R,L})\cos(k_{R,L}), & |k_{R,L}| \leq 2\pi \\ 1 \quad , & |k_{R,L}| > 2\pi \end{cases} \tag{2.38}$$

Here, $\eta_{0R,L}$ is computed based on the longitudinal stiffness $C_{xR,L}$, cornering stiffness $C_{yR,L}$, longitudinal coefficient of friction $\mu_{xR,L}$, and lateral coefficient of friction $\mu_{yR,L}$:

$$\eta_{0R,L} = \frac{C_{yR,L}\mu_{xR,L}}{C_{xR,L}\mu_{yR,L}} \tag{2.39}$$

From Eqn.2.36, by substituting $\bar{F}_{yR,L}$ with $\bar{F}_{xR,L}$ using Eqn.2.37, the normalized longitudinal and lateral forces can be derived as:

$$\bar{F}_{yR,L} = \eta_{R,L} F_{rR,L} \frac{\bar{\alpha}_{R,L}}{\bar{S}^2_{R,L} + \eta^2_{R,L} \bar{\alpha}^2_{R,L}} \tag{2.40}$$

$$\bar{F}_{xR,L} = F_{rR,L} \frac{\bar{S}_{R,L}}{\bar{S}^2_{R,L} + \eta^2_{R,L} \bar{\alpha}^2_{R,L}} \tag{2.41}$$

Finally, since the longitudinal and lateral tyre friction forces are normalized with respect to the maximum friction force, the actual forces are given by:

$$F_{yR,L} = F_{ymaxR,L} \bar{F}_{yR,L} \tag{2.42}$$

$$F_{xR,L} = F_{xmaxR,L} \bar{F}_{xR,L} \tag{2.43}$$

The parameters $F_{xmaxR,L}$ and $F_{ymaxR,L}$ are the maximum force that can be generated by the tyre longitudinally and laterally. It is assumed that longitudinal and lateral maximum forces are equal and can be obtained from the equations [22]:

$$F_{ymaxR,L} = -7.39 \times 10^{-7} F^2_{zR,L} + 5.11 \times F_{zR,L} \tag{2.44}$$

$$F_{xmaxR,L} = F_{ymaxR,L} \tag{2.45}$$

### 2.2.2 Aerodynamic model

As aerodynamic forces are proportional to the square of the incoming air velocity, they provide nonlinearity within the aircraft model in addition to the tyre forces. The aircraft aerodynamic coefficients also depend nonlinearly on the angle that the aircraft makes with the airflow, i.e. aerodynamic slip angle $\beta$. By invoking the assumption that the aircraft operates in still air (i.e. neglecting wind effects), and that the angle of attack remains constant during ground manoeuvres, the aerodynamic slip angle can be defined in the same way as the tyre model:

$$\beta = \arctan(\frac{V_y}{V_x}) \tag{2.46}$$

Here, $V_x$ and $V_y$ are the velocities of the aircraft CG in the local body coordinate system. The aerodynamics model consists of six elements: three forces and three moments about each axis of the aircraft. It is assumed that all the force elements act at the aerodynamic center of the aircraft, which is defined at 25% along the mean aerodynamic chord from its leading edge. The six force elements are modelled as follows:

$$F_{xA} = \frac{1}{2}\rho |V|^2 S_w C_x(\beta) \tag{2.47}$$

$$F_{yA} = \frac{1}{2}\rho |V|^2 S_w C_y(\beta) \tag{2.48}$$

$$F_{zA} = \frac{1}{2}\rho |V|^2 S_w C_z(\beta) \tag{2.49}$$

$$M_{xA} = \frac{1}{2}\rho |V|^2 S_w l_{mac} C_l(\beta) \tag{2.50}$$

$$M_{yA} = \frac{1}{2}\rho |V|^2 S_w l_{mac} C_m(\beta) \tag{2.51}$$

$$M_{zA} = \frac{1}{2}\rho |V|^2 S_w l_{mac} C_n(\beta) \tag{2.52}$$

Here, $|V|$ is the aircraft's resultant velocity, and the parameters $\rho$, $S_w$,$l_{mac}$ are listed in Table 1. The aerodynamic coefficients $C_x$,$C_y$,$C_z$,$C_l$,$C_m$,$C_n$ are nonlinear functions of aerodynamic slip $\beta$. The relationship between aerodynamic coefficients and aerodynamic slip are obtained from the SimMechanics model developed by the GARTEUR Group [5]. Since aircraft speed and aerodynamic slip are both small when taxiing, we use linear aerodynamic coefficients which are approximated as following:

$$C_x = 0.06 \tag{2.53}$$

$$C_y = -0.03 * \beta \tag{2.54}$$

$$C_z = 0.4 \tag{2.55}$$

$$C_l = -0.02 * \beta \tag{2.56}$$

$$C_m = -0.1 \tag{2.57}$$

$$C_n = 0.025 * \beta \tag{2.58}$$

## 2.3 Bifurcation method

In dynamical systems, a bifurcation occurs when a small smooth change made to the bifurcation parameters of a system causes a qualitative or topological change in its behaviour. Generally, at a bifurcation point, the local stability of equilibria, periodic orbits or other invariant sets changes. In this section, we use a continuation toolbox named Dynamical System Toolbox, to perform bifurcation analysis of the aircraft model. The stability of turning circle solutions is studied over a range of discrete fixed thrust levels; for each thrust case, the steering angle is varied as a single continuation parameter. Additionally, the steady turning solutions are studied with varied operational parameters: CG position and road condition.

Each continuation run is performed at a fixed thrust level which maintains a constant straight-line velocity. Initial points to start individual continuation runs are steady-state solutions which are considered as the aircraft travelling in a straight-line at constant velocities. Starting from such an initial condition, the steering angle is varied between 0° and 90° while the stability is monitored. The required thrust force is obtained by a PI controller with the steering angle set to 0°. The results from the continuation runs are presented in bifurcation diagrams where the forward velocity and/or lateral acceleration of the aircraft are plotted against steering angle.

By doing bifurcation analysis, we can better understand aircraft ground dynamics. We are able to identify the stability boundary of aircraft ground manoeuvring over different external control inputs and operational parameters. It reveals how aircraft turning solutions change with thrust, CG position, and coefficient of friction. Any unstable branches found would form a safety envelop for operational parameters and control inputs which provides a basic guidance for the design of a real-time controller. By doing this we can avoid the aircraft going into an unstable region. In the case that only stable steady state solutions are found, the results can be used in two ways: first, the aircraft model can be validated if the stable solutions are varying with operational parameters

or control inputs in a sensible way; second, different stable branches indicate the aircraft's sensitivity to specific parameters, such that the controller can be tuned or optimised accordingly to improve robustness.

### 2.3.1 Varied thrust level

The aircraft stability might change at different speed. Basically, the higher the forward speed is, the more likely the turning solution becomes unstable. To study the stability of aircraft ground manoeuvring, we consider four typical taxiing speeds based on the nominal configuration (m=54500kg; CG=30%MAC): $5m/s$, $10m/s$, $15m/s$, and $20m/s$. The corresponding thrust levels are identified by running simulations for enough time until the derivatives of all states converge to zero. For each continuation run, the thrust force is kept constant.

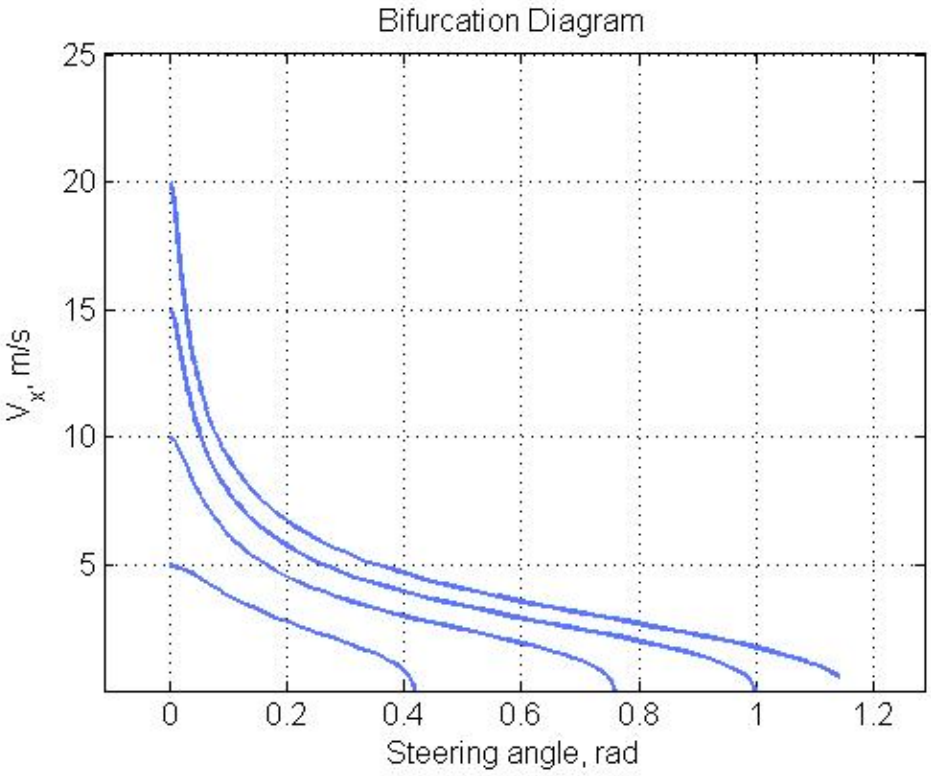


Figure 2.4: Bifurcation diagram for different thrust levels.

The bifurcation diagram in Fig.2.4 shows how forward speed varies with steering angle. Due to the low thrust force in this case, there is no bifurcation point observed at all speeds. When a steering angle is applied, the tyre generates a lateral force that holds the aircraft in a turning circle. As the steering angle is increased, the aircraft's forward velocity decreases along with a reduction of turning radius. At any thrust level, there exists a maximum steering angle at which the forward velocity drops off to zero, due to the thrust force being not able to overcome the longitudinal friction force. Hence, a higher maximum steering angle can be observed at higher thrust level.

This bifurcation diagram gives information on whether there exists an equilibrium state at a specific speed and steering angle. But it does not provide any stability information when the aircraft is shifting from one equilibrium to another. The aircraft may take a very long time to reach the equilibrium state, especially when the control input is changing rapidly. This is why we need to perform dynamic simulations to analyse transient behaviours.

### 2.3.2 Varied CG position

The stability of the aircraft is affected by CG position. Specifically, for an aircraft moving on the ground, a change of CG position would change the weight distribution on different landing gears. In turn, the vertical load largely affects the maximum lateral force that a tyre can generate. In addition, the CG position determines if the aircraft understeers or oversteers. In view of this, a bifurcation analysis is performed to study how the stable turning solutions vary with the CG position.

In this section, the continuation runs are initiated from the same straight-line velocity of $20m/s$. Each continuation run has a fixed CG position in the range 20% to 35% MAC. The steering angle is varied between 0° and 90° as a single continuation parameter. The bifurcation diagram is shown in Fig.2.5 which illustrates four stable branches at four different CG positions.

In the bifurcation diagram, the lateral acceleration is plotted against steer-

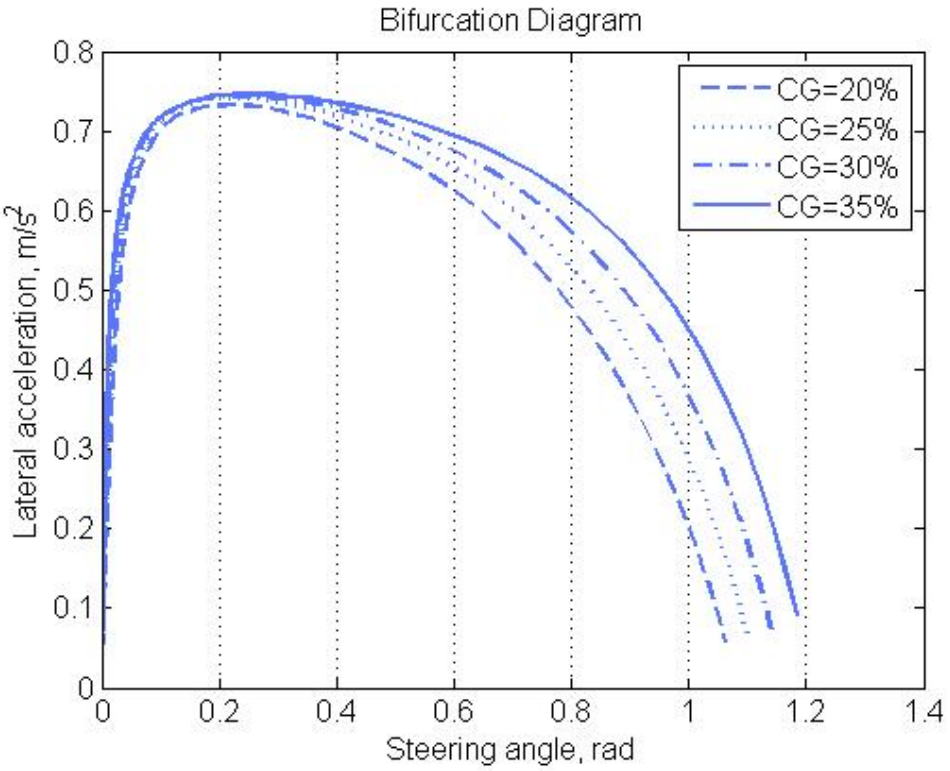


Figure 2.5: Bifurcation diagram for different CG positions.

ing angle. For steering angles less than 0.2rad (11.46°), very little difference can be seen between different CG positions. As the steering angle increases, we can see significant differences in lateral acceleration. Specifically, an aircraft with a more rearward CG position is able to follow a tighter turning circle hence achieving higher lateral acceleration. When the CG is moving from a forward position to a backward position, the aircraft will change from understeer to oversteer which makes it more difficult to be stabilized by a controller. Since the aircraft typical CG position when taxiing on the ground is about 30%MAC, which makes it oversteer, the controller should be designed and tuned at this CG position.

### 2.3.3 Varied coefficient of friction

In addition to CG position, the runway surface condition is another factor that significantly affects the aircraft ground dynamics and the range of valid operation. Taxiing on contaminated runways leads to increased risk of skidding hence loss of control on the ground. Once rudder effectiveness is lost at lower speed, directional control and deceleration difficulties on a contaminated surface may greatly increase. Reduced nose gear wheel adhesion directly limits both steering input options and the usual directionally stabilising effect of the nose gear.

To simulate different runway conditions, the original tyre model is multiplied by a normalised coefficient of friction which is varied between 0 and 1. Thus the lateral force generated by the tyre is rescaled on different runway con-

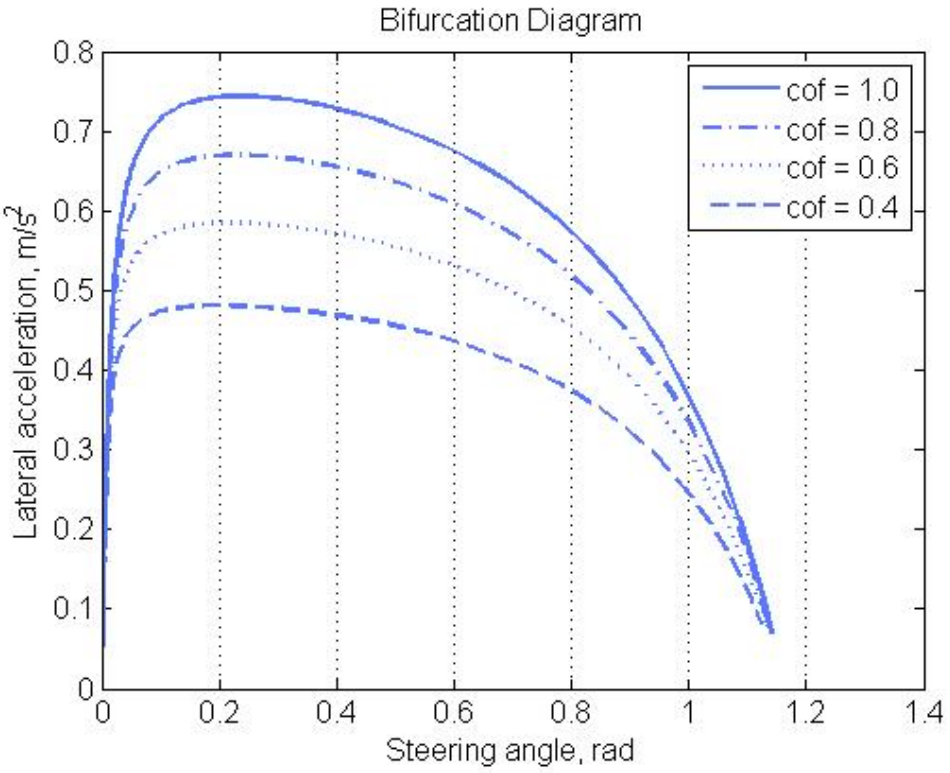


Figure 2.6: Bifurcation diagram for different coefficient of friction.

ditions. Bifurcation analysis is executed to monitor system stability at discrete levels of coefficient of friction ranging from 0.4 to 1.0. Again the continuation runs start from the same straight-line velocity of $20m/s$. The nominal CG position of 30%MAC is considered. For different runway conditions, the required thrust force to maintain the given constant straight-line velocity is identified by a PI controller.

The bifurcation diagram in Fig.2.6 shows four stable branches with different coefficient of friction. It can be seen that on a runway with lower coefficient of friction, the lateral acceleration is significantly reduced. This is because the tyres cannot generate as much lateral grip as on a dry surface (cof = 1), hence the aircraft follows a larger turning circle. In view of the dramatic change in steady turning solutions on different runways, the controller should be redesigned and tuned for various coefficient of frictions, and further robustness study should be performed considering the uncertainties in runway contamination.

## 2.4 Dynamic simulation

Dynamic simulation is used to investigate time varying behaviour of a system which is typically described by ordinary differential equations. It is done by stepping through a time interval and calculating the integral of the derivatives. Some methods use a fixed step through the interval, and others use an adaptive step that can shrink or grow automatically to maintain an acceptable error tolerance.

In this section, a classic $4^{th}$-other Runge-Kutta method with fixed time step is used to calculate system states from the initial condition. The aircraft is on the nominal configuration with total mass of 54500kg and CG position of 30%MAC. Open loop simulations help to understand how the dynamical system respond to different control inputs, and how the intermediate states (e.g. tyre slip angle and loads) behave at different speeds and/or lateral accelerations. Various simulations are considered here including step-input response

and a 45-degree runway exit manoeuvre with prescribed steering angle.

In comparison with bifurcation analysis which doesn't capture transient behaviours, dynamic simulations are able to analyze the aircraft's stability at any instant. Since the aircraft model is a white box model, all the states of the aircraft are accessible. It can provide an insight into the dynamical system by monitoring the aircraft's velocities, attitude, and force components acting on the aircraft during the simulations.

### 2.4.1 Step response

The step response of a system in a given initial state consist of the time evolution of its outputs when its control inputs are step functions. Knowing the step response of a dynamical system gives information about the transient response of the system, and on its ability to reach one stationary state when starting from another. From a practical point of view, knowing how the system responds to a sudden input is important because the deviation from the long term steady state may have significant effects on the overall system. In this section, we consider a scenario where no brake is applied, while thrust force is kept constant so that the aircraft moves in a straight line at a given speed. Simulations start from the same equilibrium point with a fixed speed of $20m/s$. A step input of steering enters the system at time $t = 0$. Two constant steering angles (4 degrees and 5 degrees) are tested with the same aircraft configuration, showing qualitatively different transient behaviours respectively.

A simulation time of 40s is considered here. The steering angle is kept constant at 4 or 5 degrees throughout the simulation while the thrust force remains at 5290N. The simulation results are illustrated in Fig.2.7, with the first column showing the result for the steering angle of $4^\circ$ and the second column showing result for $5^\circ$.

The stable and unstable aircraft CG trajectories are illustrated in the top panels respectively, with the aircraft's global position and attitude marked every 5s by an aircraft icon. In the top left panel, the aircraft is gradually

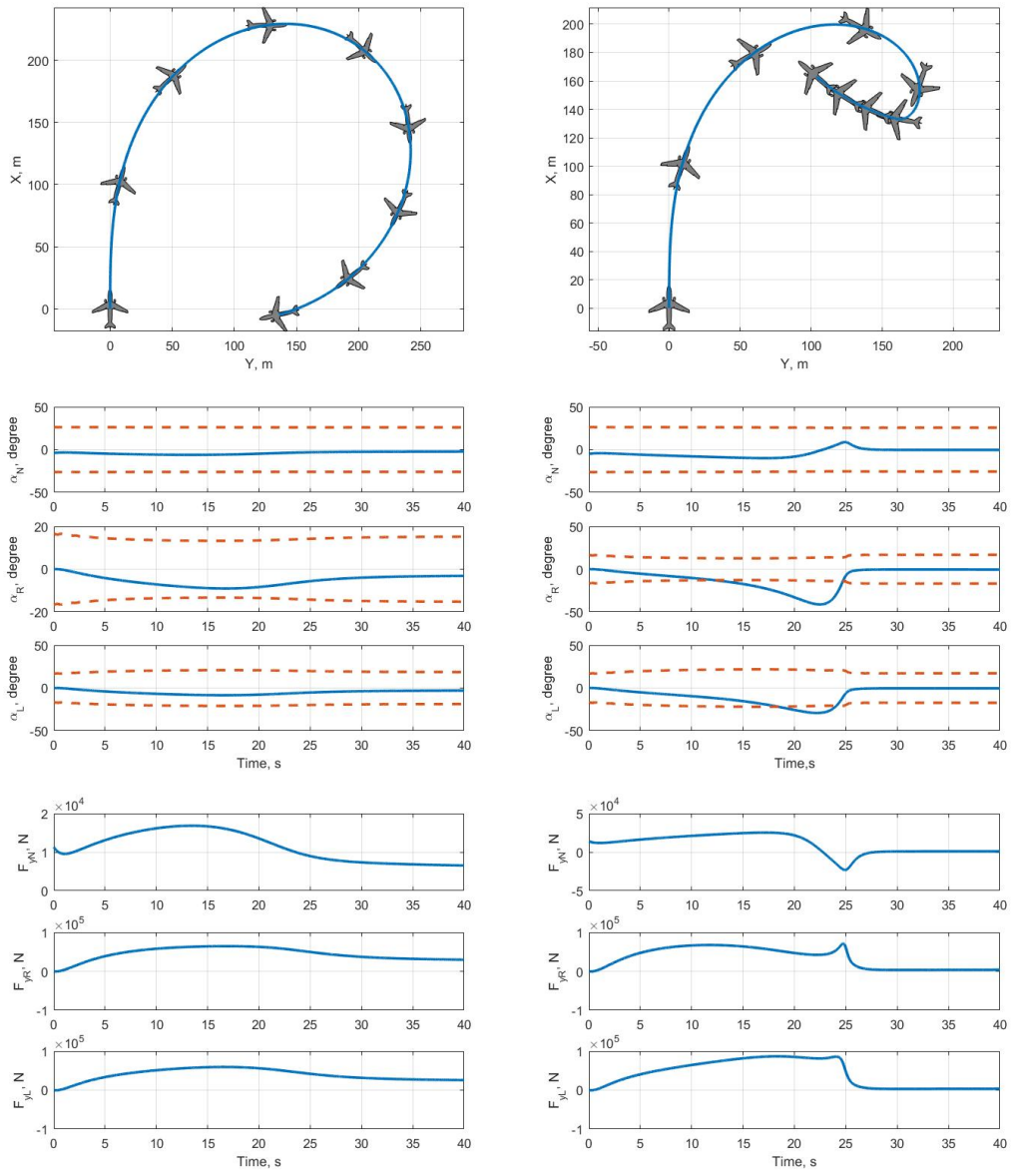


Figure 2.7: Aircraft CG trajectories, slip angles, and lateral friction forces on each gear.

entering a steady turning circle; in contrast, the aircraft in the top right panel is skidding at some point due to the saturation of main gears. To study the behaviours of each landing gear, the slip angle (solid line) and optimal slip (dash line) on nose, right and left gear are plotted in the middle panels respectively; the lateral force generated by each gear are plotted in the bottom panels respectively. As a result of weight transfer, the reduction of the vertical load on the right gear makes it saturate first; the left gear saturates afterwards and the aircraft starts to skid. The reduction of the lateral force on the main gears can be seen in the bottom right panel. The aircraft forward speed drops dramatically due to skidding. Because of the aircraft's speed reduction, the main gears are recovered from saturation and the aircraft regains stability. Nonetheless, due to the large inertia, it will take a long time to accelerate and then achieve a new equilibrium.

The previous bifurcation analysis result shows that the aircraft at a forward speed of $20m/s$ is stable over the steering angle ranging from $0°$ to $65°$. Nonetheless, as shown by this step response simulation, the transient behaviour turns out to be unstable during the simulation before it settles down to the long term steady state. Combining these two methods, we are able to have a closer look into the aircraft ground dynamics.

### 2.4.2 $45°$ runway exit

Before a controller is developed for the aircraft, an open-loop simulation with made-up steering input is an easy way to investigate a specific ground operation. In this section, we simulate a $45°$ runway exit manoeuvre at $20m/s$ with prescribed steering angle as shown in Fig.2.8. The steering angle is defined as:

$$\delta = \frac{\tanh(t - T_a) - \tanh(t - T_b)}{2}\delta_0 \tag{2.59}$$

This nominal steering angle is tuned via $T_a$, $T_b$ and $\delta_0$. Their values are chosen to negotiate this turn as $T_a = 5s$, $T_b = 11s$, and $\delta_0 = 5°$.

The simplified $45°$ runway geometry is illustrated in Fig.2.9 Panel(a). This

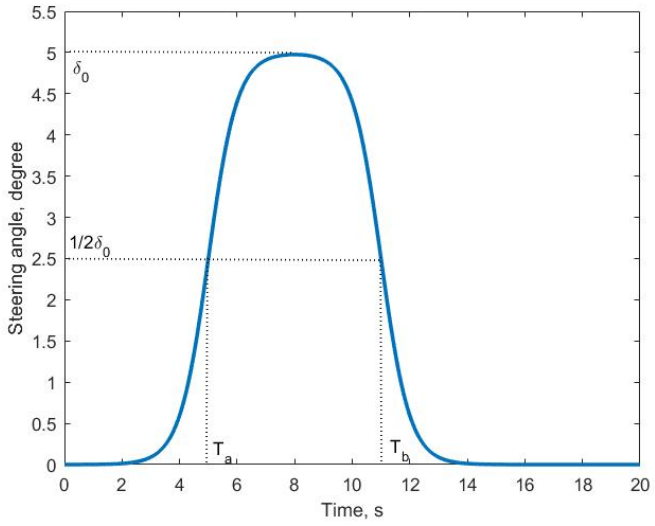


Figure 2.8: Steering angle for 45° runway exit

runway is $40m$ wide, consisting of two line segments and an arc segment. The aircraft starts the simulation from the location (-200,0). As can be seen from the aircraft trajectory, with the predefined steering input, the aircraft is able to execute this exit manoeuvre within the runway's boundaries. Panel(b) shows the slip angles (solid curves) and optimal slips (dashed curves) on each landing gear. It can be seen that the slip angle on each landing gear is lower than the optimal slip, $\alpha_* \in (-\alpha_{opt*}, \alpha_{opt*})$, which means all the gears retain sufficient grip throughout this manoeuvre. This margin of lateral slip indicates that the tyre has capability of generating more lateral force. In other words, the aircraft is able to make this exit manoeuvre at a higher speed.

Considering a typical runway exit speed is $10 - 15m/s$, this simulation demonstrates a high speed exit with manually tuned steering angle. This research aims to develop a real-time optimal controller which can potentially automate aircraft ground manoeuvres. It would significantly improve the efficiency and safety of fast runway turn-offs. The details of the controller design are presented in the following chapters.

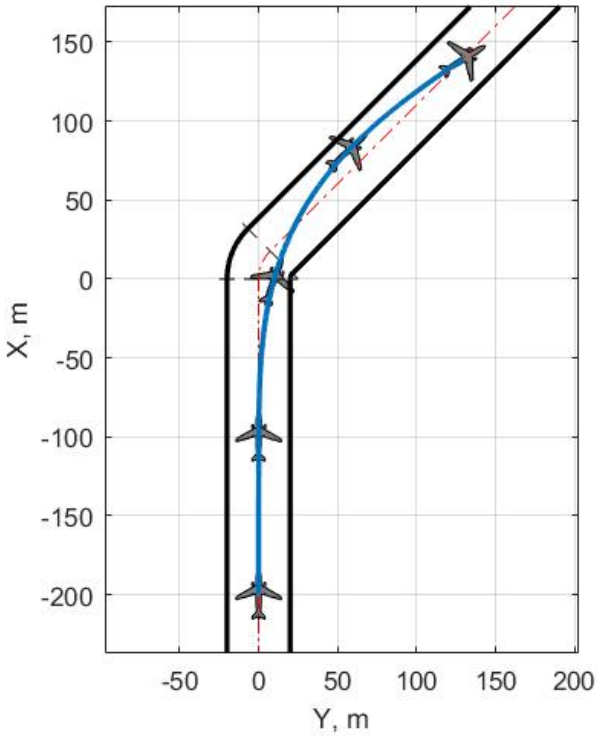


(a) Aircraft trajectory

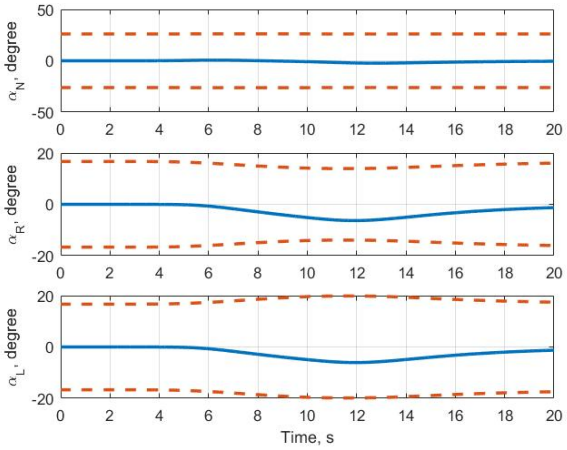


(b) Slip angels

Figure 2.9: Aircraft trajectory and slip angle on each gear for 45° runway exit.

## 2.5 Concluding remarks

A fully parameterised nonlinear aircraft model is presented. Its white box nature provides accessibility to all the aircraft states. For aircraft ground dynamics, the most important nonlinear effects come from tyre/ground forces. A realistic combined slip tyre model is proposed with parameters chosen to represent nose and main landing gear respectively. To study the stability of the proposed aircraft model and its ground dynamics, we have employed two mathematical tools: bifurcation analysis and dynamic simulation. Bifurcation analysis provides a global picture of aircraft steady turning circle solutions with varied control inputs and operational parameters. The bifurcation diagrams illustrate how turning solutions change with thrust force and steering angle over various CG positions and runway conditions. Specifically, the aircraft tends to follow a tighter circle with a more rearward CG position and on a less contaminated runway. Knowing this fact is important when designing a real-time controller for aircraft ground manoeuvring because it would potentially improve the control law's stability and robustness.

In conjunction with bifurcation analysis, dynamic simulations are employed to investigate aircraft's transient behaviours when subject to a specific control input. Two types of simulations are considered: step response to steering input and a runway exit manoeuvre with nominal steering input. Unstable transient behaviours can be observed when a 5$\circ$ steering step input is applied to the nose-gear. This short period of losing stability is not desired and can be dangerous for ground operations. Although the aircraft would finally reach an equilibrium state as shown in the bifurcation diagram, we should always make sure that the aircraft is controllable throughout the taxiing period. In terms of the 45° runway exit manoeuvre at $20m/s$, it can be achieved via a manually tuned steering input. It provides an example for manually operated runway turnoff which can later be compared with a controller automated one.

# Chapter 3

# An Expert Pilot Model

## 3.1 Introduction

Automation of aircraft ground manoeuvres can effectively reduce the workload for pilots and improve efficiency and safety of airport operations. In this chapter we present an Expert Pilot Model (EPM) for aircraft steering control on the ground, based on which we can study ground manoeuvres manually operated by pilots. It can be tuned to an expert level so as to investigate the best possible high-speed manoeuvres on the ground. This pilot model is developed on the basis of a simple realistic driver model which is initially developed for ground vehicles. Driver modelling can be used to support Advanced Driver Assistance Systems (ADAS) and autonomous vehicle research. In this research, the driver model we are referring to is originally proposed by Best [49], motivated by the author's belief that the driving task actually uses single point preview. For everyday driving, the driver tracks a section of the road ahead by continuously adapting the steering, and the vehicle will be kept on a path towards a single reference point in front of it. The proposed model is reasonably simple compared to many disproportionately complicated driver models. It is demonstrated to be capable of matching measured steering behaviour in various scenarios.

Here we take advantage of the driver model and adapt it to this aircraft application. This method does not depend on knowledge of the vehicle's dynamics. It is based on a single preview point which is the estimation of future coordinates of the aircraft. The single preview point is located by projecting along a steady turning circle, which is determined by the vehicle's current speed, steering angle, and understeer gradient. In the original model, steering control is solely based on correction of the current steering angle given the predicted lateral deviation from the target path. Since the aircraft model in this research has huge yaw moment of inertia, the system response to steering correction will experience large delay, causing the aircraft to oscillate about the target path. To overcome this disadvantage, we explore a modified path following controller by adding an additional feedback gain in terms of the current yaw angle. By doing this, the aircraft movement is better stabilised around the body-fixed yaw axis. Some previous ground vehicle driver models have proposed the influence of yaw feedback control [53] but it is partially appropriate for aircraft motion; we assume that pilots sitting in the cockpit have a feeling for the aircraft yaw rate, because their position is so far forward of the CG.

To keep the aircraft on a given path while taxiing, pilots choose either the nose-gear or CG as a reference point. They develop a feel for the nose-gear and CG positions behind them. In this chapter we simulate both types of standard path following manoeuvres using both reference points. Three different runway exit geometries are simulated: 30°, 45°, and 90°. The maximum exit speed on each runway geometry is identified. Both the original driver model and the improved version (Expert Pilot Model) are tested and compared at a range of discrete forward velocities. Lastly, a robustness study is performed to investigate the proposed controller's stability in presence of disturbances in the operational parameters (e.g. mass and CG) and environmental conditions (e.g. contaminated runway and crosswind).

## 3.2 Controller design

Prior to the controller design, we consider a particular problem with path following on the ground; generation of an accurate but computationally simple representation of the reference path. Here we use a linearly interpolated target path given a set of coordinates. Its accuracy can be improved by refining the linear path segments if required. Initially, the proposed path following controller is implemented exactly the same as the original driver model [49]. The driver model's performance, however, is unsatisfactory at high-speed due to oscillations in the steering input. Motivated by this fact, we developed an improved version of the driver model, i.e. Expert Pilot Model.

### 3.2.1 Driver model

With no attempt to mimic human pilot behaviour, the original driver model for ground vehicles can be directly employed to achieve aircraft ground path following tasks. The driver model is designed based on the single preview point method as illustrated in Fig.3.1. Since the amount of look-ahead varies with speed, a finite preview time $T_p$ is considered. The forward prediction of the aircraft coordinates at preview time $T_p$ is based on the assumption that the aircraft is in steady-state circular motion if the current steering angle is maintained. By projecting along the current circular arc, the preview point $P$ is located. It is notable that there are errors with this preview point due to the steady state assumption. The effect of these errors, however, can be minimised by tuning the controller's parameters.

At any instant $k$, the steady-state turning radius under fixed steering angle and forward speed is given by the steady-state handling equation:

$$R(k) = \frac{L + K_{ug} V_x(k)^2/g}{\delta(k)} \tag{3.1}$$

where: $L$ is the aircraft wheelbase which is $l_{xN} + l_{xR} = 12.6840m$; $K_{ug}$ is the understeer gradient which is used to describe a vehicle's sensitivity to steering.

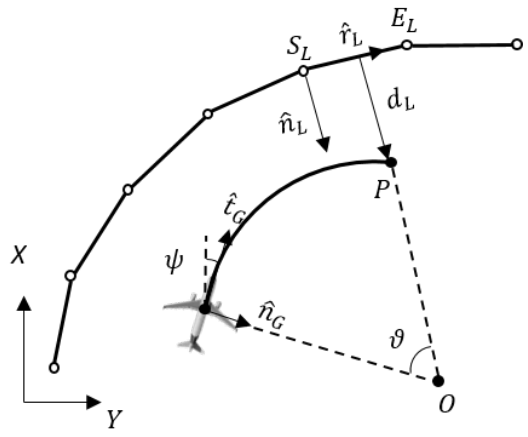


Figure 3.1: Calculation of preview point and lateral deviation from linear reference path.

It is a measure of how the difference between the front wheel's and rear wheel's slip angles change with lateral acceleration given as:

$$K_{ug} = -\frac{(\alpha_N - \alpha_R/2 - \alpha_L/2)}{V_x W_z} \tag{3.2}$$

Specifically, if the nose gear's slip angle is larger than the average of right/left gears' slip angles (negative understeer gradient), the aircraft shows oversteer and it is more sensitive to changes due to lateral acceleration; conversely, if the understeer gradient is positive, the aircraft shows understeer and it is less sensitive to changes due to lateral acceleration; if the understeer gradient is zero, the aircraft is neutral. Since aircraft are highly nonlinear systems, it is normal for the understeer gradient to vary over the range of lateral acceleration. It is possible for the aircraft to understeer in some conditions and oversteer in the others. In the proposed controller, we assume a constant understeer gradient. The choice of its value will be discussed later.

Unit vectors are found by rotation of the global X facing vector through $\psi$

$$\hat{t}_G = \begin{bmatrix} \cos(\psi) \\ \sin(\psi) \end{bmatrix}, \quad \hat{n}_G = \begin{bmatrix} -\sin(\psi) \\ \cos(\psi) \end{bmatrix} \tag{3.3}$$

and the angle traversed along the arc is:

$$\vartheta = V_x T_p / R \tag{3.4}$$

The preview point $P$ is located via the arc centre $O$:

$$P = G + R\hat{n}_G - \begin{bmatrix} \cos\vartheta & -\sin\vartheta \\ \sin\vartheta & \cos\vartheta \end{bmatrix} R\hat{n}_G \tag{3.5}$$

The reference path is a linearly interpolated trace of X, Y locations in the ground coordinate system. To determine the shortest distance from the preview point $P$ to the target path, a valid line segment needs to be identified in the first place. A segment is valid if

$$0 < |(P - S_L) \cdot \hat{r}_L| < |\hat{r_L}| \tag{3.6}$$

$$\hat{r}_L = E_L - S_L \tag{3.7}$$

Checking all segments is computationally expensive. What's more, since the line segment track is strictly discontinuous in gradient, it is possible that two or zero valid segments exist. To avoid both of these problems, the preview point $P$ will only progress forward along the track, so the track segment index $i$ can only stay the same or increase. At each new time step, the previously valid segment $i$ is retained and incremented as required according to

$$\text{while} \quad |(P - S_L(i) \cdot \hat{r}_L(i)| > |\hat{r}_L(i)|, \quad i = i + 1 \tag{3.8}$$

The signed deviation from the target path $d_L$ at a single preview point is then calculated:

$$d_L = (P - S_L) \cdot \hat{n}_L \tag{3.9}$$

The steering control is then solely based on correction of this deviation from the target path. A simple integral controller with respect to $d_L$ is used to determine the steering angle required:

$$\delta_{k+1} = \delta_k + K_{lat} d_L \tag{3.10}$$

### 3.2.2 Development of driver model

Although the original driver model works properly with ground vehicles, it has poor path following performance in an aircraft application, struggling to follow a given path especially at high speed. Specifically, it over-corrects the aircraft due to its massive yaw moment of inertia, ending up with a delayed and oscillatory system response. To improve the controller's performance, we consider further development of the original driver model. Firstly, we have implemented a full PID controller:

$$\delta(t) = K_p d_L(t) + K_i \int_0^t d_L(t)dt + K_d \dot{d_L}(t) \tag{3.11}$$

The PID controller is properly tuned via $(K_p, K_i, K_d)$ in a wide range of values. The well tuned PID controller does not show any advantage over the original controller; indeed, it has similar path following performance as the original one. From the tuning of parameters, we have noticed that the controller is dominated by $K_i$ while $K_p$ and $K_d$ are significantly smaller than $K_i$; the PID controller becomes effectively a single integral controller. The main reason behind this lies in how we estimate the preview point. Different from many other path following controllers which predict the preview point by a straight line projection, we calculate the preview point via the steady state handling equation based on current speed and steering angle. Specifically, the previewed lateral deviation $d_L$ directly depends on the instantaneous steering input. In view of long preview time and huge aircraft inertia, the proportional term will lead to significant over-corrections of the steering angle due to the movement of preview point being prior to the movement of aircraft CG.

Sharp et al. [53] propose a mathematical model for driver steering control which is based on two state feedback signals: one is the vehicle lateral offset from the current intended position on the given path; the other one is the difference between the vehicle attitude angle and the tangent angle of the intended path at the current position. The state feedback control gains proved to be very important in improving the system stability. Particularly,

the vehicle attitude error feedback control would improve the performance of the drive model for vehicles made artificially unstable by strong oversteer. In this research, we use a negative feedback gain $K_{yaw}$ with respect to the difference between current yaw angle and the angle of target line segment $\varphi_r$, proved to be able to effectively reduce overshoot and oscillations:

$$\delta(t) = \frac{K_{lat}}{\Delta t} \int_0^t d_L(t)dt + \frac{K_{yaw}}{\Delta t}(\varphi(t) - \varphi_r(t)) \tag{3.12}$$

The control law in discrete form is

$$\delta_{k+1} = \delta_k + K_{lat}d_L + K_{yaw}W_z \tag{3.13}$$

The contribution of the yaw angle feedback control tends to reduce the steering angle by adding damping. As a result, the aircraft will cut the corner, being more deviated from the centreline. The contribution of lateral deviation control could compensate for the negative contribution of yaw angle control. Hence, $K_{lat}$ and $K_{yaw}$ should be tuned together to achieve a satisfactory performance. Some guidance for the proper setting of the proposed controller is given in the next section.

## 3.3 Parameter optimisation

The proposed controller is simple, effective, and computationally efficient. It can be tuned via a couple of parameters, e.g. preview time $T_p$, understeer gradient $K_{ug}$, and proportional gains $K_{lat}$ and $K_{yaw}$.

Preview time $T_p$ is an important parameter which directly affects the timing of the steering input. With a longer preview time $T_p$, steering actions will be applied earlier for a given corner due to longer lookahead distance. By doing this, lower magnitude of steering angle will be held for a longer duration, inducing corner cutting. In contrast, a shorter preview time $T_p$ causes aggressive steering actions with higher magnitude of steering angle held for a shorter duration. Therefore, an appropriate preview time is needed for the controller

to perform a stable path following. An initial guess of $T_p$ is 5s considering the delay in the aircraft's response to steering. It can be optimised later with the other parameters fixed at a reasonable value.

Given by Eqn.3.1, the steady-state turning radius for a given steering angle and speed is determined by wheelbase $L$ and understeer gradient $K_{ug}$. Specifically, while $L$ is fixed, a larger $K_{ug}$ would enlarge the expected radius, reducing the aircraft's sensitivity to steering input. For the aircraft, understeer gradient is a nonlinear function of forward speed and lateral acceleration. Its actual value is identified through steady-state turning solutions at constant forward speed. Firstly, a PI controller is used to maintain the aircraft forward speed $V_x$:

$$F_{xTR,L} = 1 \times 10^5 * (V_x(t) - V_c) + 1 \times 10^2 * \int_0^t (V_x(t) - V_c)dt \tag{3.14}$$

During the 45° runway exit manoeuvres, the forward speed is maintained at the target level $V_c$ with an error $\pm 0.5 m/s$. Fig.3.2 illustrates the time history

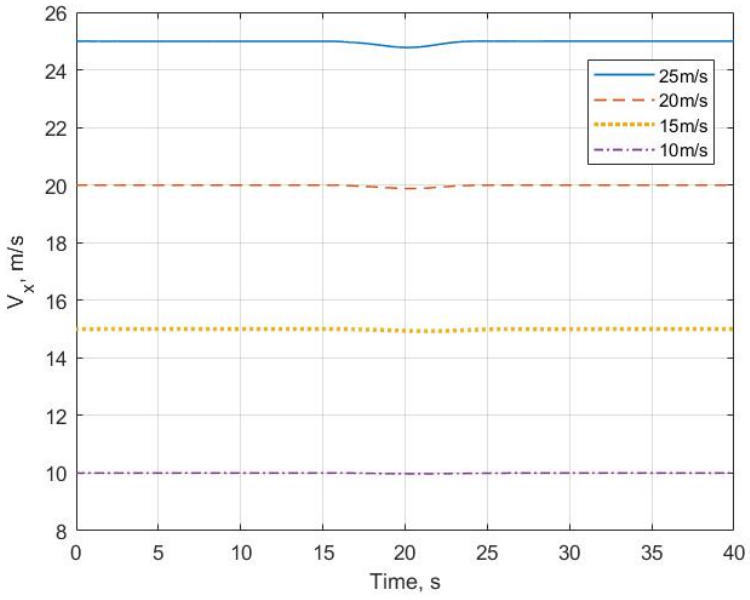


Figure 3.2: Forward speed under the control of the PI controller.

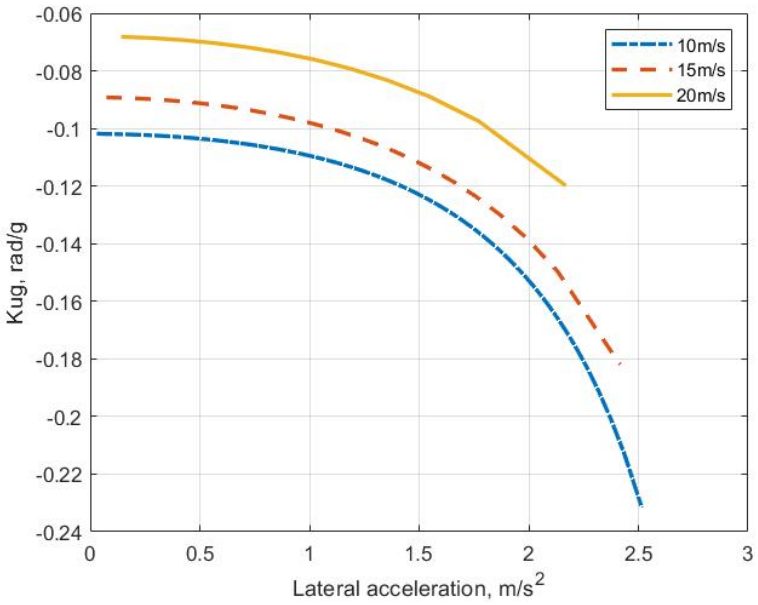


Figure 3.3: Understeer gradient at different speeds and lateral accelerations.

of forward speed at various levels.

Then the steering angle slowly ramps up going through all the stationary solutions; by computing the slip angle on each gear, $K_{ug}$ is identified by Eqn.3.2. The variation of understeer gradient at different speed is illustrated in Fig.3.3. Within the range of speed that we are interested in $(10m/s - 20m/s)$, the aircraft shows oversteer, which becomes greater at higher speed and/or higher lateral acceleration.

The transition from one stationary solution to another usually takes a long time; it might take 30s to enter a steady turning circle from rolling in a straight line, as shown in Fig.2.7. Considering 5s of lookahead is a relatively long period, using the actual $K_{ug}$ for the future path prediction would result in a massive error. To compensate for the delay in the steering response, we use higher understeer gradient in the handling equation, which means lower sensitivity to steering input and hence a larger turning radius. The $K_{ug}$ value used here at low, medium and high speed is 0.4, 0.7 and 2.0 respectively.

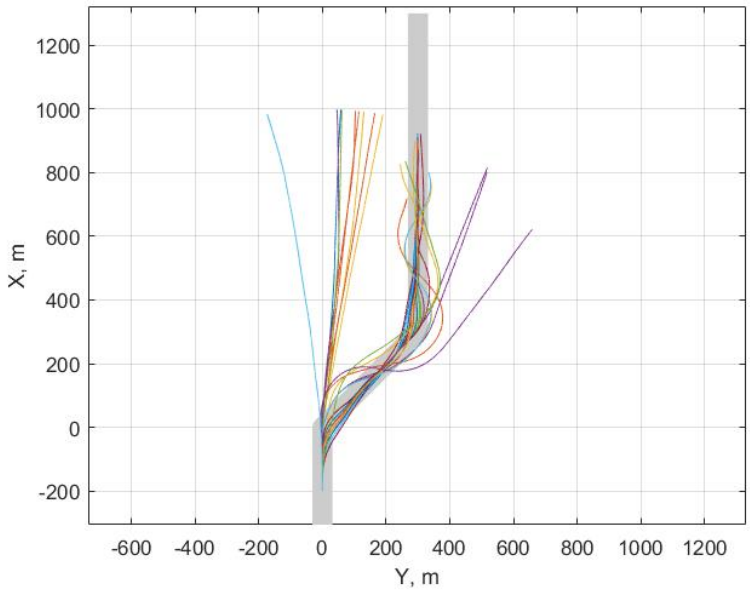


Figure 3.4: Aircraft trajectories at various combinations of $T_p$ and $K_{lat}$

Although $K_{ug}$ and $T_p$ are not exactly orthogonal in their effect, they have distinctly different effects on the controlled response.

Additionally, the proportional feedback gain $K_{lat}$ can be tuned although its effect on steering behaviour is strongly coupled to $K_{ug}$. However, independent tuning is not useful. The initial guess for $K_{lat}$ is 0.01. Lastly, the proportional feedback gain $K_{yaw}$ is tuned to stabilize the aircraft yaw motion. A negative $K_{yaw}$ is used to reduce the increment of steering angle, with its magnitude affecting the maximum lateral acceleration that the aircraft would experience. Specifically, a higher magnitude of $K_{yaw}$ would result in less steering input hence lower lateral acceleration. $K_{yaw}$ and $K_{lat}$ are complementary to each other; an aggressive steering input caused a large $K_{lat}$ can be balanced by tuning $K_{yaw}$. The initial guess for $K_{yaw}$ is -0.01.

Now we consider optimisation for these parameters. By using a simple greedy method, we optimise the parameters $T_p$, $K_{lat}$, and $K_{yaw}$ one after another, having $K_{ug}$ fixed at the given value. This optimisation can be iterated if

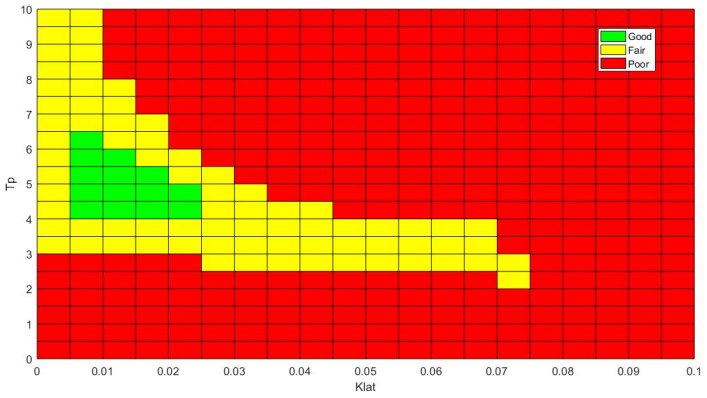


Figure 3.5: Stability map for $T_p$ and $K_{lat}$

required until a fast and stable controller response is achieved. Starting from the initial guesses ($T_p = 5$, $K_{lat} = 0.01$, $K_{yaw} = -0.01$), the lookahead time $T_p$ is firstly optimised over the range of 0 to 10s with an interval of 1s ($K_{lat}$ and $K_{yaw}$ are fixed); then $K_{lat}$ is optimised over the range of 0 to 0.1 with an interval of 0.005 ($T_p$ and $K_{yaw}$ are fixed). The nominal target path considered here is shown in Fig.3.4 as the thick light grey line.

All the simulations are launched from the same equilibrium state, based on the same aircraft configuration (m=54500kg, CG=30%MAC). As can be seen from the aircraft trajectories in Fig.3.4, with various combinations of $T_p$ and $K_{lat}$, the aircraft would stay close to the target path, or perform large oscillations around the path, or become unstable skidding off the path. Fig.3.5 shows how stability varies with different lookahead time $T_p$ and proportional feedback gain $K_{lat}$; the red area indicates the aircraft is unstable; the yellow area indicates the aircraft is able to follow the target path despite the fact that it develops large deviations from the target path; the green area is the "sweet zone" where the aircraft performs good path following with its trajectory staying close to the given path. The combination of $T_p$ and $K_{lat}$ should be tuned to lie in the "sweet zone". Therefore, in this research, the lookahead time is set to 5s, and the proportional gain is set to 0.01.

Finally, we consider the optimisation for the other proportional feedback gain $K_{yaw}$, with the preview time fixed at 5s. The proposed controller is tested with forward speed of 15m/s over a wide range of $K_{yaw}$ (-1 to -0.1) and $K_{lat}$ (0.005 to 0.05). Aircraft trajectories are depicted in Fig.3.6, showing stable and unstable path following solutions. Fig.3.7 illustrates how stability changes with different $K_{yaw}$ and $K_{lat}$. Again, red area indicates unstable solutions; yellow area indicates stable but imperfect solutions; green area indicates the "optimal" solutions with small track error. From these two figures, it can be seen that the proportional feedback gain $K_{yaw}$ could hardly change the controller's stability. However, it does improve the controller's performance with the value between -0.2 and -0.8. A higher magnitude of $K_{yaw}$ makes the aircraft become less responsive to the road curvature, resulting in significant overshoot; whereas a lower magnitude of $K_{yaw}$ might not have enough strength to eliminate the excessive oscillations about the target path through and after the corner. Therefore, a medium $K_{yaw}$ of -0.5 is used at a medium forward

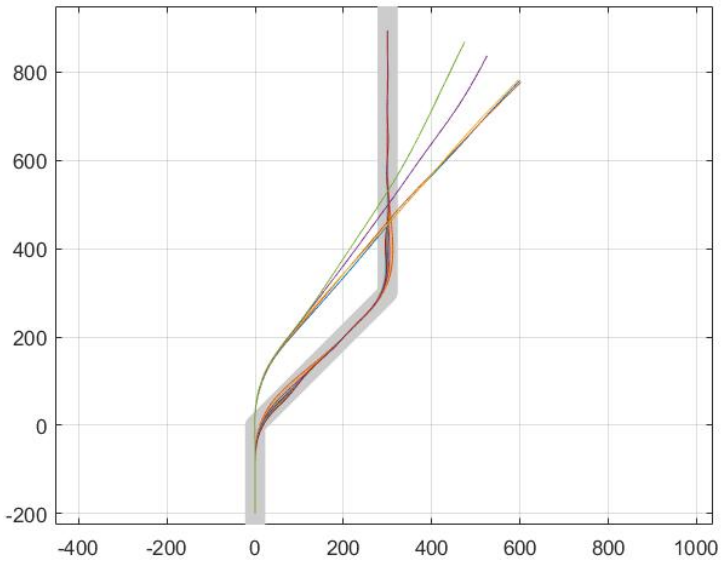


Figure 3.6: Aircraft trajectories at various combinations of $K_{yaw}$ and $K_{lat}$

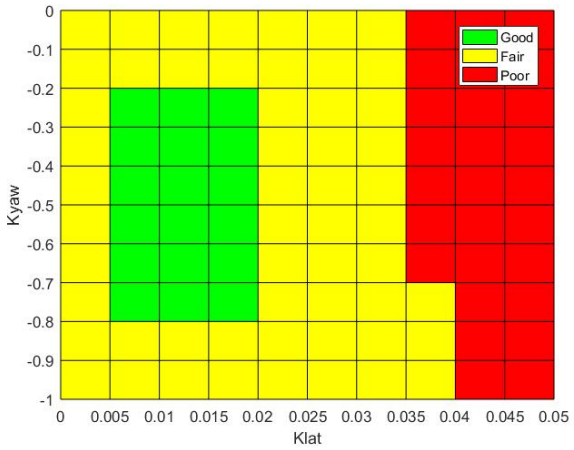


Figure 3.7: Stability map for various combinations of $K_{yaw}$ and $K_{lat}$

speed to improve the proposed controller's path following performance.

## 3.4 Runway exit following the centreline

In this section, we use the proposed Expert Pilot Model to execute a 45° runway exit manoeuvre with either CG or nose-gear following the centreline. Both the original driver model and Expert Pilot Model are examined and compared at a wide variety of forward speed: low speed of $10m/s$, medium speed of $15m/s$, high speed of $20m/s$, and extra high speed of $25m/s$. The runway is assumed to be $20m$ wide, and the maximum lateral deviation allowed is prescribed as $15m$. Thus we are able to identify the maximum speed for 45° runway exit that each controller can deal with.

### 3.4.1 CG following the path

The simulations start from different distance before the corner according to forward speed. In other words, the corner is $20s$ ahead of the aircraft. The forward speed is maintained by a PI controller throughout the simulations. The proportional feedback gain $K_{yaw}$ is retuned at different speeds. The controller

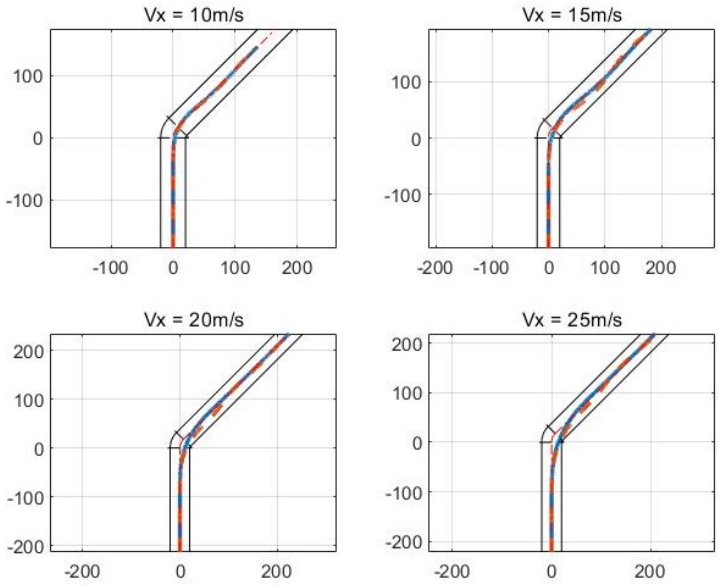


Figure 3.8: Aircraft trajectories of EPM and the driver model at various forward speed.

parameters at different speeds are given in Table.3.1.

Aircraft trajectories of both EPM and the original driver model are shown in Fig.3.8, with solid lines representing EPM and dashed lines representing the driver model. In a low speed case at $10m/s$, the original driver model and Expert Pilot Model deliver similar results with nearly overlapped trajectories. Also it can be seen from their lateral deviation along the path as illustrated in Fig.3.9 that both controllers are able to follow the given path closely with small

| $V_x, m/s$ | $T_p, s$ | $K_{ug}, rad/g$ | $K_{lat}$ | $K_{yaw}$ |
|---|---|---|---|---|
| 10 | 5 | 0.4 | 0.01 | -0.1 |
| 15 | 5 | 0.7 | 0.01 | -0.5 |
| 20 | 5 | 2.0 | 0.01 | -1.0 |
| 25 | 5 | 2.0 | 0.01 | -1.0 |

Table 3.1: Parameters of the Expert Pilot Model controller at different forward speed.

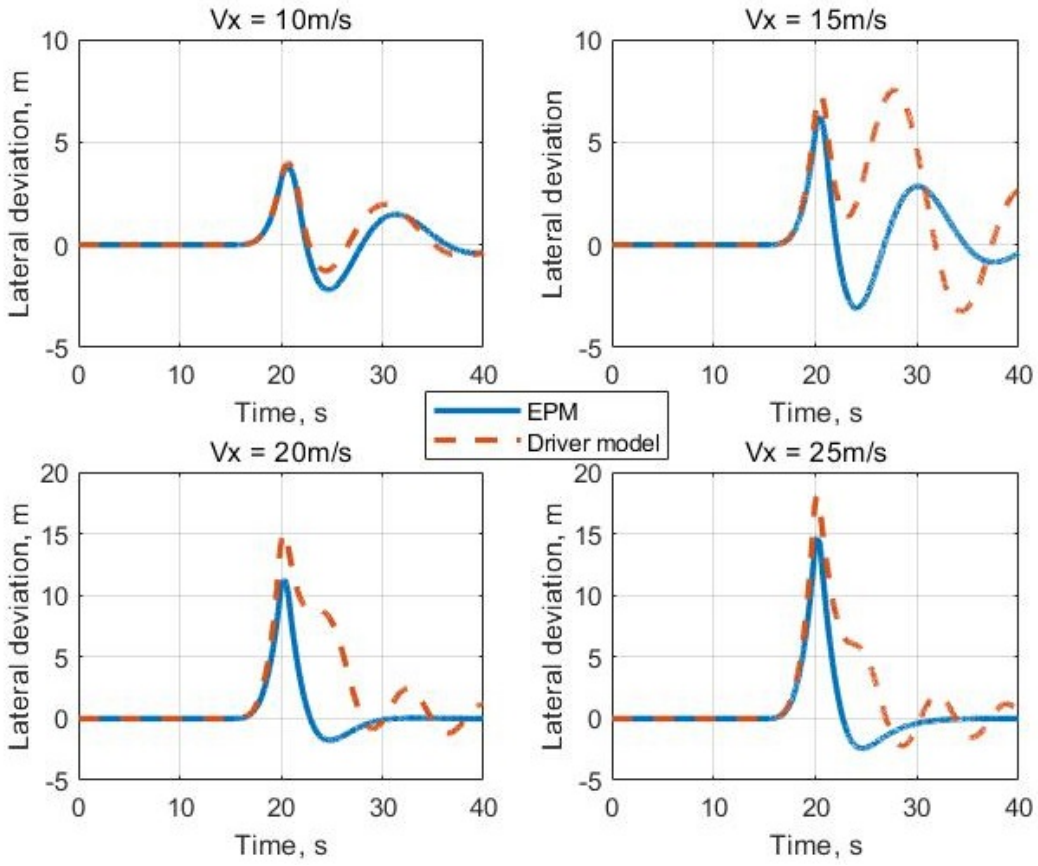


Figure 3.9: Lateral deviation of the aircraft controlled by EPM and the driver model at various forward speed.

lateral deviations; the two controllers have similar steering strategy as shown in Fig.3.10. The aircraft starts to steer at $15s$, exactly when the preview point which is $5s$ ahead of current position enters the corner. Afterwards, it starts to steer in the opposite direction after the corner so as to correct the lateral error and stay on the target path. However, due to the over-correction of steering, an additional oscillation of the steering angle is demanded to eliminate the final steady state error. The variation of steering angle is also reflected in the aircraft lateral acceleration with a $2-3s$ of delay, as depicted in Fig.3.11. The two controllers end up with similar peak lateral acceleration due to their

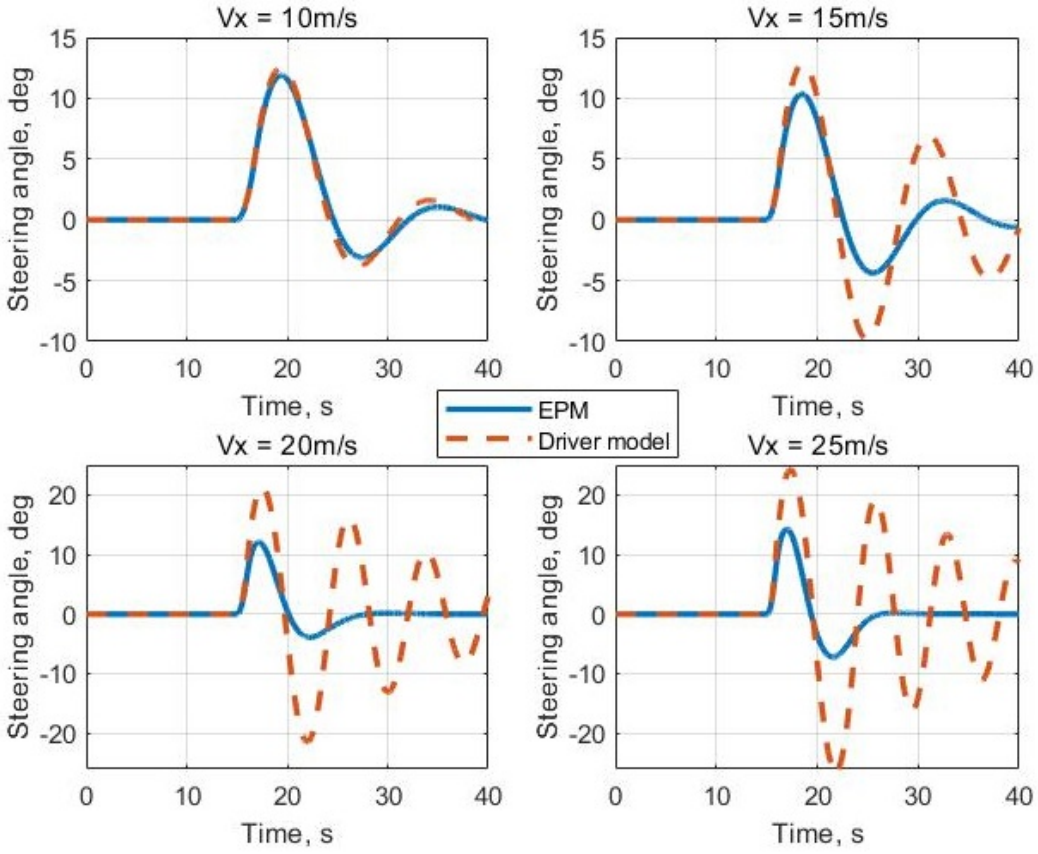


Figure 3.10: Steering angle of EPM and the driver model at various forward speed.

nearly identical steering input. The maximum lateral acceleration experienced through the corner is at a low level around $1.4m/s^2$.

With an increased forward speed, the difference between EPM and the original driver model becomes more significant. At a forward speed higher than or equal to $15m/s$, the difference can be visualised in the trajectories in Fig.3.8. It can be seen that EPM has better performance than the original driver model in this particular task of path following with the aircraft staying closer to the target path. The advantage of EPM is clearly shown by the lateral deviation along the trajectory, as illustrated in Fig.3.9. Obviously we can see

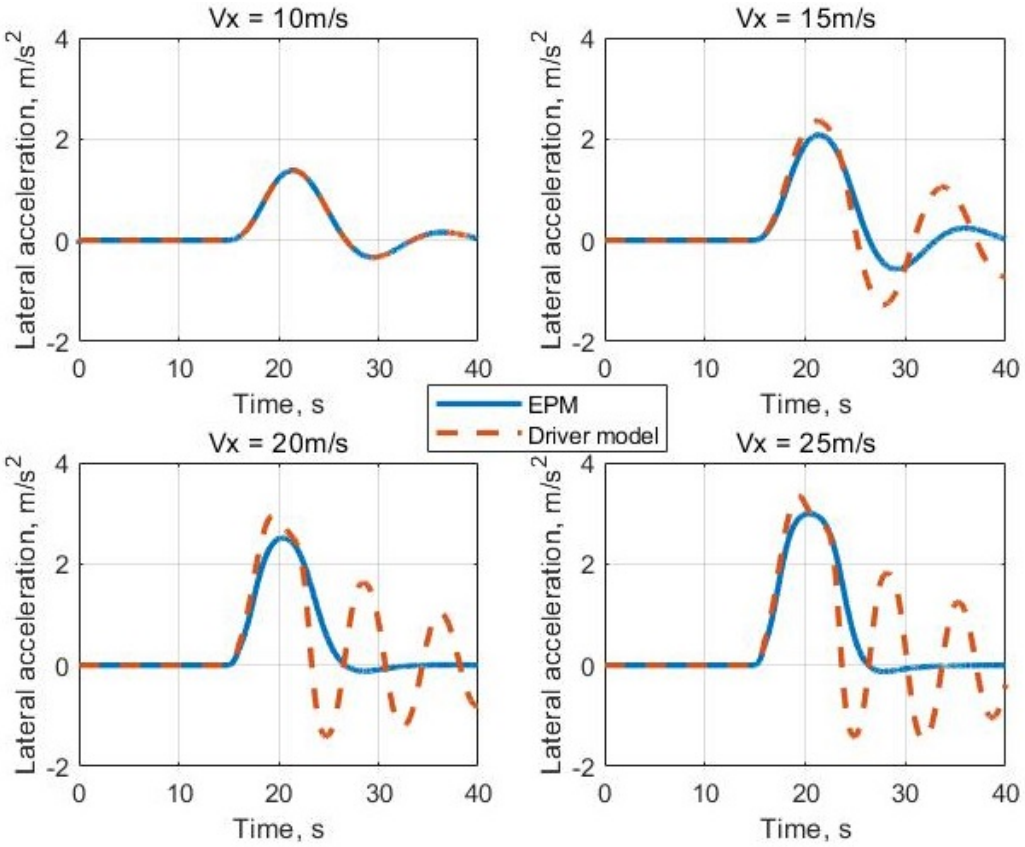


Figure 3.11: Aircraft lateral accelerations of EPM and the driver model at various forward speed.

that the aircraft controlled by EPM has an overall lower level of lateral error compared to the driver model. Considering the constraint on lateral deviation is set as $-15m$ to $15m$, the maximum forward speed that EPM could handle for the 45° runway exit is $25m/s$, whereas the maximum speed that the driver model could handle is $20m/s$.

The steering angles of the two controllers are quite different in magnitude as shown in Fig.3.10. EPM steers the aircraft in an effective and efficient approach without over-correction of steering, while the original driver model applies an excessive oscillation of steering angle. It can be seen that EPM greatly benefits from the additional proportional feedback gain $K_{yaw}$, especially at high

speed, achieving lower track error with even lower control effort. A side benefit that goes with less steering is less tyre wear which could be money-saving for airlines. The aircraft controlled by EPM experiences slightly lower lateral acceleration compared to the driver model as shown in Fig.3.11. Particularly, EPM is able to have the aircraft settle down after the corner straight away.

### 3.4.2 Nose-gear following the path

Since pilots would use either CG or nose-gear as the reference point when following a centreline, we aim to investigate if there is an advantage in using one reference point over the other. In this section, the Expert Pilot Model control is examined at four different speeds ranging from $10m/s$ to $25m/s$ with the nose-gear following the target path. The results are then compared with that of using CG following the target path.

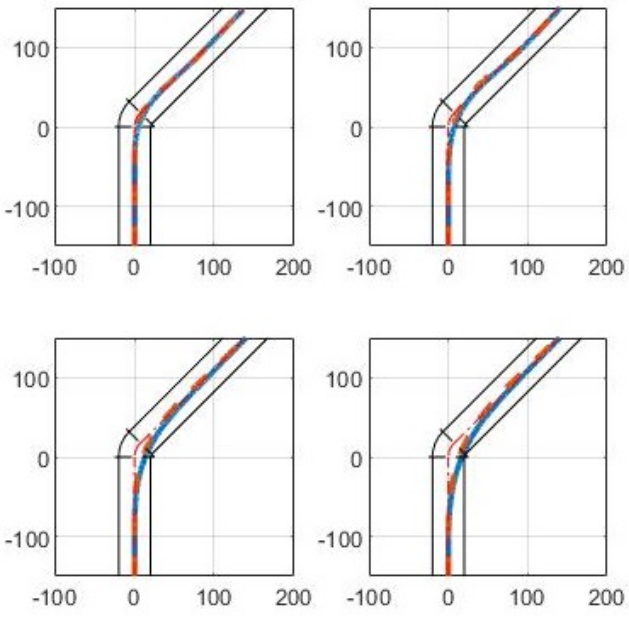


Figure 3.12: Aircraft CG trajectories with nose-gear (solid line) or CG (dashed line) following the centreline.

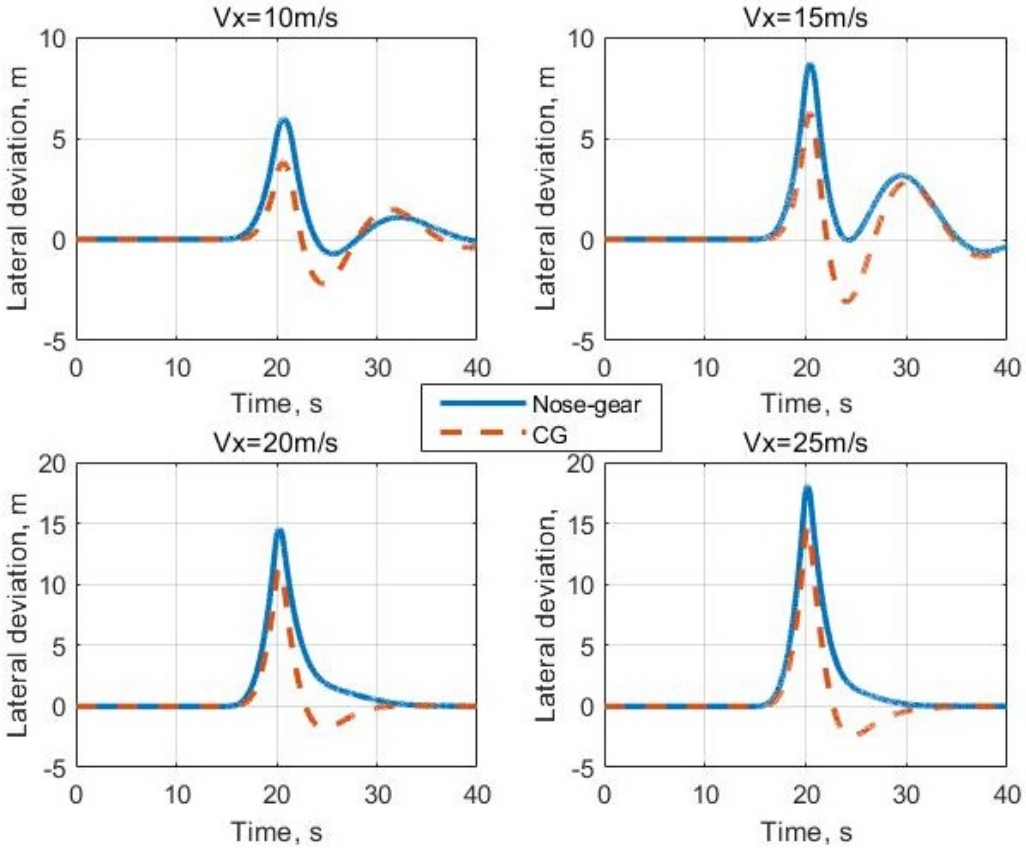


Figure 3.13: Lateral deviations of the aircraft CG.

The pilot model needs to be modified in terms of the calculation of preview point. With the nose-gear following the target path, the single preview point is now an estimation of future coordinates of the aircraft nose-gear:

$$P = G + R\hat{n}_G - \begin{bmatrix} \cos\vartheta & -\sin\vartheta \\ \sin\vartheta & \cos\vartheta \end{bmatrix} R\hat{n}_G + l_{xN} \begin{bmatrix} \cos(\vartheta+\psi) \\ \sin(\vartheta+\psi) \end{bmatrix} \tag{3.15}$$

The controller is then based on this modified preview point. Nose-gear following is compared with CG following, with the same settings of controller parameters. The aircraft CG trajectories are illustrated in Fig.3.12, showing that the aircraft is slightly more deviated from the centreline using nose-gear as the reference point, which can be clearly seen from the aircraft CG's lateral

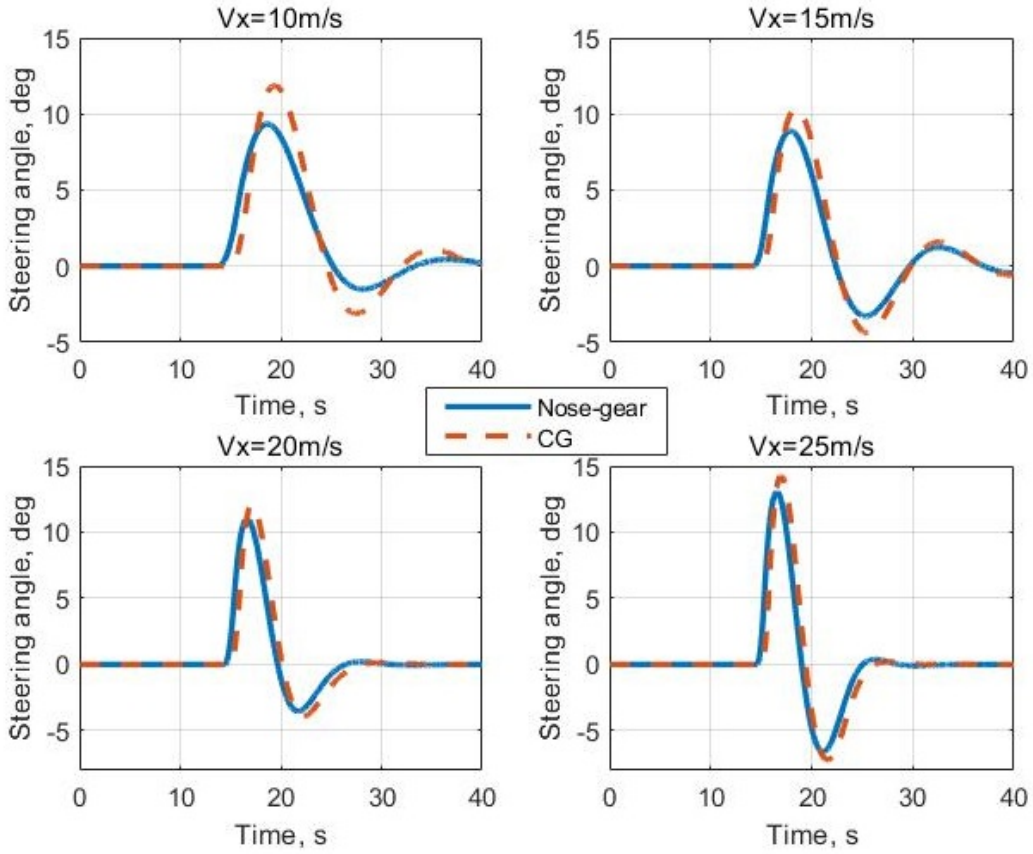


Figure 3.14: Steering angle to follow the centreline with nose-gear or CG.

deviation along the trajectories, as shown in Fig.3.13. At any speed between 10m/s and 25m/s, the aircraft ends up with a higher level of maximum lateral deviation with nose-gear following.

This would affect the maximum speed that the aircraft could handle in a 45° runway exit manoeuvre. In comparison with the case of CG following the centreline where the maximum speed is $25m/s$, it will be reduced to $20m/s$ when nose-gear is used to follow the centreline, since the maximum lateral deviation allowed is $15m$. Nonetheless, following the centreline with the nose-gear can be advantageous over following with CG in some situations. Indeed, the aircraft is not going to overshoot the centreline (no negative lateral deviation), but gradually converges to it after cutting the corner. Additionally, the

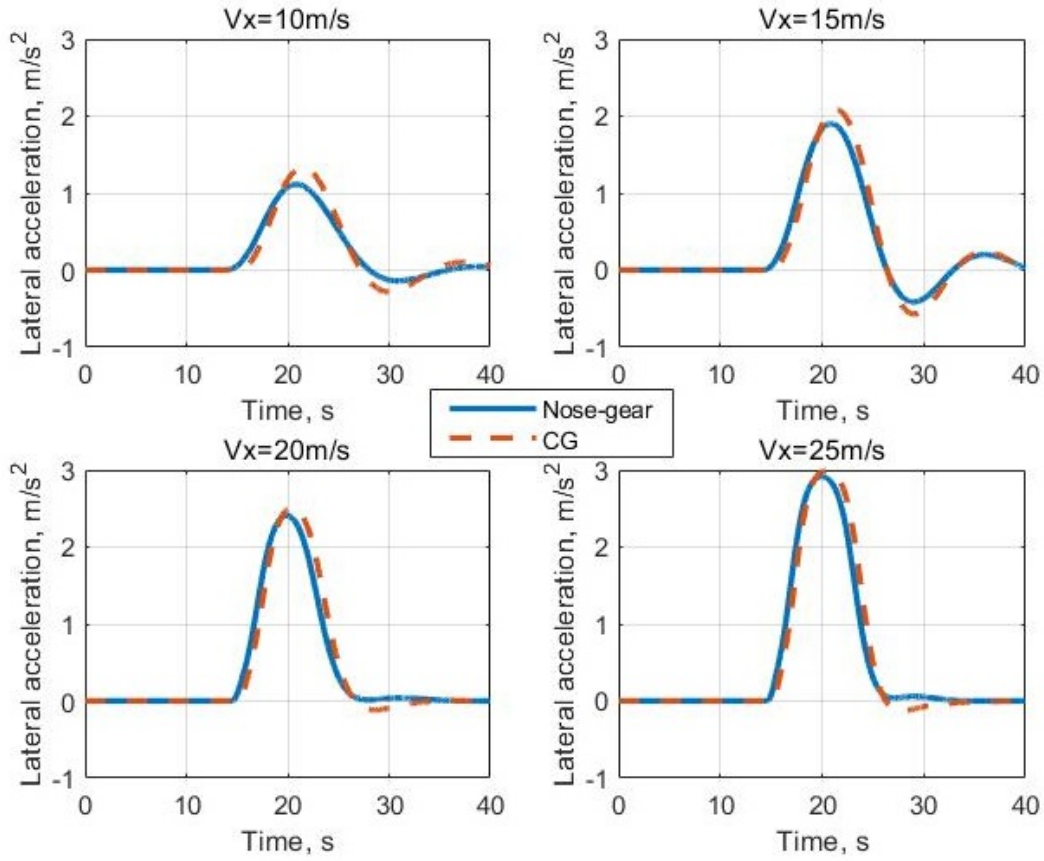


Figure 3.15: Lateral acceleration of path following with nose-gear or CG

controller demands less steering input when keeping the nose-gear on the target path as can be seen from Fig.3.14, particularly at low and medium speed. It will also result in lower lateral acceleration as depicted in Fig.3.15, hence lower tyre wear for the aircraft and better riding comfort for passengers.

## 3.5 Different runway geometries

The number and geometry of runway exits vary from airport to airport and within runways at the same airport. Different runway exits are designed to make operations more efficient on the ground, reducing runway occupancy

time. In this section, two alternative runway exit geometries are compared with CG following the centreline: 30° and 90°. A 30° runway exit is designed for high-speed turnoff with a design speed of 60knots ($30.8m/s$). Compared with the old design of 45° runway exit, this design is favoured in the case that peak operations exceed 30 per hour. In contrast, a 90° runway exit is designed for low volume of traffic, typically located at the ends of a runway. The proposed Expert Pilot Model is tested with these two types of runway exits, and the maximum exit speed is identified in each case.

### 3.5.1 30° runway exit

We use the same criterion for a safe runway exit as in the previous section. Specifically, the maximum lateral deviation allowed is $15m$. Since we are more concerned about high speed runway turn-off in this runway geometry, EPM is

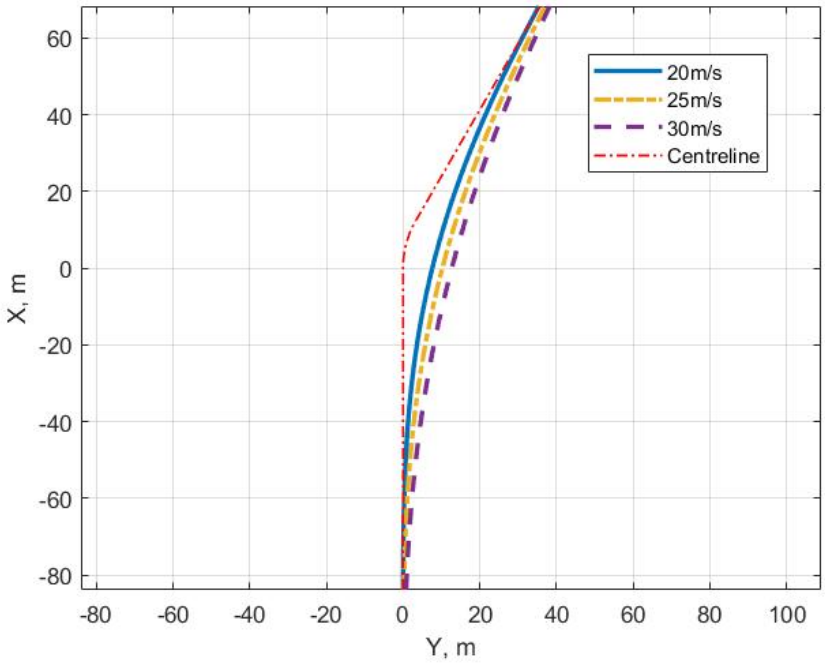


Figure 3.16: Aircraft trajectories for 30° runway exit at high speed.

tested at a range of higher forward speeds from $20m/s$ to $30m/s$. In practice, pilots might not choose to execute a runway exit manoeuvre at this high speed; indeed, they normally exit the runway at a medium speed around $15m/s$. In view of this, the proposed controller would be able to improve the efficiency of aircraft ground operations.

Fig.3.16 shows the aircraft trajectories at three different speeds: $20m/s$, $25m/s$, and $30m/s$. All trajectories are stable and smooth, rolling at a reasonable distance to the centreline; this is consistent with the maximum design speed. The lateral deviations along the trajectories are illustrated in the top panel of Fig.3.17. It can be seen that at any speed within the design speed limit ($30m/s$), EPM is capable of performing a high-speed runway turnoff with lateral errors less than $15m$. According to the Federal Aviation Regulation, the load on the aircraft CG must not exceed $0.5g$ laterally. The aircraft controlled by EPM experiences a peak lateral acceleration lower than $2.5m/s^2$, which complies with the regulation, as shown in the middle panel of Fig.3.17.

With an increased forward speed, the controller is subject to a longer lookahead distance. As a result, the aircraft starts to steer at a further distance before the corner. From the steering inputs shown in the bottom panel of Fig.3.17, we can see that the aircraft starts to steer to the right at 5s before the corner, which could be as far as $150m$ in the case of $30m/s$. This massive amount of lookahead is essential for high-speed runway turnoff despite it not being typically used by pilots. Another advantage of a long preview distance is to effectively reduce overshoot across the centreline, since steering actions are taken in advance to compensate for the delay of the dynamical system.

### 3.5.2 $90^\circ$ runway exit

A $90^\circ$ runway exit is normally located at both ends of a runway. However, it is used only when the aircraft has missed all the exits along the runway. Since pilots have limited visibility due to the blind spot below the cockpit, a $90^\circ$ exit manoeuvre is more challenging for them to operate compared to a $45^\circ$

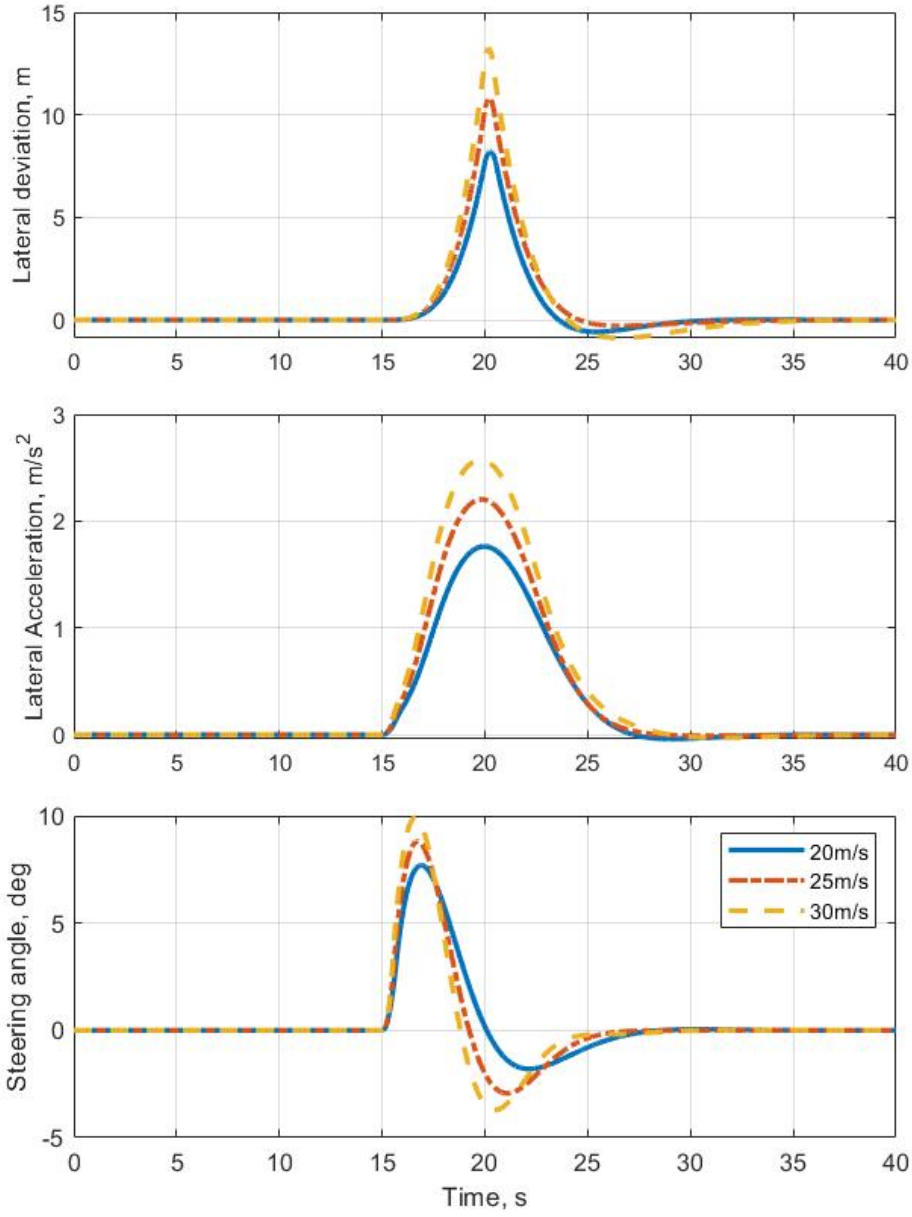


Figure 3.17: Simulation results of 30° high-speed turnoff.

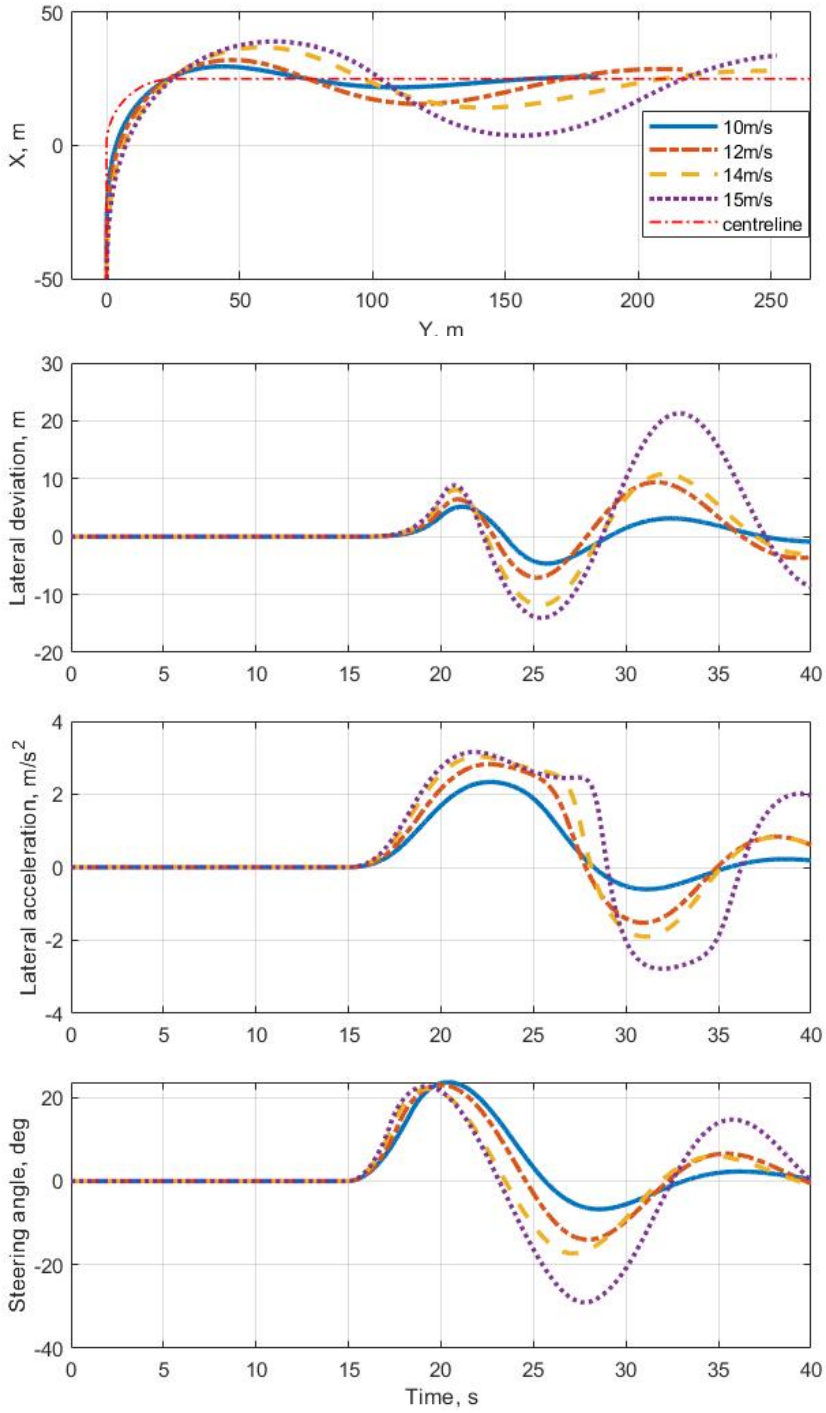


Figure 3.18: Simulation result of 90° runway exit

or 30° exit. Therefore, pilots normally execute a right-angle exit at extremely low speed no higher than $5m/s$, which would significantly increase the runway occupancy time. Hence, a real-time path following controller becomes more desirable in this scenario. Here we aim to identify the maximum speed at which EPM is able to execute a right-angle runway exit. Again, the lateral deviation through and after the corner must not exceed $15m$. The simulation results are shown in Fig.3.18.

EPM is tested at four different forward speeds ranging from $10m/s$ to $15m/s$. At a speed lower than or equal to $14m/s$, the controller is able to keep the lateral deviation below $15m$ despite oscillating around the centreline. At a low speed of $10m/s$, the aircraft closely follows the centreline with lateral deviation no greater than 5m. The aircraft slightly overshot the centreline, and then settled down quickly with no excessive corrections. The peak lateral acceleration is about $0.2g$ which is acceptable according to the regulation. However, it may result in more tyre wear due to the high amount of steering input as can be seen in the bottom panel.

Although people normally leave a safety margin for any ground manoeuvres, it is still worth knowing the controller's behaviour in an extreme case. With an increased forward speed, the aircraft will experience a longer period of oscillation with higher magnitude; when the forward speed is increased to $15m/s$, the controller is no longer able to negotiate the exit manoeuvre within the prescribed constraint on lateral deviation. The aircraft is significantly deviated from the centreline after the corner despite a massive amount of steering angle being applied to correct the track error. Although runway width is different from airport to airport, $10m/s$ would always be a safe forward speed for a 90° runway exit. In comparison with a typical manually operated runway exit at $5m/s$, the proposed controller is able to improve the efficiency of this type of manoeuvre significantly.

## 3.6 Concluding remarks

We present a simple driver model initially developed for ground vehicles, and applications in aircraft ground path following. Motivated by its unsatisfactory path following performance, we improve the driver model by adding an additional feedback control gain with respect to yaw angle. Then the steering control relies on two proportional terms: one is to correct the current steering angle given the predicted lateral deviation at a single preview point; the other one is to damp down the steering input given the current yaw angle. This improvement enables the proposed pilot model to perform more effective and efficient path following.

We provide some guidance for the tuning of controller parameters. The proposed controller can be tuned via a couple of parameters; the optimisation of these parameters is given in detail. A comprehensive simulation study is conducted to examine and analyse the controller's behaviour over a wide range of speed. Comparisons between the original driver model and EPM are made, and improvement of the path following performance is highlighted. Additionally, the difference between using CG and nose-gear as the reference point when following a given path is investigated; following a path via nose-gear results in lower steering input and lateral acceleration despite slightly higher track error. Lastly, the proposed controller is tested and compared in a variety of runway exit geometries including 30°, 45°, and 90° runway exit. The maximum speed for each exit design is identified. In conclusion, the Expert Pilot Model can be successfully used to automatically execute runway exit manoeuvres by following the centreline. It is tuned to achieve the best possible performance that an expert pilot could achieve; it delivers a fast and stable runway turnoff which could reduce runway occupancy time and hence improve airport efficiency.

# Chapter 4

# Generalised Optimal Control

## 4.1 Introduction

To evaluate the optimality of the proposed Expert Pilot Model (EPM), Generalised Optimal Control (GOC) is employed to numerically investigate the optimal solutions of aircraft runway exit manoeuvres. Comparing with existing optimal control toolbox, GOC has better adaptability providing easy access to intermediate variables, e.g. slip angles of each gear. GOC is able to achieve proper convergence despite not being the most state-of-the-art method. Indeed, its optimal solution is a benchmark against which the effectiveness of a controller can be judged.

GOC is an iterative algorithm based on a gradient descent implementation of Pontryagin's Maximum Principle for application in dynamical systems. It is able to establish the optimal sequence of control input for any smoothly nonlinear system by minimising a smooth cost function. It is a particularly attractive approach in this context as it allows simultaneous optimisation of time-varying controls (steering, acceleration and braking) and fixed model parameters. For a specific manoeuvre-cost function combination, GOC minimizes a Hamiltonian function, expressed in terms of system states and co-states. As part of the Hamiltonian function, the cost function is defined with respect to specific

control objectives. Firstly, GOC is used to investigate optimal solutions of aircraft path following with both longitudinal and lateral control optimised simultaneously. This optimisation experiment demonstrates a realistic runway exit manoeuvre using steer, thrust, and brake, despite it not providing a comparison to EPM. Secondly, to make the most of GOC and provide a benchmark for controller design in the future, different control objectives are considered, e.g. minimum runway occupancy time and minimum tyre wear. Finally, EPM is compared with the numerically-optimal solution of steering control; a simple path following manoeuvre at constant forward speed is considered.

## 4.2 Control algorithm

To find the theoretically best solution for a specific ground manoeuvre, a numerical optimization method is introduced here. The Generalized Optimal Control (GOC) algorithm is based on a gradient descent implementation of Pontryagin's Maximum Principle for application in dynamical systems [95, 96]. It minimizes a given cost function $J$ which typically consists of a continuous dynamic cost function $L[x(t), u(t)]$ plus a residual cost $L_T[x(T)]$ associated with final states:

$$J = L_T[x(T)] + \int_0^T L[x(t), u(t)]\, dt \tag{4.1}$$

A vector of co-states, $p(t)$, is introduced and then a Hamiltonian function is defined in terms of the system states and co-states as follows:

$$H = L[x(t), u(t)] + p^T(t) f[x(t), u(t)] \tag{4.2}$$

where $f[x(t), u(t)]$ is the system equations. The co-states are given by:

$$\dot{p^T}(t) = -\frac{\partial H}{\partial x} = -\frac{\partial L}{\partial x} - p^T \frac{\partial f}{\partial x} \tag{4.3}$$

$$p^T(T) = \frac{\partial L_T}{\partial x(T)} \tag{4.4}$$

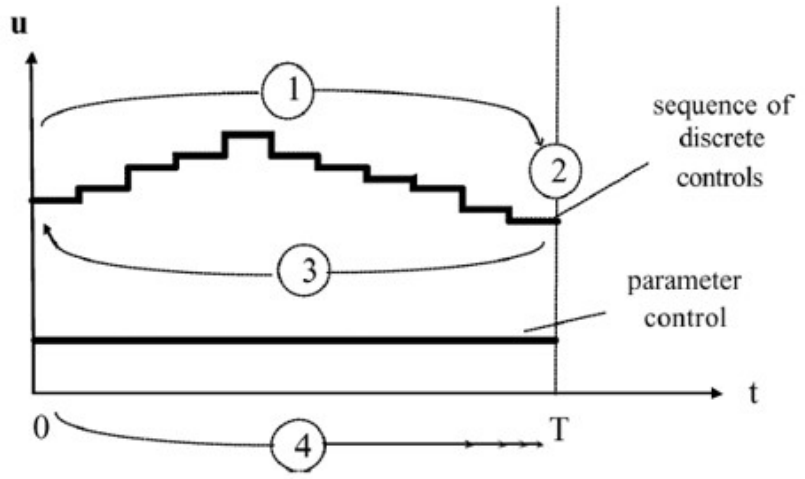


Figure 4.1: 4 Steps of GOC algorithm

The optimal control sequences is found at the minimum of the Hamiltonian function:

$$\frac{\partial H}{\partial u} = 0 \tag{4.5}$$

The optimal solution is identified via a discrete sequence of controls, with each control element held constant for an equal time interval $\Delta t_c$. Within the time period for each control, the cost gradient is obtained directly from the Hamiltonian as:

$$\frac{\partial J}{\partial u_i} = \int_{t_{i-1}}^{t_i} \frac{\partial H}{\partial u_i}\, dt \tag{4.6}$$

A gradient-based iterative optimization can then be utilized to determine the optimal control sequence with the 4 steps outlined in Fig.4.1:

- Step 1: The dynamical system is evaluated (for the current control sequence) from the initial condition $x(0)$. The continuous cost component in Eqn.4.1 is integrated simultaneously.

- Step 2: The final state $x(T)$ is used to evaluate the residual cost $L_T[x(T)]$ and the final co-state $p(T)$ by Eqn.4.4.

- Step 3: The co-state system calculates the integral of the co-states via $\frac{\partial H}{\partial x}$ in reverse-time from the final co-state $p(T)$.

- Step 4: Cost gradients are used to update the control sequence by a line search optimization along the steepest descent direction to minimize the cost function.

Steps 1-4 are repeatedly executed until suitable convergence is achieved. The optimal solution is considered to be converged if the magnitude of cost gradients are sufficiently small and no further reduction of total cost can be achieved with more iterations.

We admit that GOC is not a state-of-the-art optimal control method in light of the popularity of direct methods. However, it is still proposed in this research because it shows good convergence to optimal solutions in all the control problems considered here. It might not be the most efficient algorithm, but it does provide sensible solutions for off-line optimisations where we are not concerned about computing speed. Indeed, it gives us a benchmark against which the effectiveness of future real-time controllers may be judged.

### 4.2.1 GOC implementation test

The implementation of GOC with the aircraft ground dynamics model, as used throughout this thesis, is validated through a test case with straightforward results: a maximum straight-line deceleration case. A 4th-order Runge-Kutta method is used to perform the time integration of the states and co-states, with a constant timestep used throughout the simulation. State errors are monitored in order to set the time step to ensure reasonable accuracy. A zero-order-hold control input is applied for some control timestep $\Delta t_c$, not necessarily the same as the numerical integration timestep. The length of control step ($\Delta t_c$) affects the convergence speed of the optimization, and also the fineness of the control sequence. To achieve a fast and accurate convergence, a coarse resolution is specified initially; this resolution is improved over several

concurrent GOC runs to obtain an appropriate level of continuity in the final control sequence.

In this straight line braking scenario, GOC is used to identify the braking required to minimize the total distance travelled during a simulation. The aircraft starts in an equilibrium condition, with a forward speed of $40m/s$ and heading in the global X direction. The simulation time span (in seconds) is specified as $t \in [0, 10]$, with a numerical time step of 5ms (chosen as it is sufficiently small for this dynamical system). To ensure the aircraft remains in a straight line, the continuous cost function is defined as a track cost $L_{track}$. For this case, it is a quadratic function with respect to the aircraft's deviation from the global X axis:

$$L_{track} = \int_0^T Y^2 dt \tag{4.7}$$

In addition to this continuous cost, a final-state cost is defined as the total distance travelled, i.e. the final distance to the starting point (0,0):

$$L_{final} = X^2 + Y^2 \tag{4.8}$$

The total cost is comprised of the continuous track cost plus the final cost:

$$L_{total} = L_{track} + L_{final} \tag{4.9}$$

The optimal solution obtained by 2200 iterations, is judged to be optimal based on the magnitude of all cost gradients at each point in time. The optimal control sequence, in this case the braking torque, is shown in Fig.4.2. The cost gradients obtained at this optimal iteration are shown in Fig.4.3: they have been reduced to a sufficiently low level; additional iterations beyond this point will not provide significant reductions in total cost. An initial brake spike is used to slow the wheel speed down rapidly at the beginning of this simulation, however the brake torque is then modulated to keep each wheel rolling at its optimum total slip. This spike with huge magnitude is not feasible for the aircraft's brakes; in a more realistic application, control cost in terms of the brake torques should be added so as to avoid the control input going beyond its physical limit.

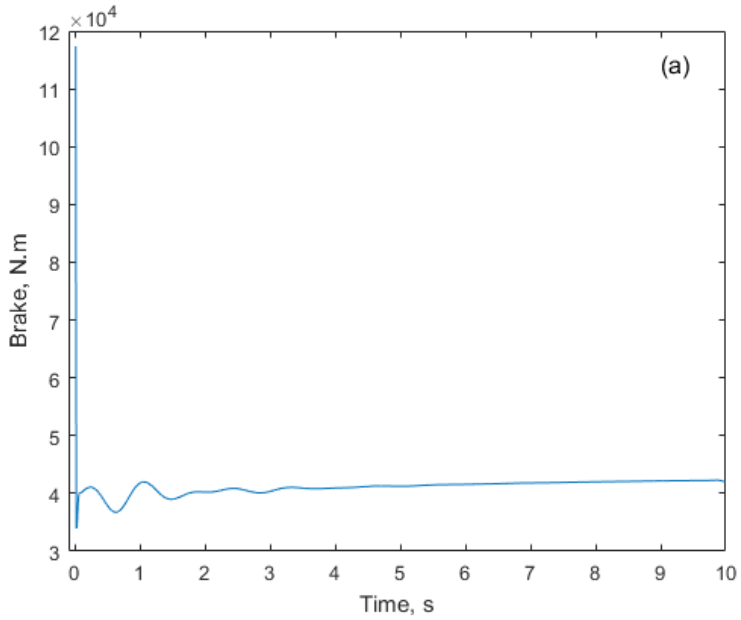


Figure 4.2: Optimal brake torque input.

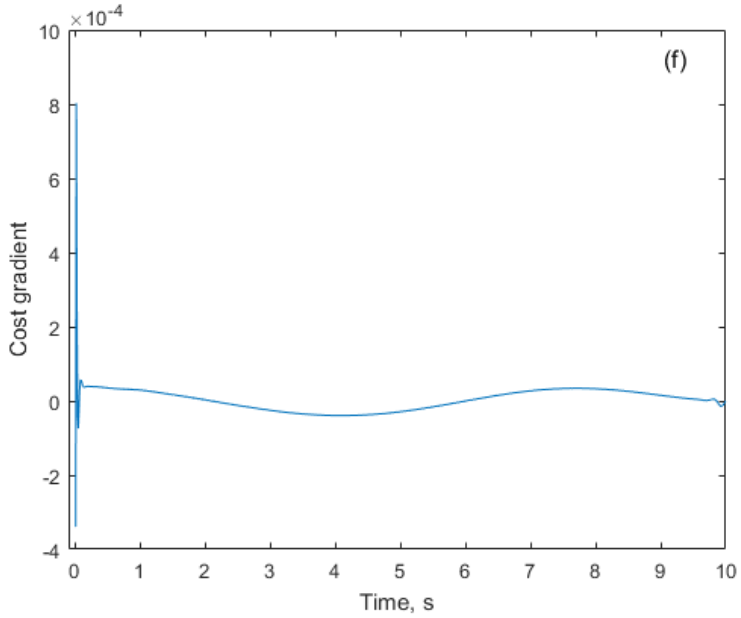


Figure 4.3: Cost gradient with respect to brake.

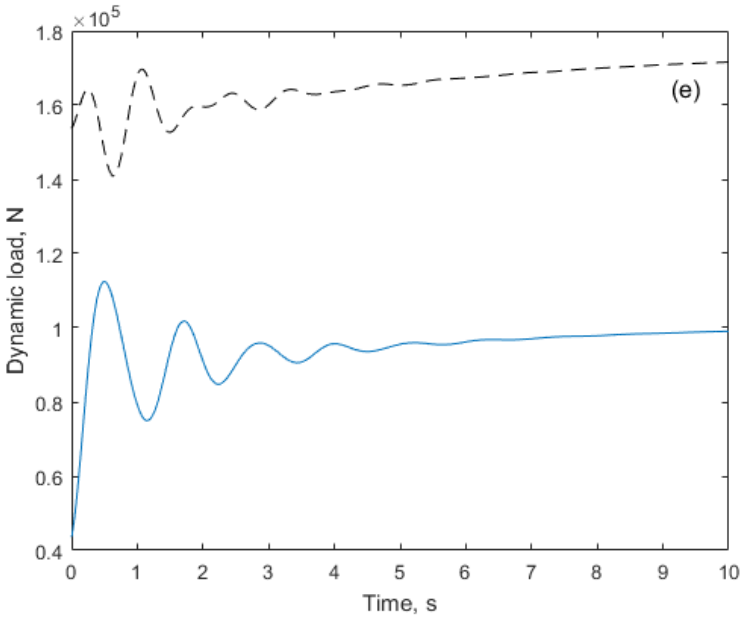


Figure 4.4: Dynamic load on nose-gear(solid) and main-gears(dash).

The oscillations in brake torque that occur during the first 4 seconds are a response to the changing dynamic load on the main landing gears, observable through comparison of Fig.4.2 and Fig.4.4. Since the tyre's peak force is a function of its vertical load, a greater load on the tyre means more brake torque can be applied before it saturates. Fig.4.4 shows how the load on the nose gear and the main gear varies throughout the simulation. Initially, there is a small weight transfer from the main gears to the nose gear due to the initial deceleration. This results in a period of transient behaviour as the longitudinal weight transfer settles to a steady value, with a corresponding reduction in brake torque during this transient period as shown in Fig.4.2. Over the second half of the simulation, the loads on main gear and nose gear increase together, because the aircraft's lift decreases as it slows down. Fig.4.5 shows the main-gears' contact-patch speeds and their translational speeds. The difference between them results in a longitudinal slip ratio. Applying a brake torque causes the wheels' angular velocity to reduce. Since the wheels'

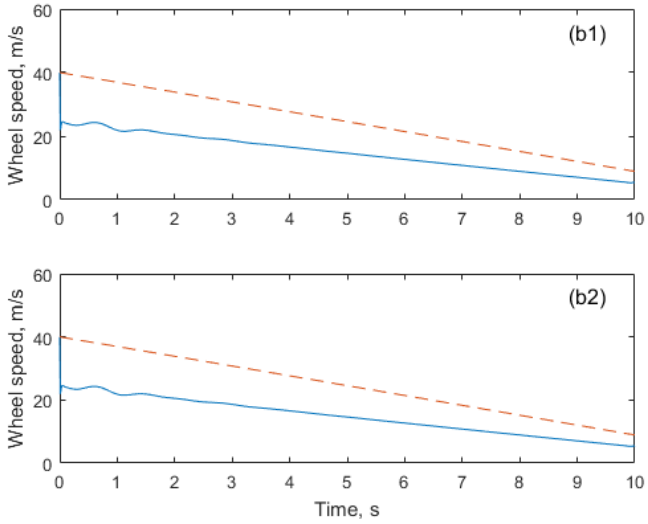


Figure 4.5: Wheel contact-patch speed (solid) and translational speed (dash) for the right and left gear.

contact-patch speed becomes lower than the translational speed, a negative slip ratio occurs. This generates a negative friction force on the main gears, which causes the aircraft to decelerate. The gradient of the dashed curve (the wheels' translational velocity) shows that the aircraft experiences a constant deceleration rate around $3m/s^2$.

Optimality of the results is validated by analysing the tyre behaviours. For pure braking in a straight line, the total slip consists of longitudinal slip ratio only; lateral slip remains zero throughout. The maximum deceleration should therefore occur when the total slip is equal to the optimal slip. If the tyre experiences a slip greater to or less than this value, it will generate less force than its capacity. The slip angles shown in Fig.4.6 suggest that this is the case where optimal braking has been applied to achieve the aircraft's maximum deceleration rate. A very small period of over-slip at the beginning is caused by the initial brake spike (required to remove wheel momentum as fast as possible). Fig.4.7 shows the normalized tyre forces (w.r.t. the maximum force) have been perfectly controlled, as the forces remain at the value of '1'

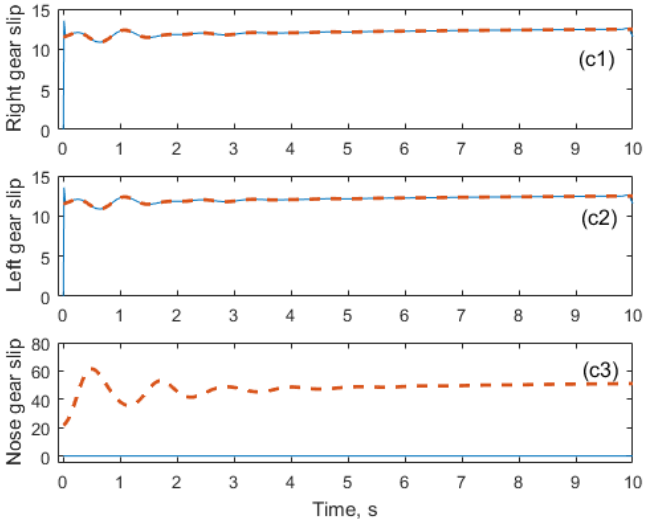


Figure 4.6: Optimal slip(dash) and actual slip(solid) for the right, left, and nose gear.

for both the left and right gears. Note that no braking force is applied to the nose-gear.

This simple test case shows that the implementation of GOC used in this work is able to obtain an optimal sequence for a control input. The wheel speeds are controlled such that they remain just below saturation, in order to achieve the maximum deceleration rate for the aircraft. The next section considers results from GOC for the more complicated case of a high-speed runway exit manoeuvre.

## 4.3 Optimal high-speed runway exit

In this section, GOC is used to find optimal control sequences for high-speed runway exit manoeuvres. Since GOC is capable of optimising all the control inputs at the same time, the aircraft is not necessarily rolling at a constant forward speed. The initial forward speed is set as $40m/s$ where the optimal strategy of steering and deceleration can be revealed. Three realistic test cases

are considered here, each using the same runway geometry and track cost: in case A, the optimal control sequence minimises the distance between the aircraft's CG and the runway centreline; in case B, it maximises the distance travelled by the aircraft during the 20 seconds of simulation; in case C, the optimal control sequence minimises tyre wear. The track cost is defined as a quadratic function of the distance to the runway's centreline as shown in Fig.4.8. Constraints on states and control inputs can be imposed via "tanh" function or higher order polynomial when needed. Such constraint should not be solely used as the track cost because the aircraft may try to cut the corner, which is dangerous in practice.

### 4.3.1 Case A: follow the centreline

Runway exit by following the centreline is a common ground manoeuvre which is manually operated by a pilot. When executing such a manoeuvre, pilots generally focus on the steering, leaving the brakes to null and thrust to idle.

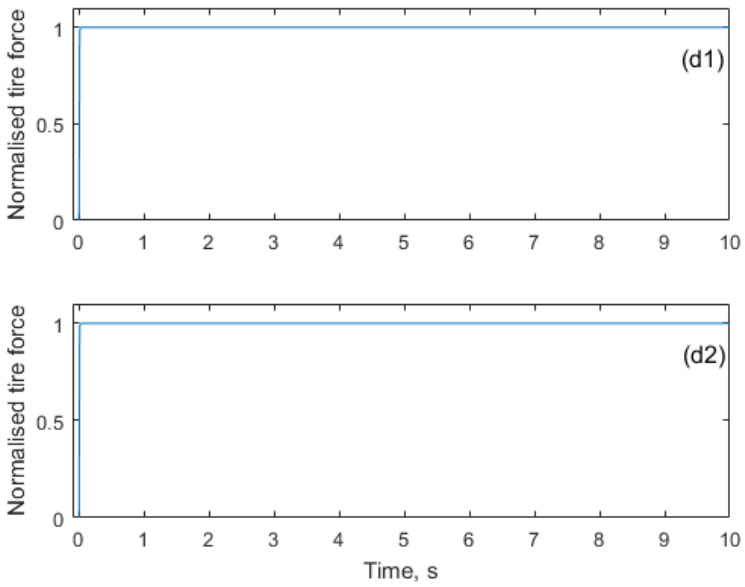


Figure 4.7: Normalised friction force for the right and left gear.

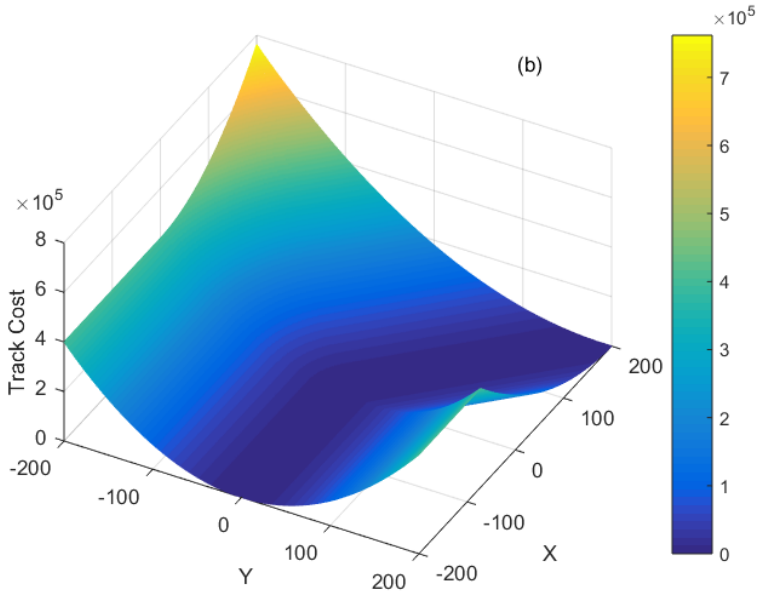


Figure 4.8: The track cost as a function of ground position.

To investigate the best combination of steering, thrust and brake, GOC is used to minimize the distance between the aircraft CG and the runway centreline. The initial condition is an equilibrium state with a forward speed of $40m/s$. The continuous cost function contains only the track cost as depicted in Fig.4.8. The residual cost is a function of the aircraft's yaw angle, yaw rate and lateral velocity, and is used to ensure that the aircraft finishes the simulation aligned with the road with no significant yaw rate or side-slip velocity. Hence, the overall cost function is defined as follows with coefficients $\lambda$ to balance cost components; to improve convergence of the optimal solution, the $\lambda$ coefficients are set based on the residual cost and then rescaled to ensure that all the cost components are in the same order of magnitude:

$$L_{final} = \lambda_1(\psi(T) - \pi/4)^2 + \lambda_2 W_z(T)^2 + \lambda_3 V_y(T)^2 \tag{4.10}$$

$$L_{total} = L_{track} + L_{final} \tag{4.11}$$

Fig.4.9 shows the total cost variation along the 50000 iterations. It drops

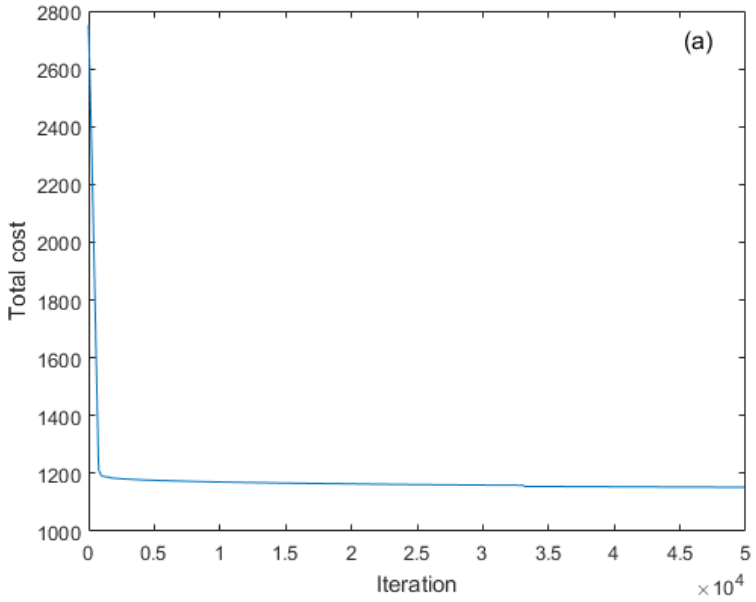


Figure 4.9: The total cost for 50,000 iterations.

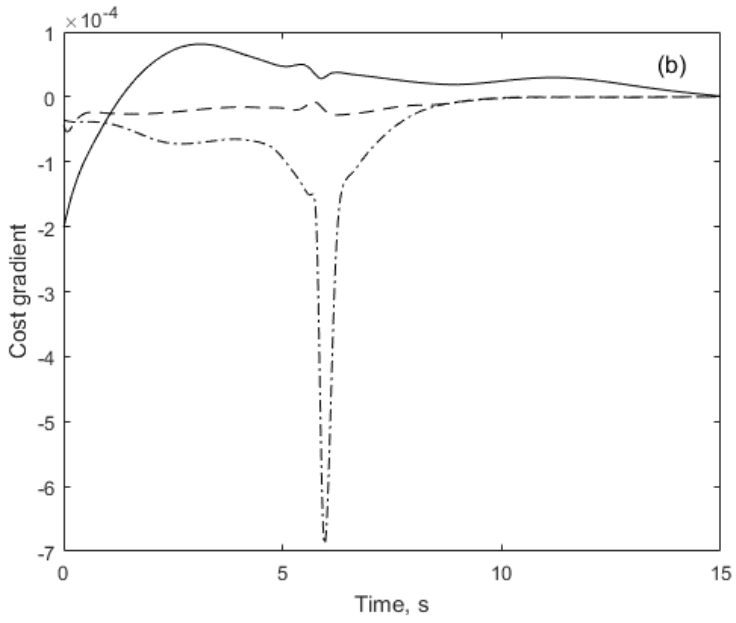


Figure 4.10: The final cost gradient in terms of steer(solid), thrust(dash), and brake(dashdot).

dramatically within the first 1000 iterations and then settles down gradually over the next 49000 iterations. Since the magnitude of the cost gradients has been reduced to the order of $10^{-4}$ as shown in Fig.4.10, and no significant reduction of total cost can be achieved with further iterations, the cost function is judged to have converged. Although the spike on the cost gradient would shrink with further iterations, it is sufficiently small (of the order $10^{-4}$) to be considered as converged.

The aircraft's optimal trajectory is illustrated in Fig.4.11, with small triangles used to represent the aircraft's position and orientation with an interval of $1s$. It can be seen that the aircraft stays close to the centreline throughout the simulation, despite it not following it exactly. The aircraft initially steers to the left when approaching the right-hand exit, in order to maximize the

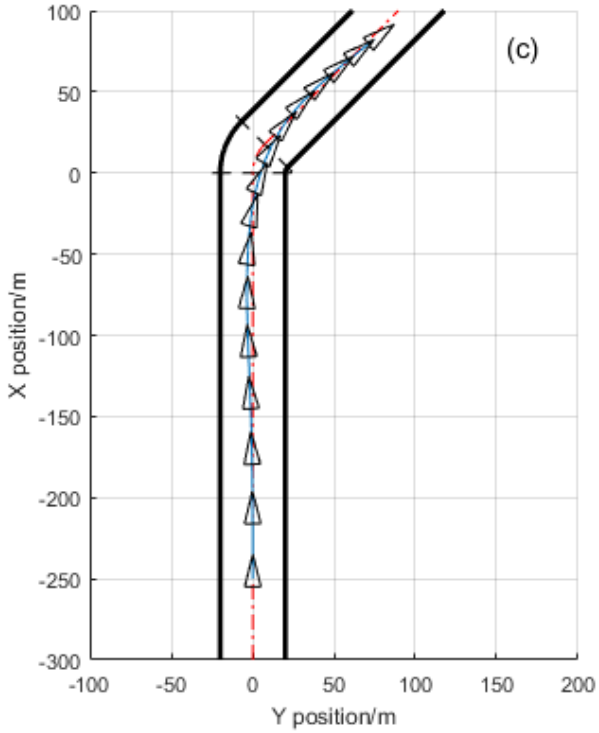


Figure 4.11: The optimal trajectory of the aircraft CG.

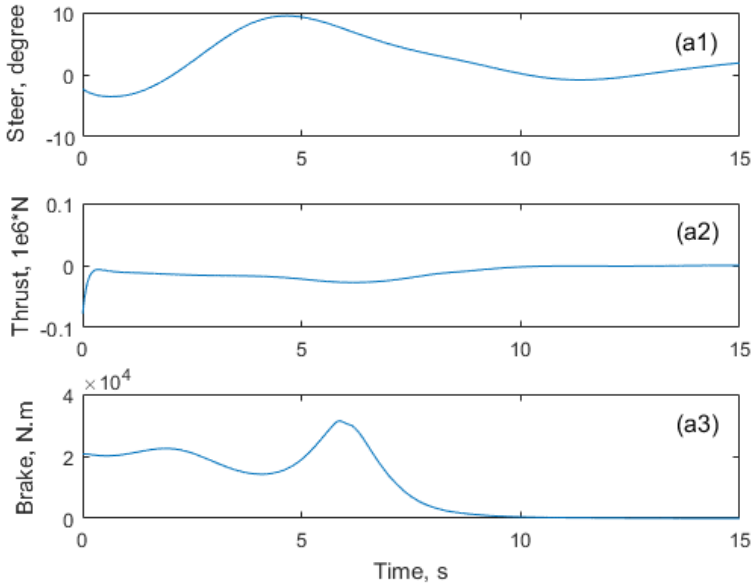


Figure 4.12: The optimal control inputs for steering, thrust and braking.

turning radius without deviating from the path centreline too much in the corner (and hence incurring a high cost). Fig.4.12. shows the optimal control inputs for steering, thrust and braking.

The negative steering input at the beginning of the simulation turns the aircraft to the left, however the aircraft's large yaw inertia makes it continue to move straight along the runway centreline for the first 3 seconds of the simulation. During the first few seconds, the brakes are applied (along with some reverse thrust) to reduce the aircraft's speed, as the initial forward speed of $40m/s$ is too fast to make a 45° turn. Fig.4.13 shows the wheel's contact-patch speed and translational speed of the right and left gear, highlighting that all wheels' translational speed drops dramatically from $40m/s$ to less than $20m/s$ over the first 6 seconds.

It can be seen that the right (inner) gear's wheel speed drops towards zero during peak braking, and that the brake torque is released to a lower level before this gear's wheel locks. By doing this, the aircraft's dynamics are still

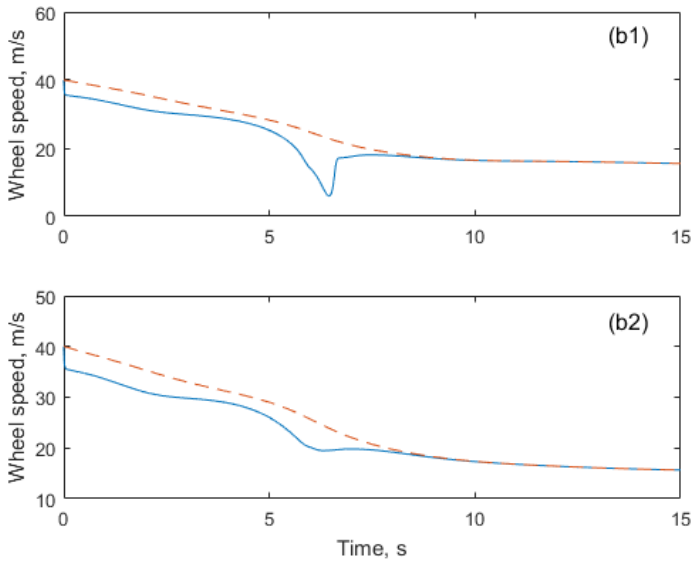


Figure 4.13: Wheel contact-patch speed (solid) and translational speed (dash) of the right and left gear.

under control and the tyres can be recovered from the saturation.

After $5s$, a rapid increase in braking torque causes the right gear's tyre to saturate, as shown by the plot of tyre slip angles in Fig.4.14. An over-slip occurs on the right gear, where the total slip exceeds the optimal slip and the tyre is said to be saturated. This tyre saturation leads to the decrease of the right gear's lateral friction force as shown in Fig.4.15, which in turn increases the total yaw moment around the z axis, allowing the aircraft to make the turn more easily. Optimality of this part of the solution is reflected in Fig.4.16, which shows the normalized total friction force on the main gears (normalized with respect to the maximum force that the tyre can generate). It can be seen that the normalized force on the right gear stays right at the maximum level during the turn except when it over-slips to make a quick adjustment to the yaw angle.

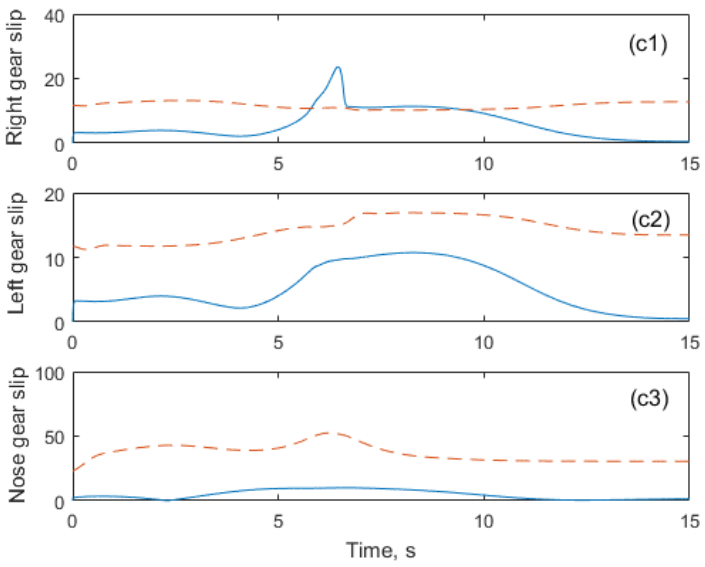


Figure 4.14: The optimal slip (dash) and the actual slip (solid) of the right, left, and nose gear.

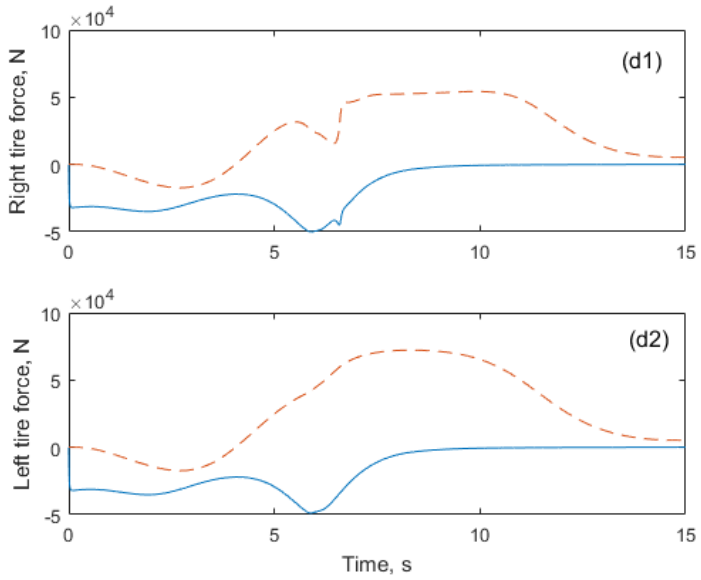


Figure 4.15: The longitudinal (solid) and lateral (dash) force element of the total tyre/ground friction force of the right and left gear.

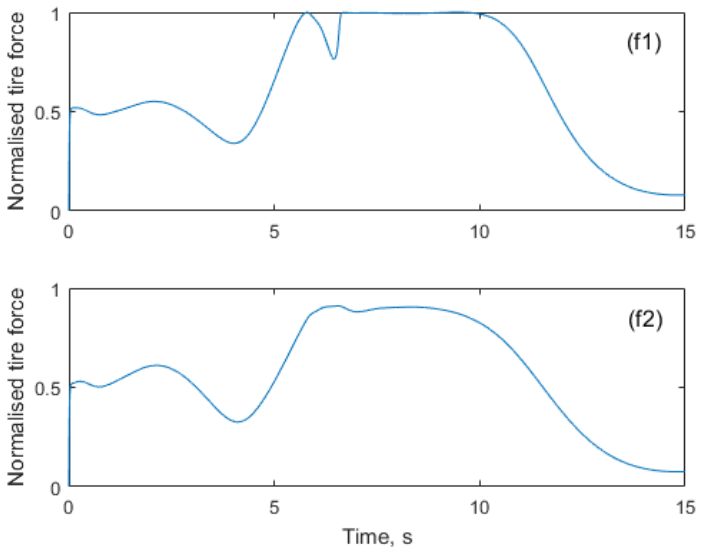


Figure 4.16: The normalized total tyre/ground friction force of the right and left gear.

### 4.3.2 Case B: Minimum runway occupancy time

Aiming to improve efficiency of airport ground operations, the time-optimal solution of runway exit is investigated here. This second case extends the first case by requiring that high-speed runway exit be performed as fast as possible, using steer and brake inputs (thrusts are set to idle in this case). The simulation starts from the same initial condition and runs for the same period of time as in Case A. The continuous cost function contains only the same track cost, however the final cost has been changed: an additional final cost is now defined with respect to the aircraft's final distance to a target point; this ensures that the control strategy maximizes the distance travelled during the simulation and hence minimises the runway occupancy time. The final cost function used for this case is:

$$L_{final} = \lambda_1(\psi(T)-\pi/4)^2+\lambda_2 W_z(T)^2+\lambda_3 V_y(T)^2+\lambda_4((X(T)-500)^2+(Y(T)-500)^2) \tag{4.12}$$

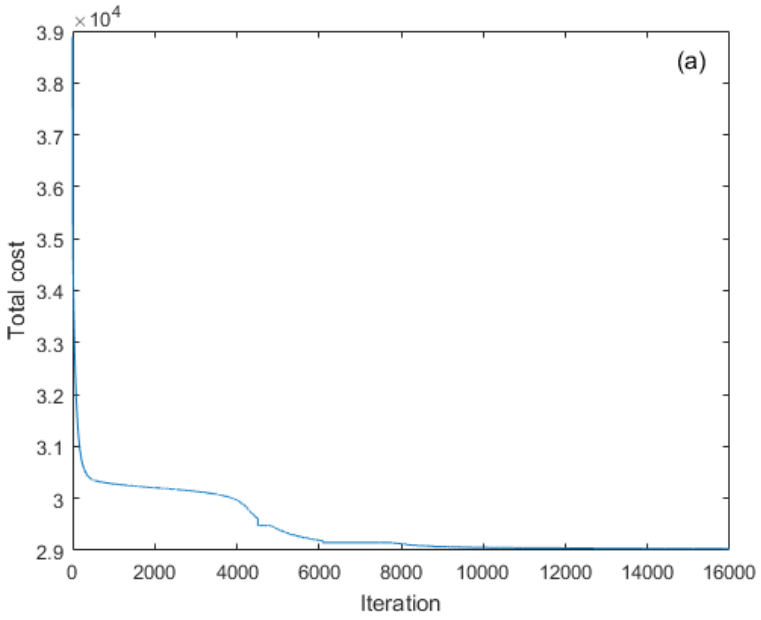


Figure 4.17: The total cost for 16,000 iterations.

The coefficients $\lambda_1$, $\lambda_2$, $\lambda_3$ remain the same as in Case A, whilst $\lambda_4$ is tuned to ensure that the cost component used to maximize the distance travelled contributes approximately the same order of magnitude to the final cost as all the others.

The total cost history shown in Fig.4.17 is judged to have converged after 16,000 iterations. The cost drops significantly in the first few hundred iterations, and then continues to drop gradually over the subsequent 9000 iterations. The magnitude of the final cost gradients, as shown in Fig.4.18, are in the order of $10^{-5}$, so further reductions in total cost won't be achieved with additional iterations. The aircraft's final trajectory is illustrated in Fig.4.19, again with each small triangle showing the aircraft's position and orientation at each second of the simulation.

The optimal steering and braking control sequences are shown in Fig.4.20. As in the first case, the aircraft initially steers to the left to obtain a larger turning radius, and then to the right to negotiate the corner. It also takes a

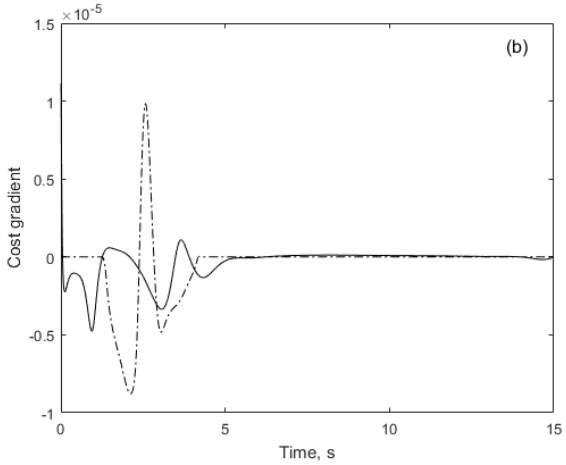


Figure 4.18: The final cost gradient in terms of steer (solid) and brake (dash-dot).

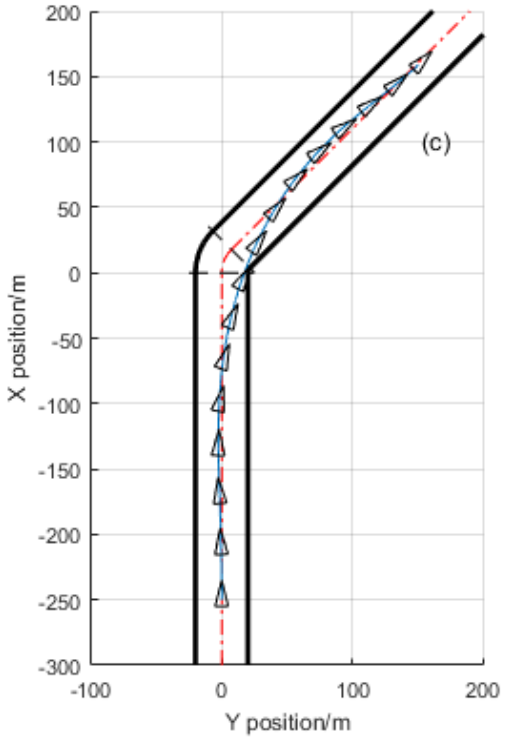


Figure 4.19: The optimal trajectory of the aircraft CG.

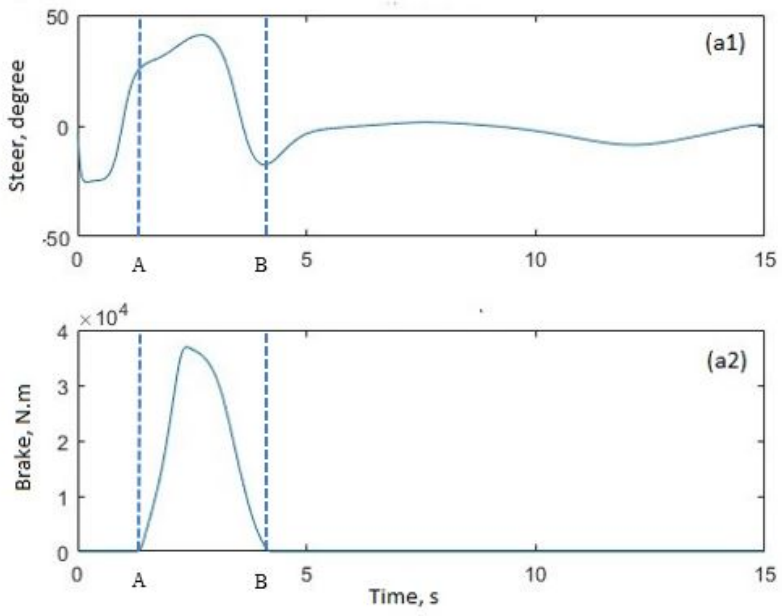


Figure 4.20: The optimal control input of steering and braking.

couple of seconds for the steer input to build up the aircraft's yaw angle due to the aircraft's large yaw moment of inertia. Unlike the initial case where the aircraft just aims to follow the centreline, the right turn cuts more of the corner: this is a familiar tactic used by racing car drivers, as it increases the radius of the turn and hence increases the maximum speed that can be achieved by a given vehicle in the corner. The brakes are also used differently here from the first case: no brakes are applied until the aircraft is at point A (Fig.4.20); the aircraft brakes from point A to point B, whilst it is still steering hard right (in anticipation of the corner); the brake is completely cut off at point B to achieve the maximum lateral slip angle, just as the aircraft starts to move to the right of the centreline, cutting the corner. The combined use of braking and steering between points A and B is an aircraft-specific tactic, as unlike racing cars, aircraft have huge yaw moment inertia. Since the main-gear's slip angle takes time to build up when a steering angle is actuated by the nose-gear, the action of steering doesn't immediately affect its capacity to brake by

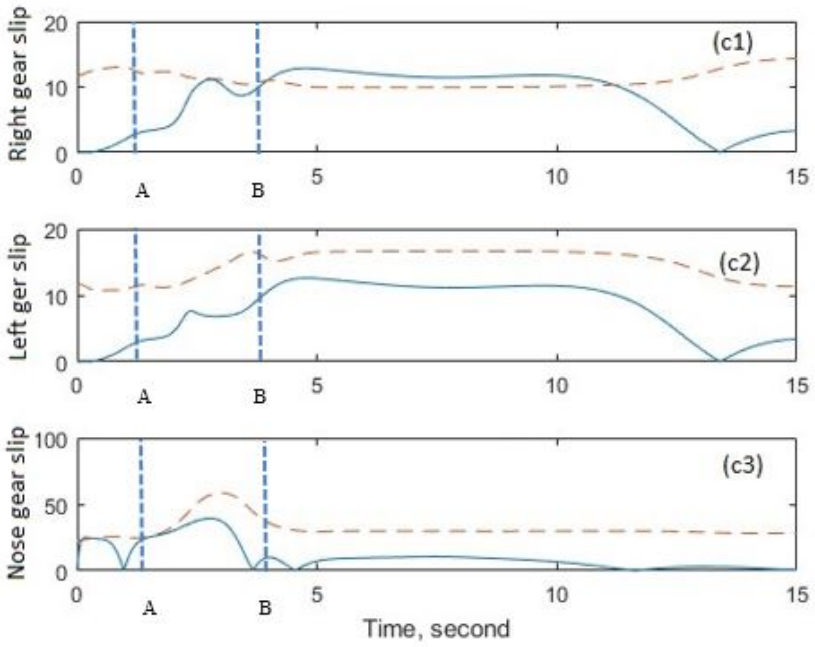


Figure 4.21: The optimal slip (dash) and the actual slip (solid) of the nose, right and left gear.

increasing the total slip experienced. In fact, Fig.4.21 shows that the action of braking increases the nose wheel's optimal slip: the solid curve illustrates the total slip and the dashed curve illustrates the optimal slip where the maximum force occurs. The GOC algorithm balances steer and brake inputs so that the total slip on all the three gears achieves their optimal slip value at some point during the manoeuvre, meaning maximum tyre forces can be generated. This is shown in Fig.4.22, where the normalized tyre force reaches a value of 1 to indicate that the tyre is operating at its maximum capacity. The weight transfer from right gear to left gear, as depicted in Fig.4.23, means that the right gear is allowed to saturate slightly during the right turn, so that the left gear can generate more lateral force (hence maximizing the total lateral force).

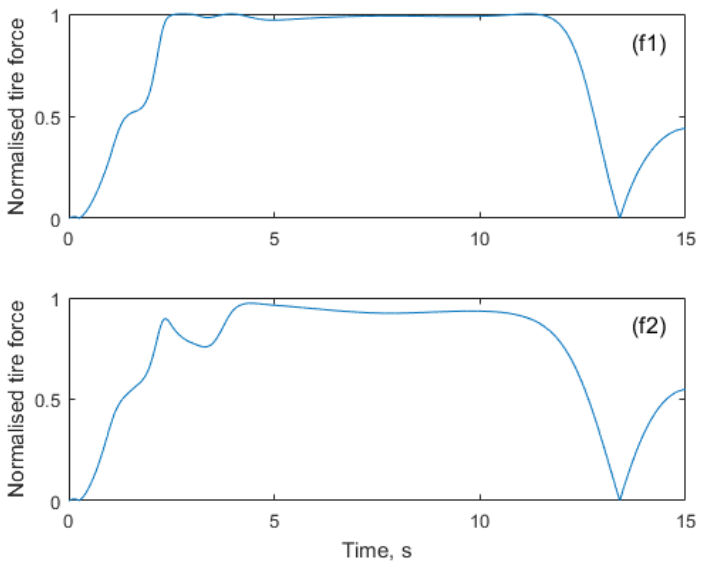


Figure 4.22: The normalized total tyre/ground friction force of the right and left gear.

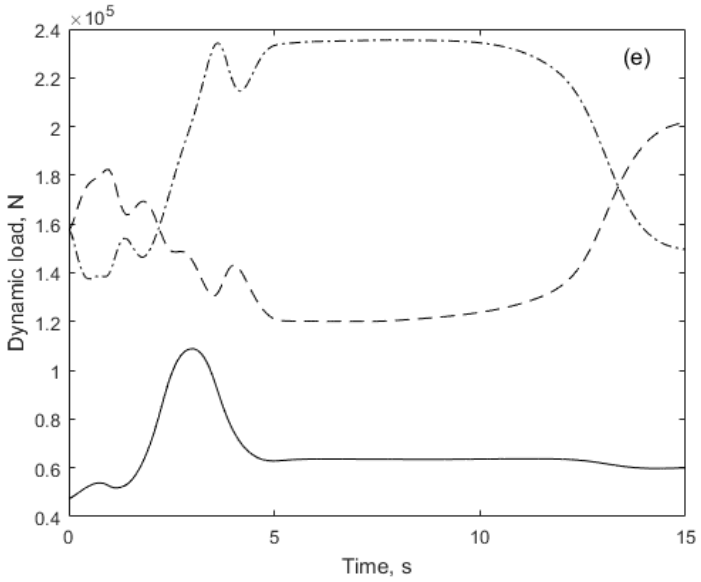


Figure 4.23: The dynamic load on the nose (solid), right (dash) and left (dash-dot) gear.

### 4.3.3 Case C: Minimum tyre wear

From an economic perspective, airlines are eager to extend lifespan of tyres, saving manpower and material resources. The final case considers minimization of tyre wear. Friction is regarded as a fundamental energy dissipative mechanism as a result of which tread surface degradation and wear occur. Hence, as an additional continuous cost component, tyre wear is assumed to be proportional to the friction work performed by the tyre [97, 98]. The tyre wear cost function is given by:

$$L_{tyre} = \int_0^T (|F_{xN,R,L} V_{xN,R,L}| + |F_{yN,R,L} V_{yN,R,L}|) dt \tag{4.13}$$

The absolute value sign will not affect the differentiability of the cost function because the friction forces are always in the opposite direction of the tyres' velocities. Adding this cost component to the cost function considered in Case B, the total cost in Case C is given by:

$$L_{total} = L_{track} + L_{tyre} + \lambda_1(\psi - \pi/4)^2 + \lambda_2 W_z^2 + \lambda_3 V_y^2 \tag{4.14}$$

The simulation starts from the same equilibrium as used in the first two cases. The cost function converged after around 5000 iterations, as shown in Fig.4.24. The cost gradients of steer and brake are both of the order $10^{-7}$, as shown in Fig.4.25, which indicates that the minimum of the cost function has been achieved. The corresponding optimal trajectory of the aircraft's CG is depicted in Fig.4.26, with small triangles illustrating the position and orientation of the aircraft at an interval of 1 sec. The aircraft CG is still within the prescribed safety boundary although it is extremely close to the apex. It cuts the corner to follow the largest turning circle.

The optimal control input of the steer and brake are shown in Fig.4.27. Compared with the solution in Case B, much less steering and braking is applied so as to achieve a lower tyre wear cost. The aircraft performs a similar runway exit manoeuvre by cutting the corner but with a different control strategy. It starts to brake from the very beginning of the manoeuvre to

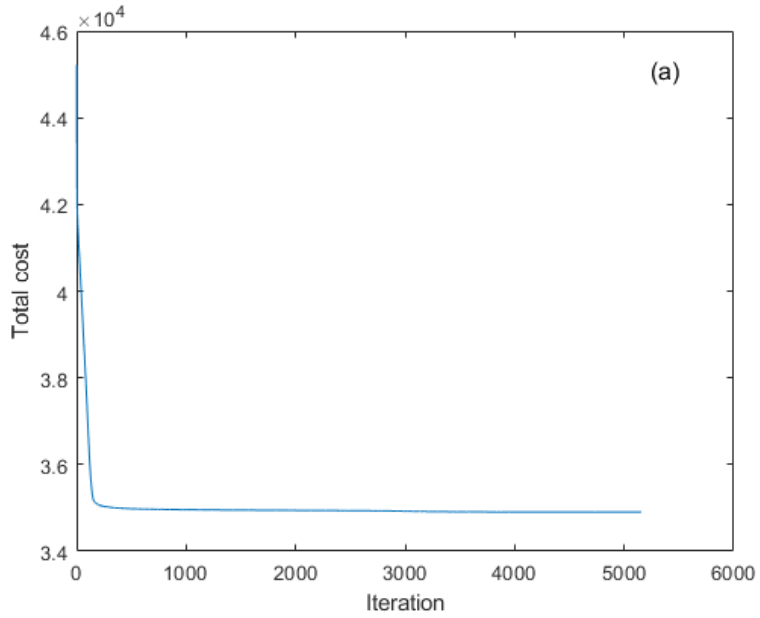


Figure 4.24: The total cost along with iterations.

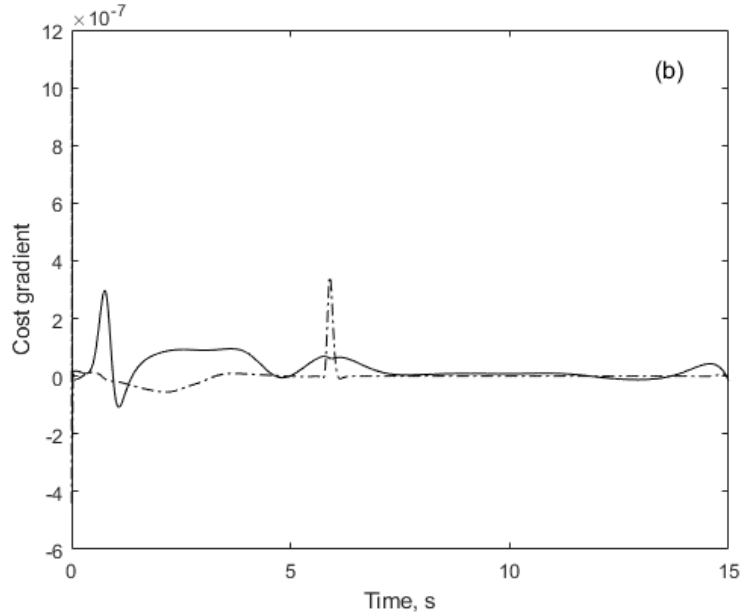


Figure 4.25: The final cost gradient in terms of steer, thrust and brake.

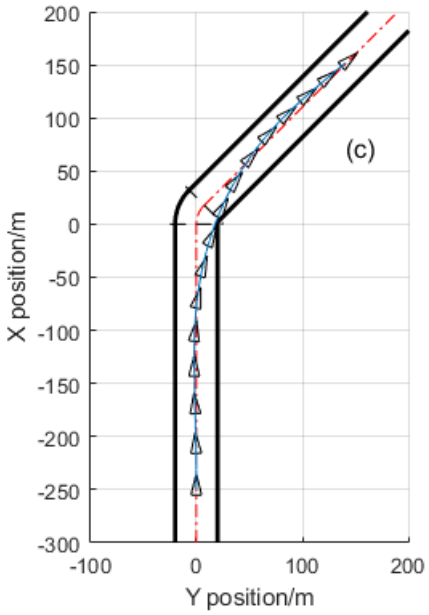


Figure 4.26: The optimal trajectory of the aircraft CG.

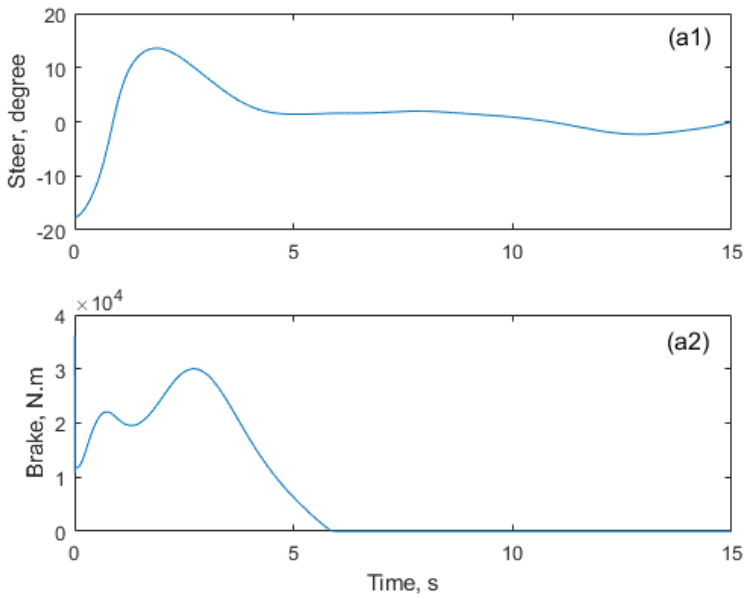


Figure 4.27: The optimal control input of the steer and brake.

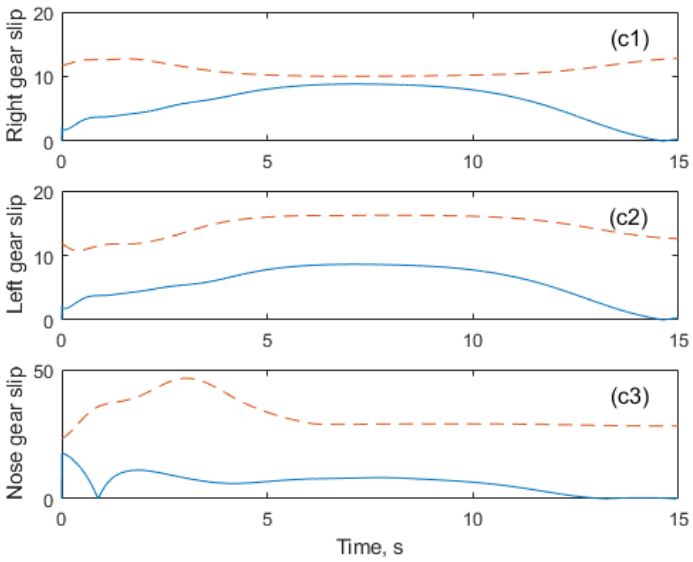


Figure 4.28: The optimal slip (dash) and the actual slip (solid) of the nose, right and left gear.

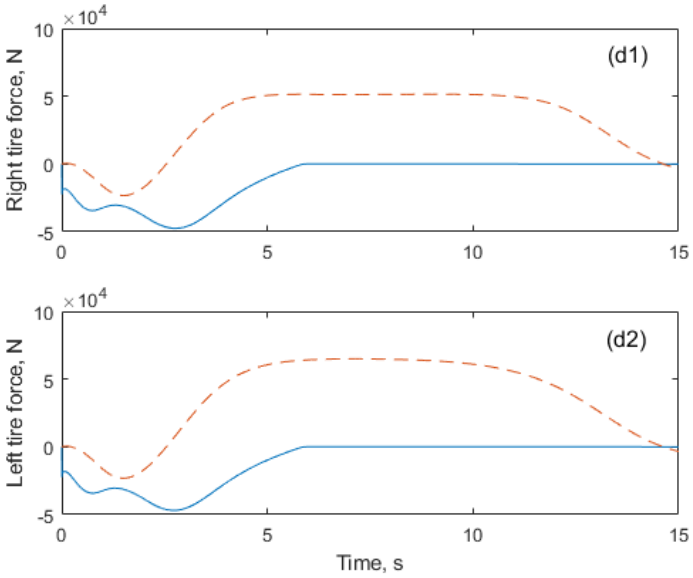


Figure 4.29: The longitudinal (solid) and lateral (dash) force element of the total tyre/ground friction force of the right and left gear.

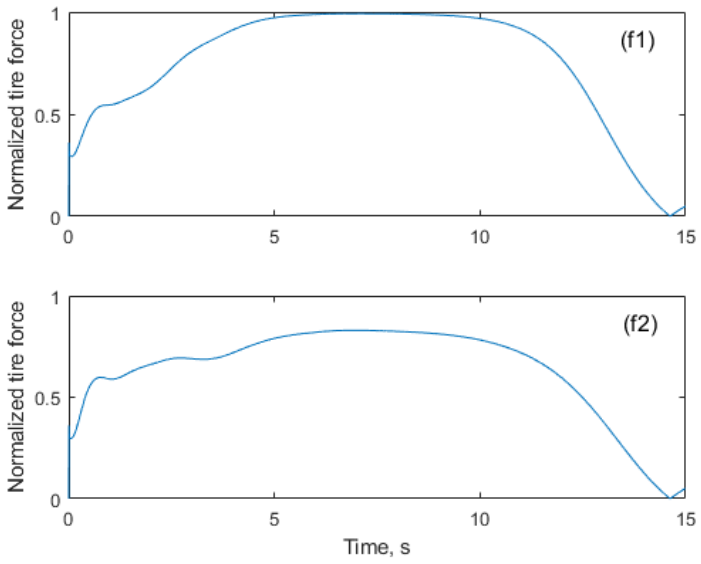


Figure 4.30: The normalized total tyre/ground friction force of the right and left gear.

decelerate. In this way, the aircraft rolls at a lower speed during the corner. Considering the lateral friction force is the main contributor to tyre wear in a runway exit manoeuvre, deceleration before the corner is able to reduce the tyre wear cost. Since GOC is minimizing the runway occupancy time and tyre wear simultaneously, the aircraft doesn't decelerate at the maximum rate.

The tyre wear is also reflected in the tyre slip. Both side slip and longitudinal slip contribute to the tyre wear. In Fig.4.28, the solid curve illustrates the total slip and the dashed curve illustrates the optimal slip where the maximum force occurs: the actual slip of all three gears is kept at a lower level throughout the manoeuvre and no over-slip occurs on any tyre. The lateral and longitudinal forces of the right and left tyres are shown in Fig.4.29; it can be seen that both force components are kept at a lower level. The corresponding normalized friction forces of the main gears in Fig.4.30 show more clearly that the tyres are not working at their maximum capacity. Indeed, the left tyre is far from its saturation point.

## 4.4 Optimality of EPM

The Expert Pilot Model has been proved to be an effective controller for aircraft ground manoeuvres. However, its effectiveness has not been quantitatively studied yet. Since this research aims to develop an optimal controller, results from GOC can be used to evaluate the optimality of the proposed controller. As a numerical optimal controller, GOC is used to provide a benchmark to judge the effectiveness of EPM. The gap between the optimal solution and EPM determines whether a more intelligent controller could provide significant performance advantages.

Starting from the control sequence given by EPM at $20m/s$ for a $45°$ runway exit, GOC is used to further optimize the solution. The track cost is defined exactly the same as in the previous chapter. GOC is able to iteratively decrease the cost function to achieve the optimal solution. The total cost is plotted against the number of iterations in Fig.4.31. It can be seen that the total cost

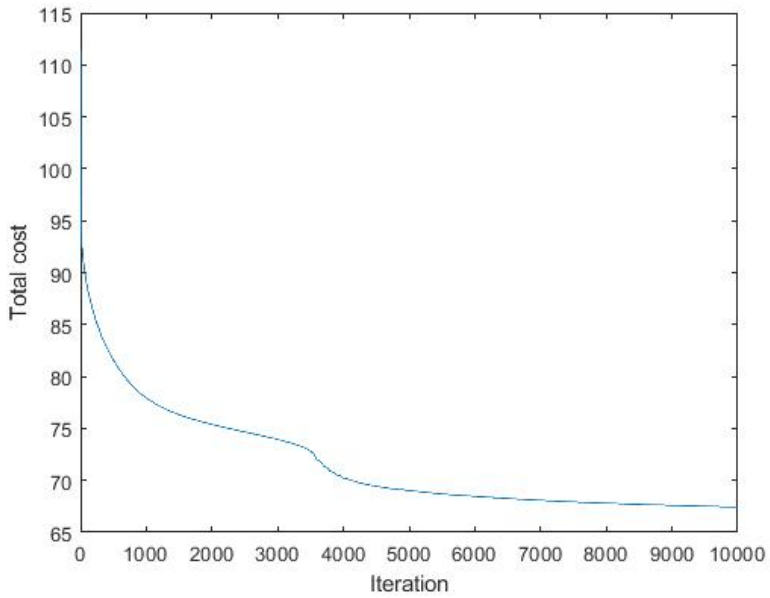


Figure 4.31: Total cost of GOC algorithm against number of iterations.

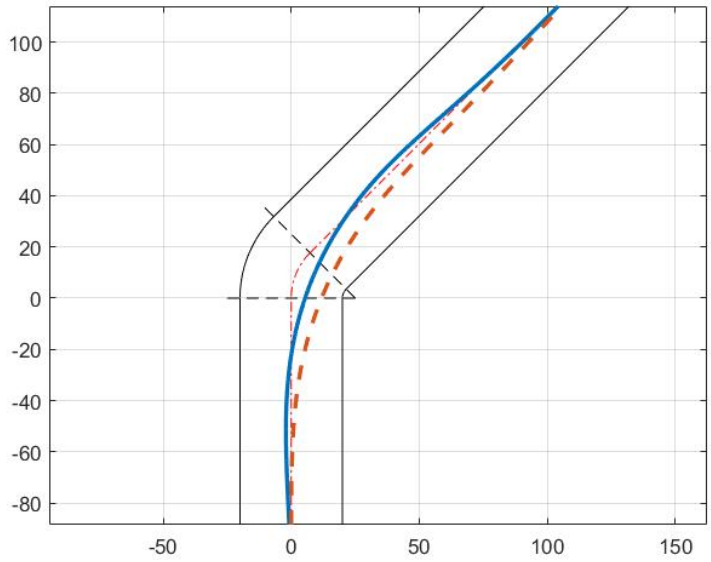


Figure 4.32: CG trajectories of GOC(solid) and EPM(dash).

drops dramatically for the first 1000 iterations; after 5000 iterations, the cost is reduced by nearly half; for another 5000 iterations the cost gradually settles down to a certain level. Considering the magnitude of cost gradient has been reduced to a sufficiently low level which meets the convergence criteria, it is believed that the cost function has converged to the minimum.

The comparison between the aircraft trajectories of GOC and EPM is illustrated in Fig.4.32; the blue solid line is GOC and the red dashed line is EPM. Obviously, the optimal trajectory given by GOC stays closer to the centreline compared to EPM. In terms of the control strategy, EPM is substantially different to the optimal solution. While GOC oscillates around the centreline to benefit from an enlarged turning radius, EPM doesn't traverse across the centreline; instead, it cuts the corner and then slowly correct the lateral deviation. Additionally, the optimal control sequence starts to steer the aircraft much earlier at $t = 7s$ as shown in the bottom panel of Fig.4.33; it takes an oscillatory steering action to achieve a larger turning radius so as to

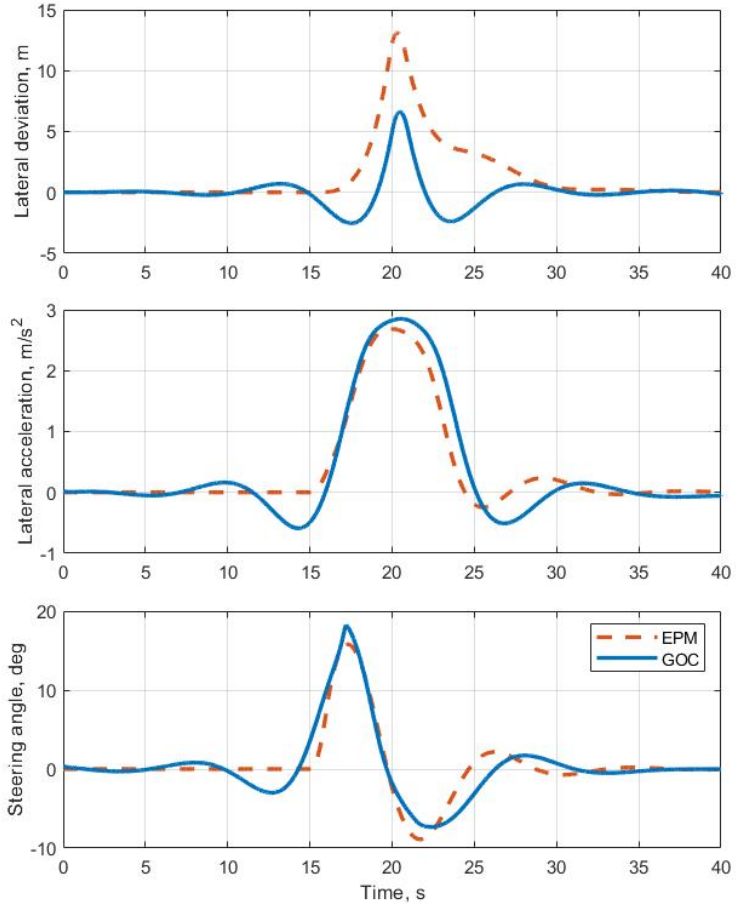


Figure 4.33: Comparison between EPM and the optimal solution given by GOC.

follow the centreline more closely. On the other side, EPM starts to steer later at $t = 15s$ due to its 5s of preview time. Consequently, the aircraft deviates more from the centreline during the corner and requires more steering input to correct the lateral error. The lateral deviation along the trajectory is shown in the top panel of Fig.4.33. As a result of the difference in steering strategy, the maximum lateral deviation of EPM is around two times as high as that of GOC. From the safety point of view, EPM is at a distinct disadvantage due to traversing too close to the apex. Based on the same control cost, EPM ends up with a 4 times higher track cost (263.1) compared to GOC (66.4). Both

controllers have a similar level of lateral acceleration despite GOC having a slightly higher lateral acceleration of 0.3g as shown in the middle panel of Fig.4.33. In conclusion, the difference between EPM and the optimal control is significant, which may indicate that there would be plenty of room for improvement. Motivated by this fact, we develop a near-optimal controller which is presented in the next chapter.

## 4.5 Concluding remarks

This chapter presents a method of optimal control, i.e. Generalized Optimal Control, to study optimal control strategies for an aircraft high-speed runway exit manoeuvres. The ability of GOC to identify the optimal control sequence is validated in the case of a straight line maximum deceleration. Optimality is achieved since the longitudinal slip of both main landing gears is equal to the optimal slip throughout the simulation. Three scenarios are investigated for the high-speed runway exit manoeuvre. In the case where the aircraft follows the centreline, the cost function is comprised of the track cost and final attitude cost. The maximum tyre/ground force is achieved on the inner gear. To investigate the time-optimal solution for the fast runway exit manoeuvre, an additional cost component in terms of the final distance to a target point is employed. Consequently, the aircraft executes the runway exit by cutting the corner at high speed. The tyre/ground forces on the main gears are both close to their maximum level. Finally, the optimal control sequence in the case of minimum tyre wear is identified, where an additional cost associated with tyre wear is added to the cost function. The result shows that the tyre/ground forces for all the gears are kept at a lower level by using less steering and braking.

Since GOC is an iterative algorithm and requires calculations in reverse time, it is suitable for off-line investigation rather than real-time implementation. The optimal solution given by GOC can be used as a benchmark for real-time controller design. Hence, the optimality of the proposed Expert Pi-

lot Model is judged via the comparison with GOC. Based on the same control cost, EPM ends up with a much higher track cost. Additionally, its control strategy is substantially different to the optimal control. Although EPM is proved to be an effective and efficient path following controller, an optimal real-time controller is still desired.

# Chapter 5

# Predictive Steering Control

## 5.1 Introduction

A clear need for a formal solution of real-time optimal steering control problem arises from the gap between the Expert Pilot Model and Generalised Optimal Control. In this research, we aim to develop an optimal controller that is suitable for real-time implementation. The problem formulation devised by Louam [99] and improved by Prokop [100] provides a structure for setting up the pilot/aircraft preview problem, such that it conforms to the requirements of a standard discrete linear quadratic method. Based on this method, which has been successfully implemented for car steering control by Sharp [13] with a linear vehicle model, we have developed this Predictive Steering Control for optimal ground manoeuvres with a nonlinear aircraft model. Since the aircraft model used in this research is a highly nonlinear system, the original method is modified so that it can be used in this aircraft application. Specifically, the aircraft model is linearised at discrete levels of forward speed and lateral acceleration; then the sequence of optimal control gain is obtained by interpolating between a set of precomputed control gains using lateral acceleration as the measurement. By doing this, we do not need to compute the optimal control gains repeatedly, which improves the controller's real-time capability.

Additionally, rather than projecting the aircraft in a straight line to obtain the reference path lateral profile, as in Sharp's method, the aircraft position is predicted using the well-known steady-state handling equation. It provides a rough prediction of the aircraft trajectory based on the current steering angle, with reasonable accuracy and computational complexity. The whole sequence of road preview is updated every time step, while in Sharp's method the road preview is propagated with only the last preview point updated. This modification can effectively prevent the errors caused by the prediction to accumulate.

To evaluate how much benefit we could get from using this real-time optimal controller, it is compared with the Expert Driver Model in different runway geometries and at different forward speed. The optimality of PSC is evaluated via the comparison with GOC. PSC delivers near-optimal solutions which are more effective and intelligent than what a pilot could achieve. Lastly, a comprehensive robustness study is carried out. A compact version of PSC based on constant control gain sequence is tested, and compared with the original version. From the robustness study we can see that the proposed controller shows good robustness to uncertainties (mass, CG, and road conditions) and disturbances (crosswind).

## 5.2 Controller design

Taking advantage of a similar preview mechanism as in the pilot model, PSC is developed based on an infinite discrete-time Linear Quadratic method. Rather than having only one preview point like the driver model, PSC is based on an estimation of trajectory with equally spaced preview points over the preview horizon, as shown in Fig.5.1. In this method, the aircraft model can be linked with the previewed information of the road via the path preview model, which is defined by a shift register given by Eqn.5.1 and 5.2 (where $y_r$ is the previewed path and $y_{ri}$ is the input to the preview model):

$$y_r(k+1) = Dy_r(k) + Ey_{ri} \tag{5.1}$$

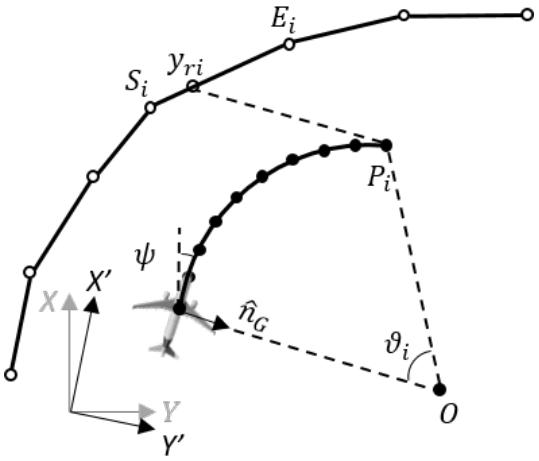


Figure 5.1: Calculation of preview trajectory and lateral reference point.

$$D = \begin{bmatrix} 0 & 1 & 0 & \cdots & 0 \\ 0 & 0 & 1 & \cdots & 0 \\ \vdots & \vdots & \vdots & \ddots & \vdots \\ 0 & 0 & 0 & \cdots & 1 \\ 0 & 0 & 0 & \cdots & 0 \end{bmatrix} \quad E = \begin{bmatrix} 0 \\ 0 \\ \vdots \\ 0 \\ 1 \end{bmatrix} \tag{5.2}$$

The path model is incorporated with a discrete formulation of the aircraft model

$$x(k+1) = A_d x(k) + B_d u(k) \tag{5.3}$$

$$A_d = 1 + \frac{\partial f(x,u)}{\partial x}\Delta t, \quad B_d = \frac{\partial f(x,u)}{\partial u}\Delta t \tag{5.4}$$

The target path for the entire preview horizon is updated at every time-step. At any instant $k$, the path preview data observed by the pilot is a sequence of $(N_p + 1)$ points at and ahead of the aircraft CG ($N_p$ being the preview horizon). The y-coordinates of the preview points $[y_{r0}, y_{r1}, \cdots, y_{rN_p}]^T$ are the actual targets to follow in the case of steering control. At instant $(k + 1)$, the first preview sample (at the current CG position) is lost from the problem; a new sample which is previously outside the problem enters the system as the last sample $y_{ri}$; the rest of the samples from 2 to $N_p + 1$ are shifted so that they become the samples from 1 to $N_p$.

The ground coordinate system should be rotated by current yaw angle $\psi$ every time-step because the aircraft model is linearized at zero yaw angle. Each preview point along the trajectory has a corresponding reference point at the same x-coordinate:

$$\text{if} \quad P_{ix} > S_{ix} \;\&\; P_{ix} < E_{ix} \;, \quad y_{ri} = S_{iy} + (E_{iy} - S_{iy}) \frac{P_{ix} - S_{ix}}{E_{ix} - S_{ix}} \tag{5.5}$$

To improve the accuracy of the path preview model, the whole sequence of y-reference $y_r$ is updated at any instant $k$. Combining the path preview model with the linearized aircraft model, the overall dynamical system is represented as:

$$\begin{bmatrix} x(k+1) \\ y_r(k+1) \end{bmatrix} = \begin{bmatrix} A_d & 0 \\ 0 & D \end{bmatrix} \begin{bmatrix} x(k) \\ y_r(k) \end{bmatrix} + \begin{bmatrix} 0 \\ E \end{bmatrix} y_{ri} + \begin{bmatrix} B_d \\ 0 \end{bmatrix} u(k) \tag{5.6}$$

The two models are linked via a quadratic cost function with respect to the lateral deviation of the aircraft CG from the target path:

$$J = \sum_{k=0}^{k=\infty} \{Z^T(k) \cdot Q \cdot Z(k) + u(k)^T \cdot R \cdot u(k)\} \tag{5.7}$$

$$Z(k) = \begin{bmatrix} x(k+1) \\ y_r(k+1) \end{bmatrix} \quad Q = C^T \cdot C \tag{5.8}$$

$$C = [\underbrace{0 \quad 0 \quad 0 \quad 0 \quad 0 \quad 0 \quad 0 \quad 1 \quad 0 \quad 0 \quad 0 \quad 0}_{\text{system states}} \quad \underbrace{-1 \quad 0 \quad \cdots \quad 0}_{\text{path preview}}] \tag{5.9}$$

The Q matrix is chosen to reflect the system objective and the R matrix is chosen to reflect the cost of using control. The optimal control sequence that minimizes the above cost function is given by:

$$u(k+1) = -K \cdot Z(k) \tag{5.10}$$

where

$$K = (R_p + B^T P_p B)^{-1} B^T P_p A \tag{5.11}$$

and P is the unique positive definite solution to the Discrete time Algebraic Riccati Equation (DARE):

$$P_p = A^T P_p A - A^T P_p B (R_p + B^T P_p B)^{-1} B^T P_p A + Q \tag{5.12}$$

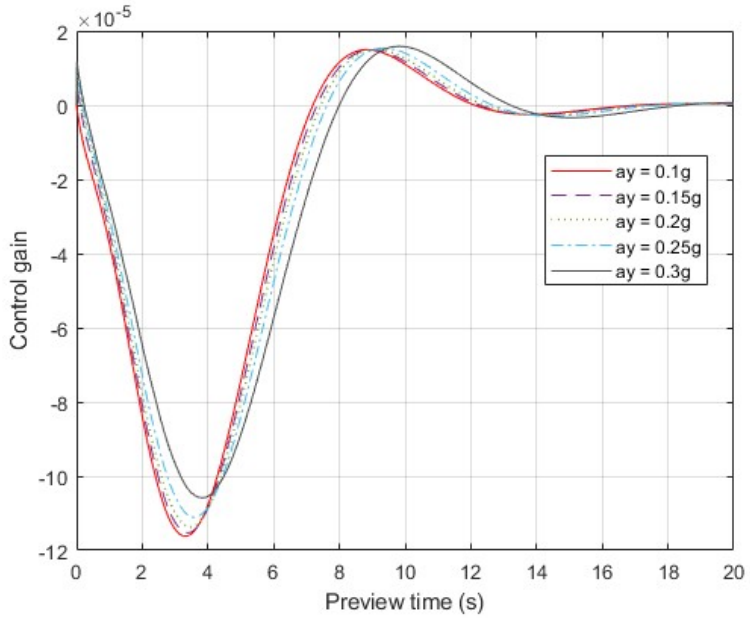


Figure 5.2: Control gains v.s. Preview time

To avoid recomputing the Riccati equation solution at every time-step, all the control gains can be precomputed at each equilibrium point, as shown in Fig.5.2; at any point along the trajectory, a specific control gain vector can be obtained by interpolating between the stored control gains using lateral acceleration as the measurement. Due to the massive inertia of the aircraft, a long preview horizon is needed. In this research, a preview time of 20s is chosen, so that the control gain settles down to zero.

LQR approach exhibits very good stability margins. It selects closed-loop poles that balance between system errors and the control effort by tuning R matrix. Since the closed-loop transfer function is guaranteed to be far from the critical point for all frequencies, Nyquist plot being outside the unit circle centred at (-1,0), then LQR is very robust. See the prove by Anderson et al. [101].

## 5.3 Numerical simulation

In this section, the proposed real-time optimal controller PSC shows its effectiveness and efficiency in terms of aircraft ground path following in a series of numerical simulations. To evaluate its advantage over manually operated ground manoeuvres, PSC is compared with EPM which represents an expert pilot. PSC is examined in three generic runway geometries at a wide range of speed from 10m/s to 25m/s. Based on these simulation results, we can evaluate the safety, effectiveness, and stability of autonomous runway exit using PSC. In terms of the aircraft configuration, a typical landing weight of 54,500kg and a CG position at 30%MAC are considered throughout this section. The aircraft CG is chosen as the reference point when following a given path. To keep consistency with EPM, constant forward speed is considered here, which is controlled by the same PI controller. In order to make comparison, both controllers are tuned to achieve the same control cost and hence the track cost can be compared. Therefore, the track cost and control cost are calculated by the same equations throughout this section in order to evaluate the controllers' performance:

$$L_{track} = \int_0^T d^2 dt \tag{5.13}$$

$$L_{control} = \int_0^T 100\delta^2 dt \tag{5.14}$$

where $d$ is the lateral deviation in meters and $\delta$ is the steering angle in radians.

### 5.3.1 45° runway exit

A 45° runway exit is firstly considered as a generic ground manoeuvre. At low speed ($10m/s$) and medium speed ($15m/s$) in a 45-degree runway exit manoeuvre, both EPM and PSC are able to perform a good path following, as can be seen from the aircraft CG trajectories in Fig.5.3. From their lateral deviations to the target path as shown in Fig.5.4, it can be seen that PSC performs a better path following than EPM, with a lower level of maximum

lateral deviation. More importantly, compared to EPM, it significantly reduces the oscillations of steering input after the corner. These oscillations are caused by the correction of the aircraft attitude and position, which in turn results in a higher track cost. Both the control cost and track cost of PSC and EPM are given in Tabel.5.1. Based on the same control cost, PSC achieves a much lower track cost, e.g. it could be less than half of the track cost of EPM at a speed lower than 25m/s.

Fig.5.5 shows the steering input of both controllers, from which we can see the difference between their steering strategies. A positive steering angle

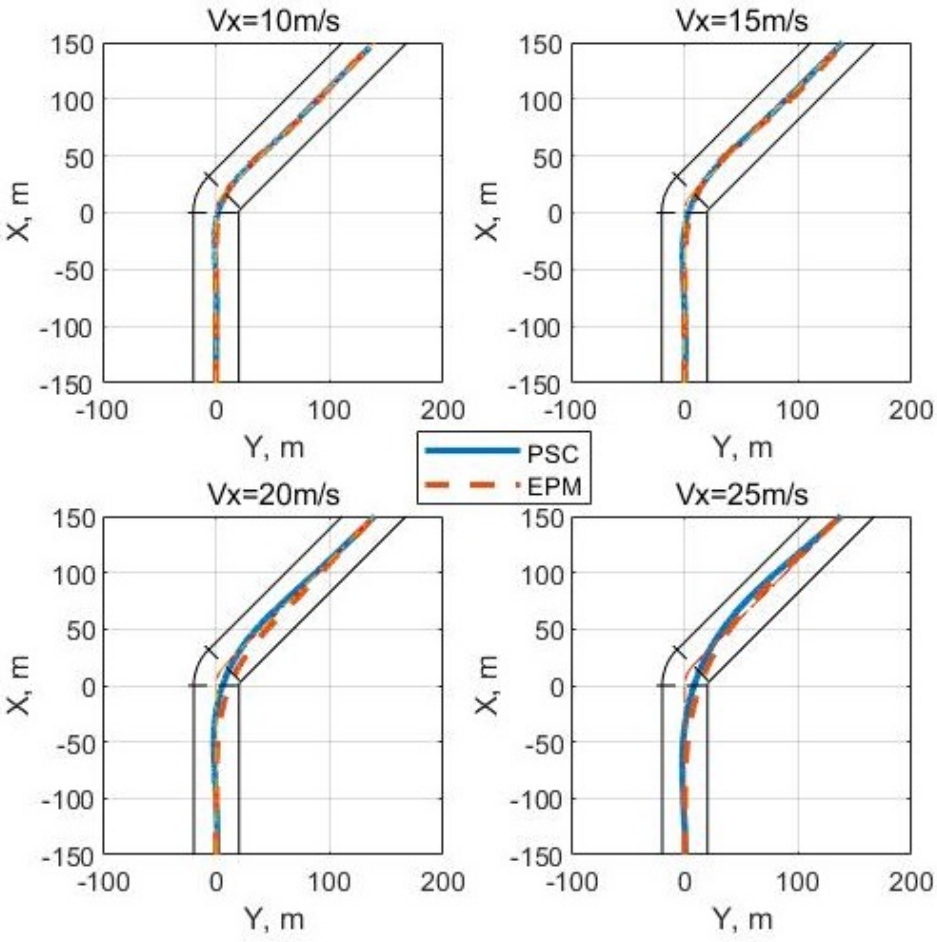


Figure 5.3: Aircraft trajectories of PSC and EPM at various speed.

| | $10m/s$ | $15m/s$ | $20m/s$ | $25m/s$ |
|---|---|---|---|---|
| Control cost | 21.0 | 15.1 | 15.1 | 13.6 |
| Track cost PSC | 21.2 | 50.0 | 111.0 | 278.1 |
| Track cost EPM | 48.3 | 121.1 | 263.1 | 336.4 |

Table 5.1: Control cost and track cost of PSC and EPM at various speed.

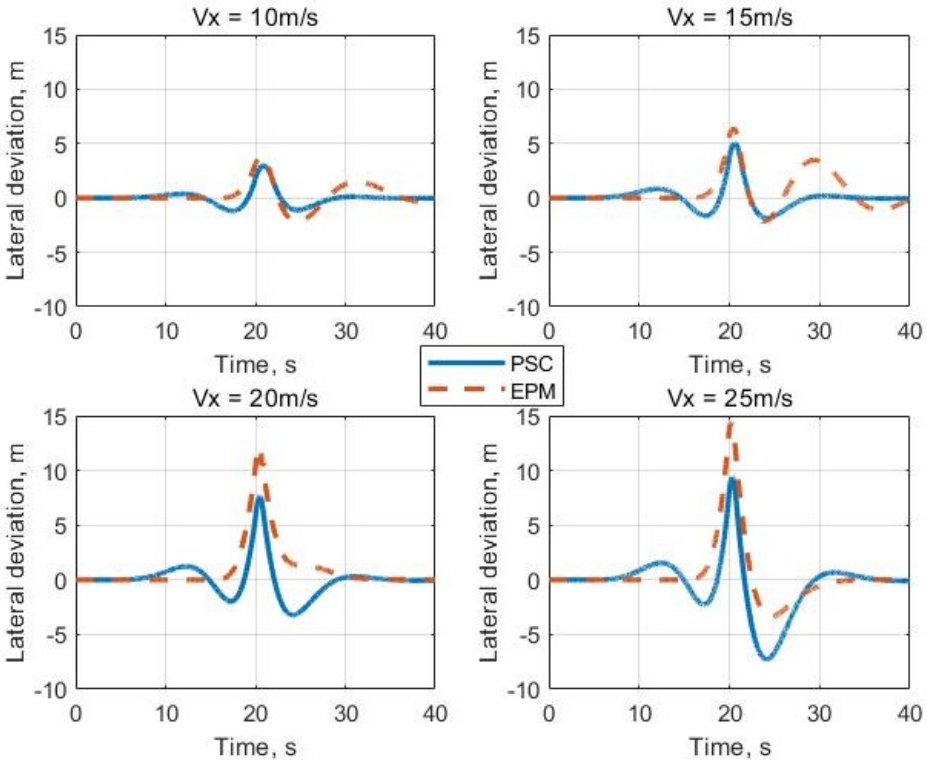


Figure 5.4: Lateral deviation of PSC and EPM at various speed.

indicates that the aircraft is steered to the right. In the pilot model, there is no steering input until the preview point reaches the first non-zero Y-reference. After the aircraft has passed the corner, it needs a long time and distance to settle down, which significantly increases the track cost. In comparison, PSC performs a preview-oscillation of steering which starts at a long distance before the corner. Since the road information propagates from the farthest preview point to the nearest preview point, the first non-zero reference point entering

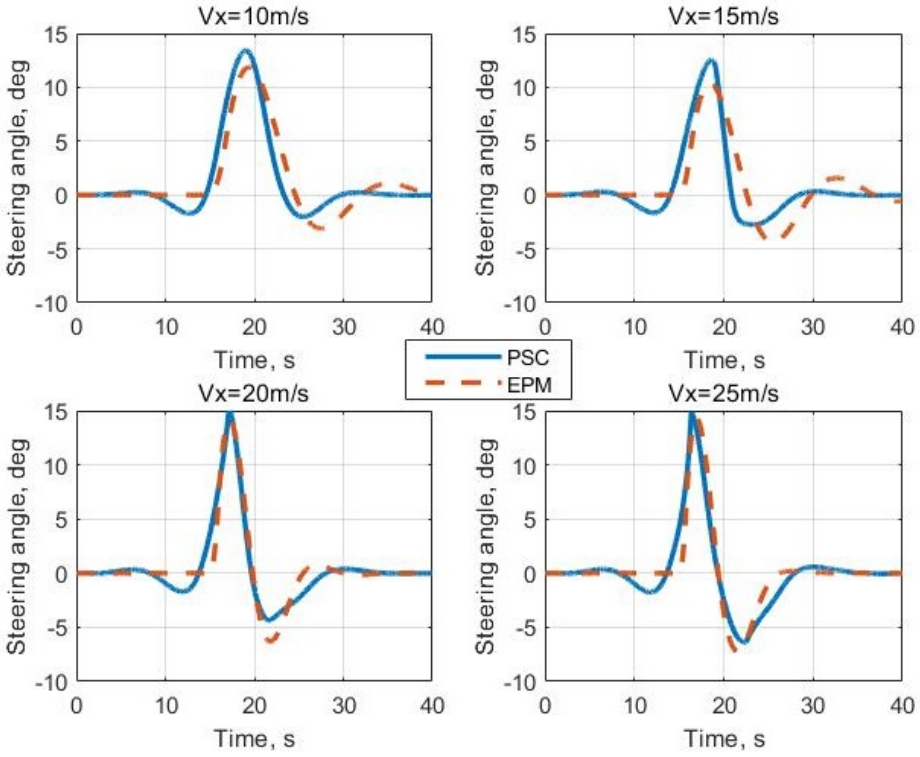


Figure 5.5: Steering angle of PSC and EPM at various speed.

the preview system (which is positive in this right-hand exit manoeuvre) will be multiplied by the last element of the control gain sequence. As the previewed information is propagated within the path preview model, it will experience oscillatory control gains as depicted in Fig.5.2. Therefore, the aircraft is able to build up oscillatory yaw momentum as a result of the oscillations in the steering input. By doing this, the aircraft is able to follow the path more easily via a larger turning radius. Moreover, the aircraft settles down quickly and stays closer to the centreline without excessive corrections after the corner.

The lateral accelerations are shown in Fig.5.6. Both controllers experience a similar level of maximum lateral acceleration around $0.15g$ at $10m/s$ and $0.2g$ at $15m/s$, which are both below the $0.5g$ limit. While the aircraft controlled by PSC settles down to zero lateral acceleration quickly after the corner, a longer period of oscillation in the lateral acceleration is caused by EPM due

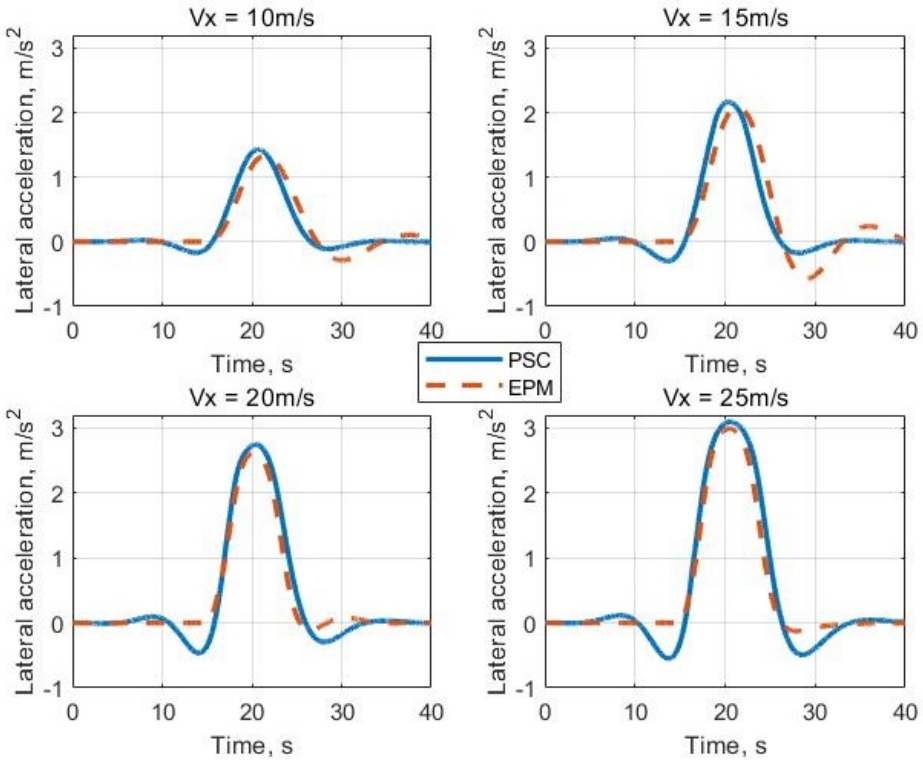


Figure 5.6: Lateral acceleration of PSC and EPM at various speed.

to its oscillatory steering input. In conclusion, at low and medium speed, PSC performs a better path following than EPM.

As the forward speed rises to $20m/s$, the difference between the two controllers becomes more significant. Both the peak and average of the lateral deviation are greatly reduced. From the aircraft trajectories in Fig.5.3, it can be seen that the trajectory of PSC stays closer to the centreline; EPM cuts the corner with the trajectory closer to the apex. It is noticeable that at any speed between 10m/s and 20m/s, based on the same control cost, the track cost of EPM turns out to be around 2.5 times higher than that of PSC.

In Fig.5.4, the track errors of both controllers are plotted against time. It can be seen that PSC is effective and efficient at tracking the target path at high speed. It takes the same control strategy of preview-oscillation of steering as in the lower speed case. This control strategy allows the aircraft to apply

steering in advance to benefit from an enlarged turning radius, but without compromising the safety by operating too close to the apex. In this way, the maximum lateral deviation is largely reduced which leaves a wider safety margin for the runway exit manoeuvre. Unlike PSC, which uses a sequence of preview points, EPM is based on only one preview point. Therefore, EPM is not able to plan a manoeuvre ahead of time, because it does not have full knowledge of the road curvature. Steering angle and lateral acceleration are plotted in the bottom left panel of Fig.5.5 and Fig.5.6 respectively. A massive steering input is built up over a short period between 15s and 20s. This rapid increase of steering angle would quickly correct the aircraft's orientation and hence reduce the oscillatory correction after the corner. This sharp rise of steering angle, however, does not affect the aircraft lateral acceleration; PSC and EPM have a same level of maximum lateral acceleration around $0.28g$.

To investigate extra high-speed runway turnoff, a forward speed of $25m/s$ is simulated. From the trajectories shown in Fig.5.3, it can be seen that PSC overshoots the centreline further than EPM, which stays closer to the apex due to corner cutting. Based on the same control cost, PSC achieves a lower track cost of 278.1 compared to EPM (336.4). Considering the lateral deviation limit set at 15m which is the same as in Chapter3, EPM is right at the limit which could be dangerous in practice. In contrast, PSC reduces the maximum lateral deviation by 4-5m which would significantly improve safety. In conclusion, as a method based on the prediction of aircraft trajectory and road curvature, PSC is more effective and stable than EPM.

### 5.3.2 30° runway exit

Both automatic controller and pilots are able to handle a 30° runway exit manoeuvre more easily compared to a 45° runway exit manoeuvre. In fact, this runway geometry is more widely used globally. The benefit we can get from an automated runway turnoff would decrease in this less challenging scenario. Since this runway geometry is designed for high-speed turnoff, PSC is only

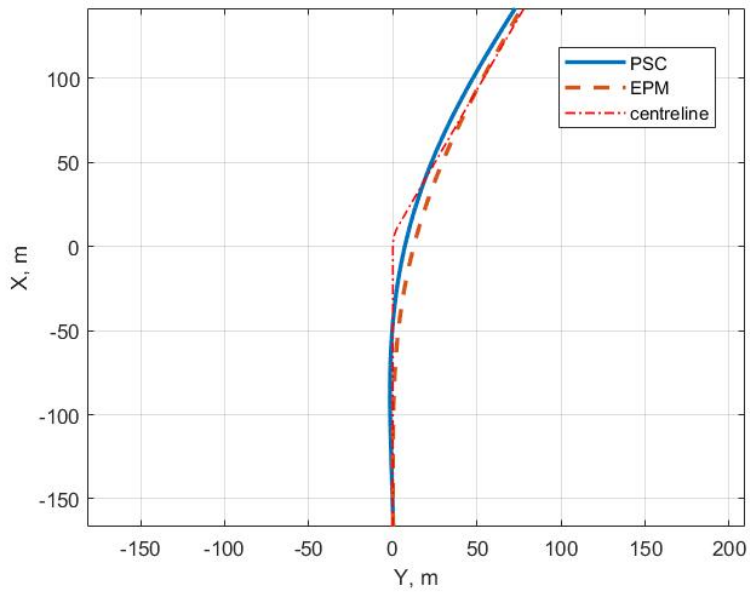


Figure 5.7: Aircraft trajectories of PSC and EPM at 30m/s.

tested at the design speed (30m/s); in addition, the advantage of PSC over a pilot at the expert level is illustrated by the comparison with EPM.

The aircraft trajectories are illustrated in Fig.5.7. As for the 45° runway exit manoeuvre, PSC steers the aircraft to the left to achieve an enlarged turning radius. Instead of using a preview-oscillation steering strategy, EPM steers the aircraft to the right directly. Overall, PSC performs a better path following in this case. It controls the aircraft to traverse more closely to the centreline through the corner although it needs a longer period to get back to the centreline after the corner.

A more detailed comparison is shown in Fig.5.8. The top panel shows the lateral deviation from which we can see that PSC has a lower peak value. The maximum lateral deviation is of more importance since it indicates how much safety margin is provided by the controller. The aircraft lateral acceleration is illustrated in the middle panel. The aircraft starts to build up oscillatory yaw momentum as early as 15s prior to the corner. In this way, the effect

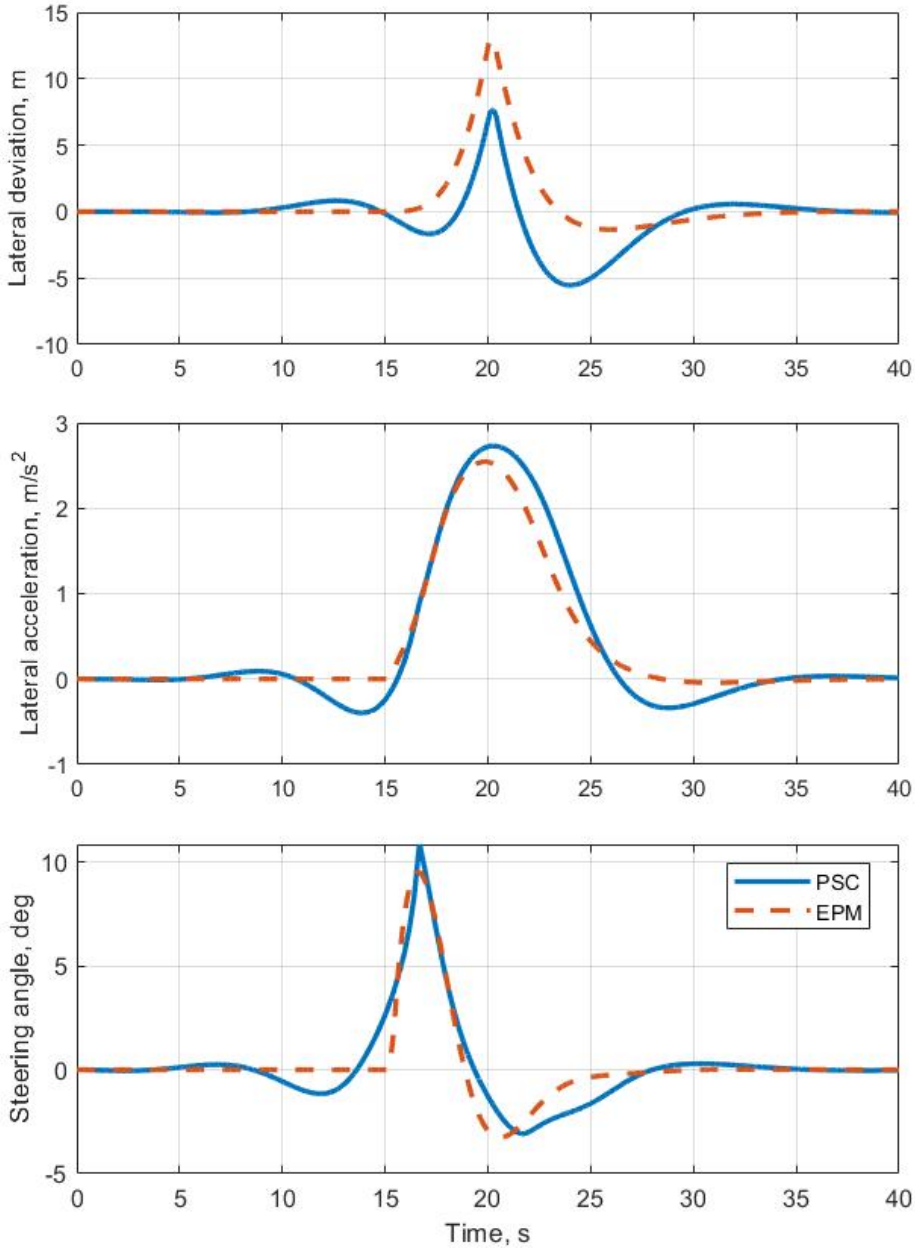


Figure 5.8: Comparison between PSC and EPM in a 30° runway geometry.

of the system inertia is minimized such that the aircraft is able to negotiate a turn more easily. Although the difference between PSC and EPM is not as significant as in a 45° runway exit, the aircraft ground operations can still benefit from the control strategy of PSC which is more effective.

### 5.3.3 90° runway exit

A right-angle runway exit is one of the most challenging ground manoeuvres for not only a pilot, but an automatic controller as well. As discussed in Section 3.5.2, EPM is able to execute a 90° runway exit with the maximum forward speed at 14m/s; when the forward speed rises to 15m/s the aircraft cannot follow the centreline properly, ending up with massive lateral deviation and oscillations. To evaluate effectiveness of the proposed optimal controller in this scenario, PSC is examined and compared with EPM at two different speeds: low speed of 10m/s and medium speed of 15m/s.

The top two panels of Fig.5.9 illustrate the aircraft trajectories at two different forward speeds respectively. It can be seen that PSC follows the centreline with less track error than EPM, especially at higher speed. At 10m/s, based on the same control cost, PSC achieves a lower track cost than EPM despite a slightly higher maximum lateral deviation as illustrated in the middle-left panel; at 15m/s, the aircraft controlled by PSC experiences much lower track error with even less steering input. The quality of this extreme manoeuvre is significantly improved by using PSC which can easily negotiate this runway geometry without excessive corrections. While EPM totally fails to execute a 90° runway turnoff at 15m/s, PSC is still able to handle this speed properly with CG staying within the prescribed safety boundary. Steering inputs are illustrated in the bottom panels. The two controllers have a similar level of maximum steering angle around 25 degrees. However, their steering strategies are substantially different. PSC takes oscillatory steering action before the corner to build up the aircraft's yaw momentum, while EPM takes oscillatory steering action after the corner to correct residual track errors. By

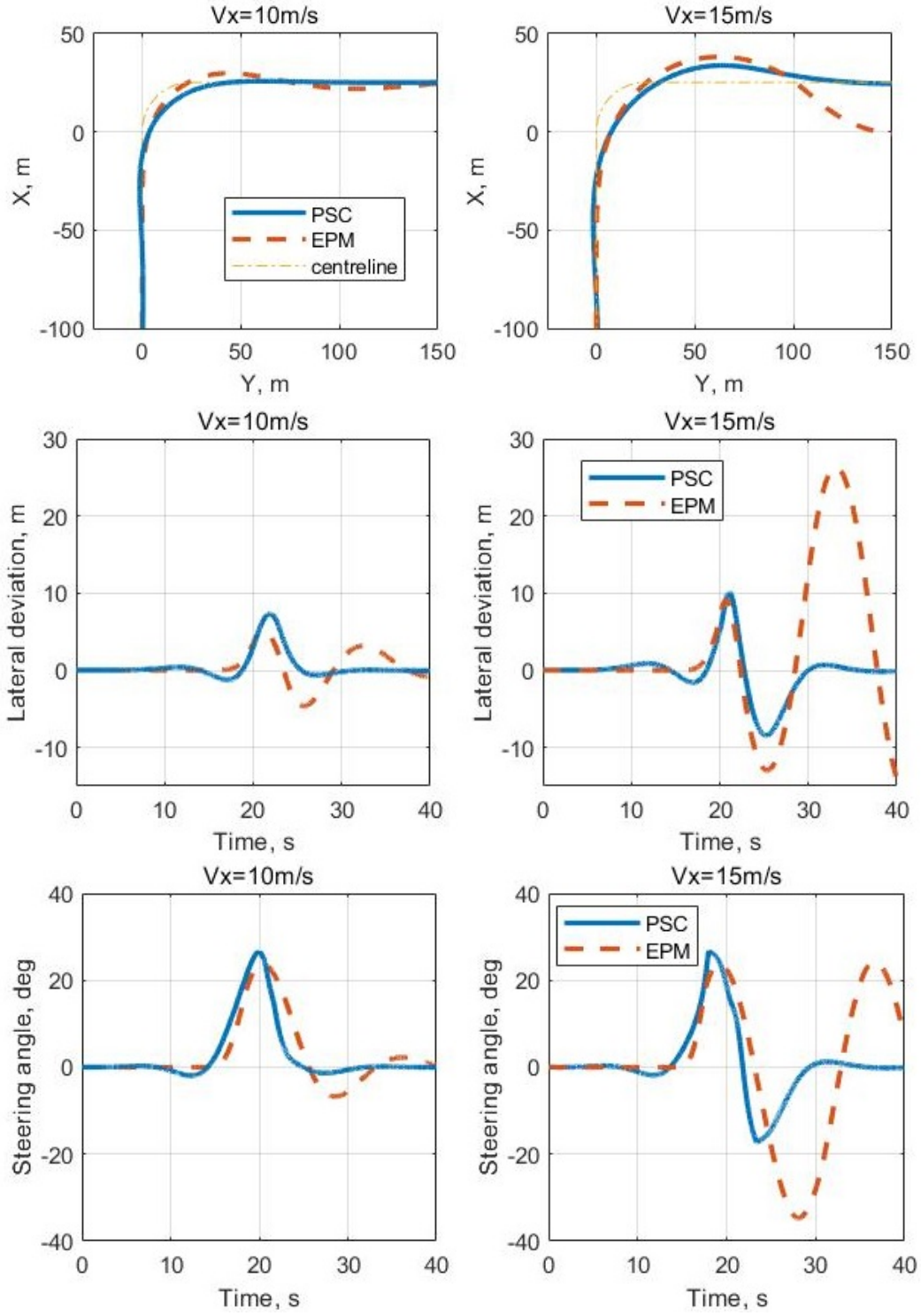


Figure 5.9: 90° runway exit controlled by PSC and EPM at 10m/s and 15m/s.

employing this preview-oscillation steering strategy, PSC maintains the lateral deviation below 10m through and after the corner. With sufficient safety margin maintained to the edge of the runway, PSC is able to execute a right-angle runway exit at a speed that is 3 times as fast as a typical 5m/s for manually operated aircraft. Given that 15m/s is an extremely high speed for this particular manoeuvre, PSC shows its strong capability of steering control, especially at a high speed.

## 5.4 Optimality of PSC

In this section, GOC is employed as a benchmark, based on which we can evaluate the optimality of PSC. PSC is compared with the optimal solution identified by GOC at 20m/s. Here we use the same optimal solution as in Sec-

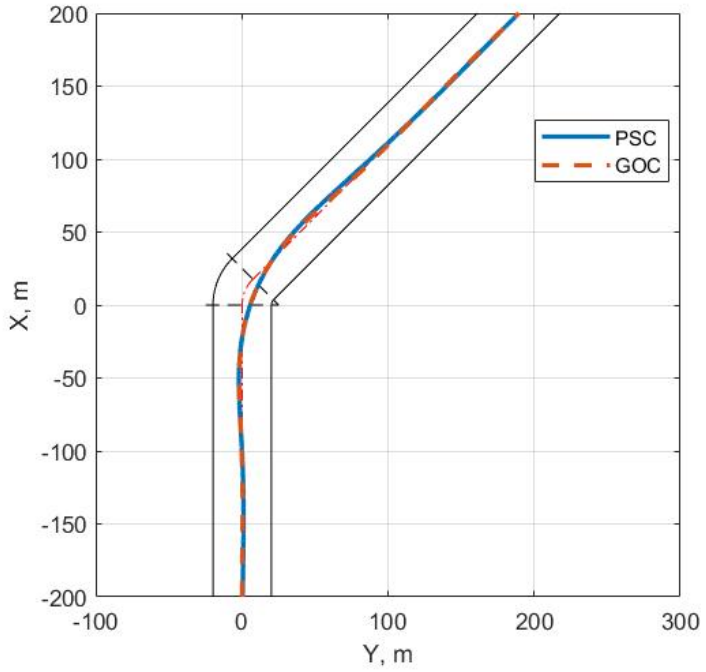


Figure 5.10: Aircraft trajectory of PSC and GOC at 20m/s.

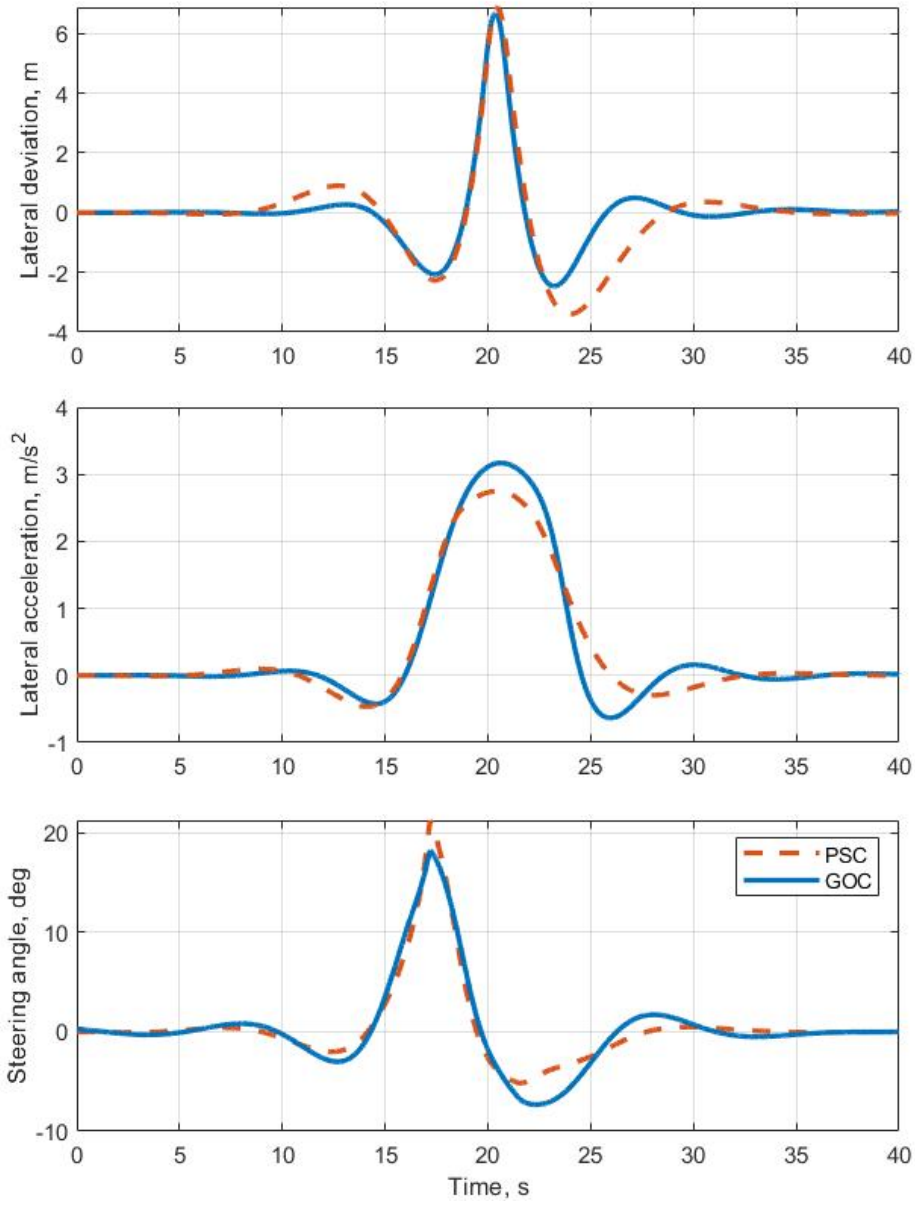


Figure 5.11: Comparison between PSC and GOC in a 45° runway exit at 20m/s.

tion 4.4. The aircraft trajectories of PSC and GOC are illustrated in Fig.5.10. It can be seen that PSC executes a runway exit manoeuvre which is very close to the optimal solution; the trajectory of PSC largely overlaps with the optimal trajectory. The difference between these two trajectories can hardly be seen despite the reduction of track cost achieved by GOC. The lateral deviations are plotted in the top panel of Fig.5.11, from which we can see that PSC and GOC have a similar track error history with the same peak value. However, two minor differences in the magnitude of lateral deviation can be observed; the aircraft controlled by PSC experiences slightly higher track error both before and after the corner. Additionally, the variation of sign illustrates how the aircraft negotiates this runway exit manoeuvre by oscillating around the centreline; PSC has a similar variation of sign compared to GOC, but with a small phase shift. The steering angles of both controllers are illustrated in the bottom panel. PSC takes advantage of the preview-oscillation steering strategy which is the same as the optimal solution. PSC applies an oscillatory steering input with lower magnitude compared to the optimal solution, which results in the increase of track cost. Since the implementation of PSC involves linearisation of the aircraft model and a rough estimation of the aircraft trajectory, its feedback control gain may not be the optimal one in terms of minimizing track error. But it still can be considered as a near-optimal controller, which is computationally efficient and suitable for real-time implementation.

## 5.5 Tyre behaviour

The tyre behaviour is the most important factor that has direct influence on the aircraft movement on the ground. At a typical taxiing speed, e.g. 20m/s, the tyre/ground forces are much higher than the aerodynamic forces. Therefore, the tyre capabilities fundamentally affect the aircraft stability boundary and hence the physical limit of ground manoeuvres. In this section, we look into the tyre behaviours to investigate the reason behind the difference in the three controllers' (EPM, GOC, PSC) performance. A 45° runway exit at 20m/s is

considered as an example scenario.

When a steering action is applied on the nose gear, the direction in which the wheel is pointing becomes different to the direction in which it is actually travelling. Due to the tyre slipping sideways, a lateral velocity is developed in its local coordinate system, as shown in Fig.5.12. The oscillations in the tyre lateral velocity can be observed in GOC and PSC due to the oscillatory steering input. The optimal solution from GOC has the highest lateral velocity among the three controllers, which might be a disadvantage because it causes more tyre wear.

In the tyre coordinate system, the angle between the forward velocity and the resultant velocity is know as the slip angle. It determines how much lateral force is generated by the tyre; the lateral force increases nonlinearly with the slip angle until it achieves the optimal slip, at which point the tyre becomes saturated and the lateral force starts to decrease. The tyre slip angles and optimal slips are illustrated in Fig.5.13. In a right-hand turn, the optimal slip of the right gear is decreased due to the weight transfer between landing gears. It can be seen that in GOC, the right gear is closer to the saturation point compared to the other two controllers. The optimal solution tends to make the most of the tyres' capacity; while in PSC, the maximum slip angle of the right gear turns out to be 3 degrees lower than the optimal slip. The lateral force generated by each gear is shown in Fig.5.14; it can be seen in the middle panel that the three controllers have the same peak value despite the small difference in the slip angles. Near the optimal slip angle, the tyres do not generate more lateral grip regardless of whether the tyre saturates or not. Indeed, tyre saturation can be dangerous for ground manoeuvres, causing the aircraft's skidding and loss of control. Therefore, in view of the safety of ground operations, PSC provides an advantage over GOC with near-optimal performance.

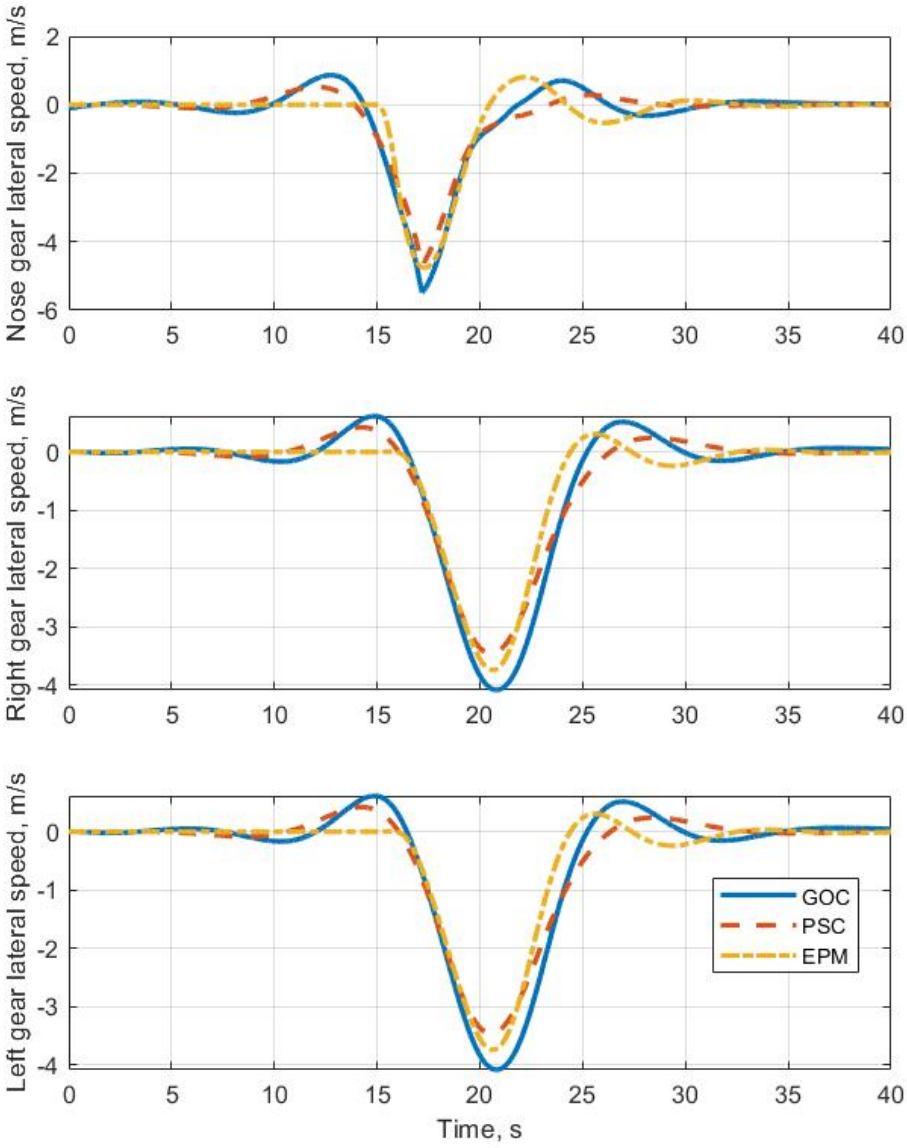


Figure 5.12: Lateral velocity of the nose, right and left landing gear.

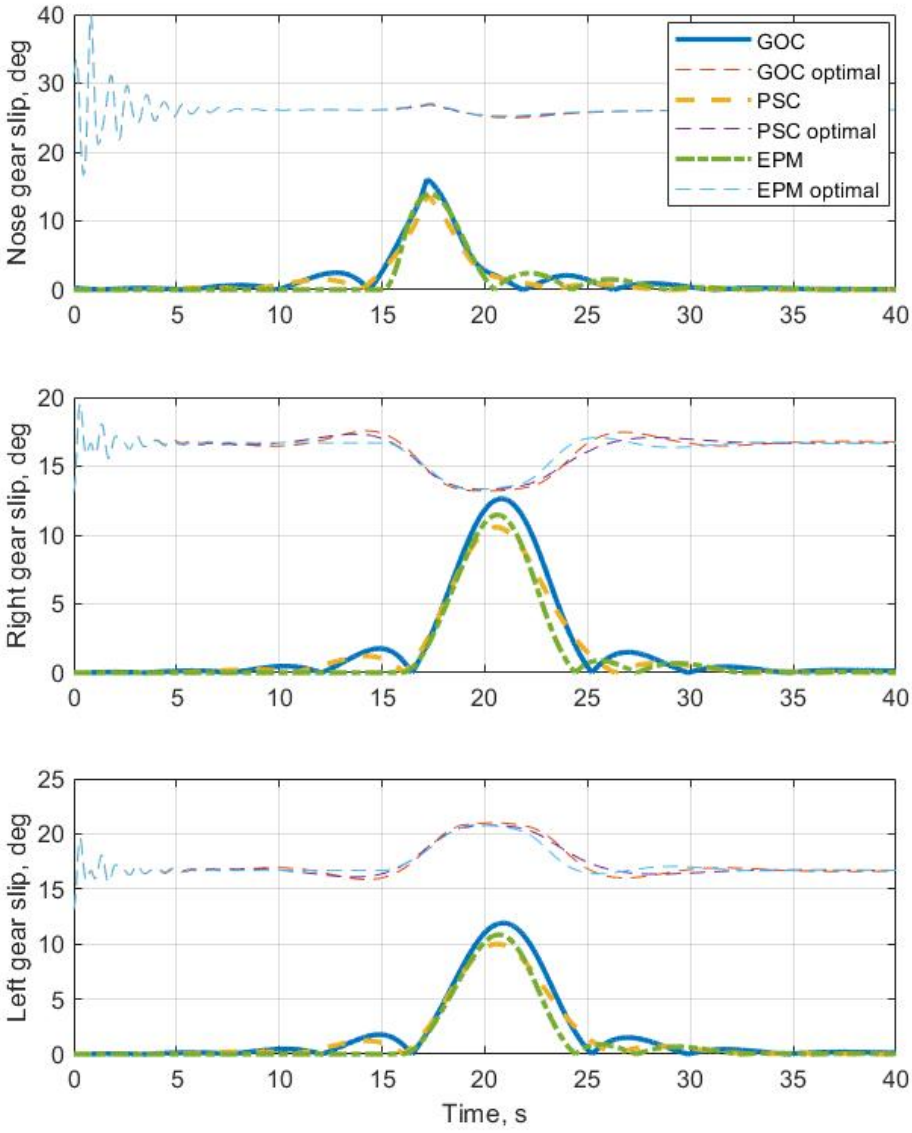


Figure 5.13: Slip angles and optimal slip of the nose, right and left landing gear.

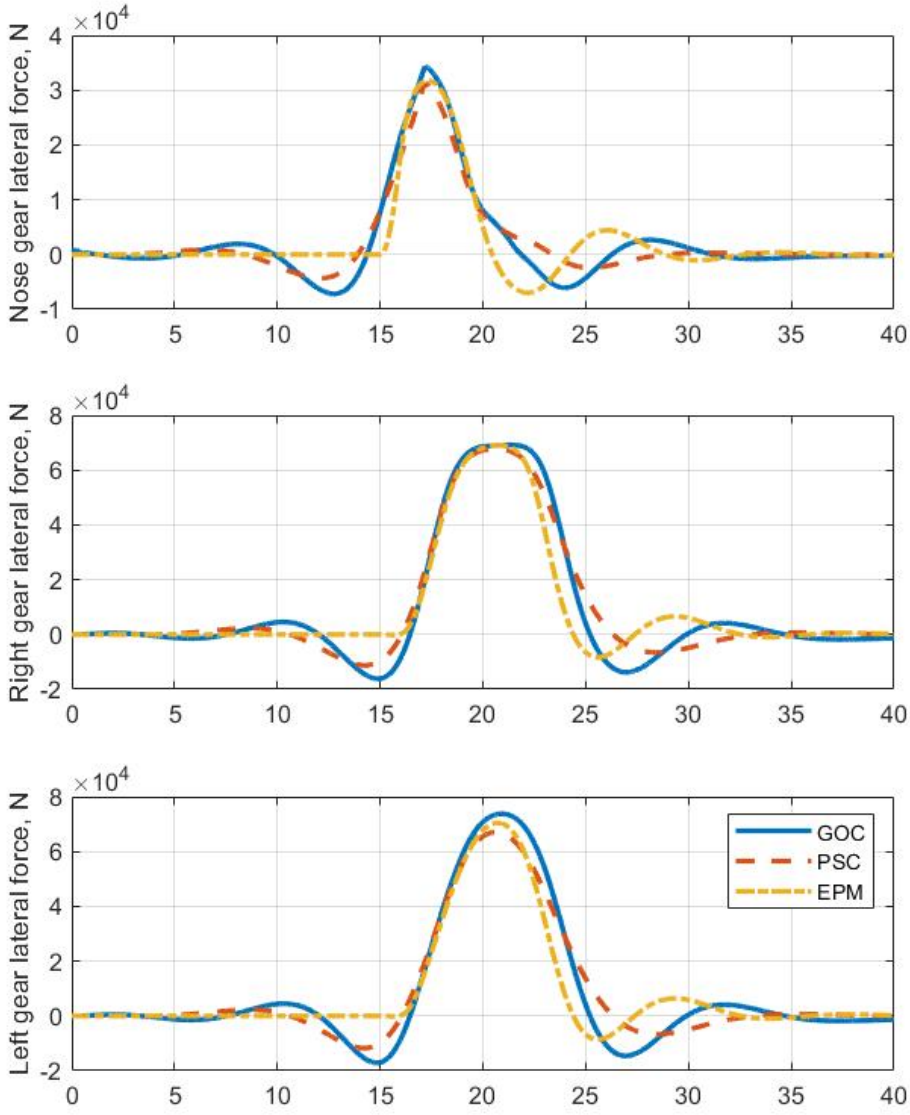


Figure 5.14: Lateral force on the nose, right and left gear.

## 5.6 Robustness study

In this section, the proposed controller's robustness to uncertainties and disturbances is studied in a 45° runway exit manoeuvre at 15m/s. Throughout the robustness study, all the simulations are based on the same set of control gains which are obtained with the nominal aircraft configuration (a total weight of 54500Kg with a forward CG position of 30%MAC).

Firstly, to investigate the controller's sensitivity to the control gain at discrete lateral accelerations, we develop a compact version of PSC (PSCC). Specifically, PSCC uses a fixed control gain sequence which is obtained by taking the average of all the control gains at different lateral acceleration levels. Afterwards, PSCC is tested with uncertainties including the aircraft's total weight, CG position, road friction coefficient and tyre conditions. These factors would largely change the dynamics of the aircraft hence the stability of the controller. The baseline case is based on the nominal configuration on a dry road surface (friction coefficient of 1). Without re-tuning the controller, PSCC is employed to control the modified aircraft model on different runway conditions. The results are then compared with the baseline.

### 5.6.1 Constant control gain

In the original PSC method, a transient control gain is identified via interpolation between the precomputed set of control gains. To make the control law more compact and computationally efficient, PSC with constant control gain (PSCC) is proposed here. The constant gain is obtained by taking average of the whole set of control gains. The averaged control gains at different speeds are illustrated in Fig.5.15. PSCC is tested at various speeds from 10m/s to 20m/s. The track cost and control cost are illustrated in Fig.5.16. Using the averaged control gain, PSCC tends to apply less steering which results in a slightly higher track cost. Lateral deviation and lateral acceleration are plotted in Fig.5.17. It can be clearly seen that all the results by PSCC are very close

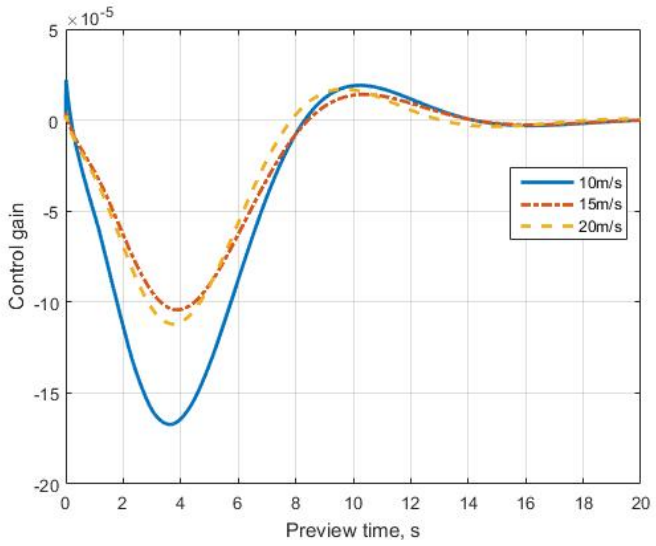


Figure 5.15: Averaged control gains at different speeds

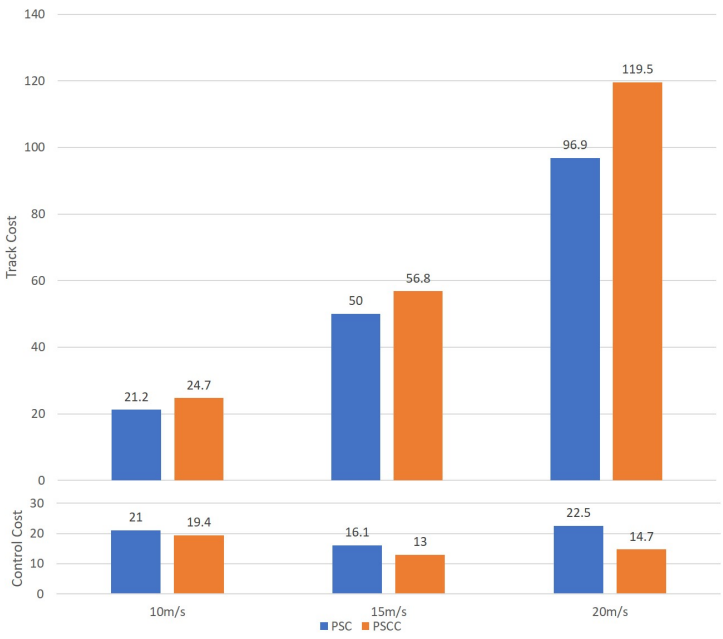


Figure 5.16: PSC v.s PSCC at different speeds

to the baseline (PSC). In this way, this compact version of PSC is validated and the following robustness analysis will be based on PSCC. The computation speed of PSC and PSCC are very close despite PSCC running slightly faster than PSC by 0.001s for each time step. This is because the interpolation in PSC is very efficient and most of the computation time is spent on the calculation of the 2,000 preview points. The computation of control algorithm takes around 0.1s for a single time step of 0.01s running on a desktop with Intel Core i5-4460 CPU. The computation speed can be significantly increased by a more powerful multi-core processor and parallel programming.

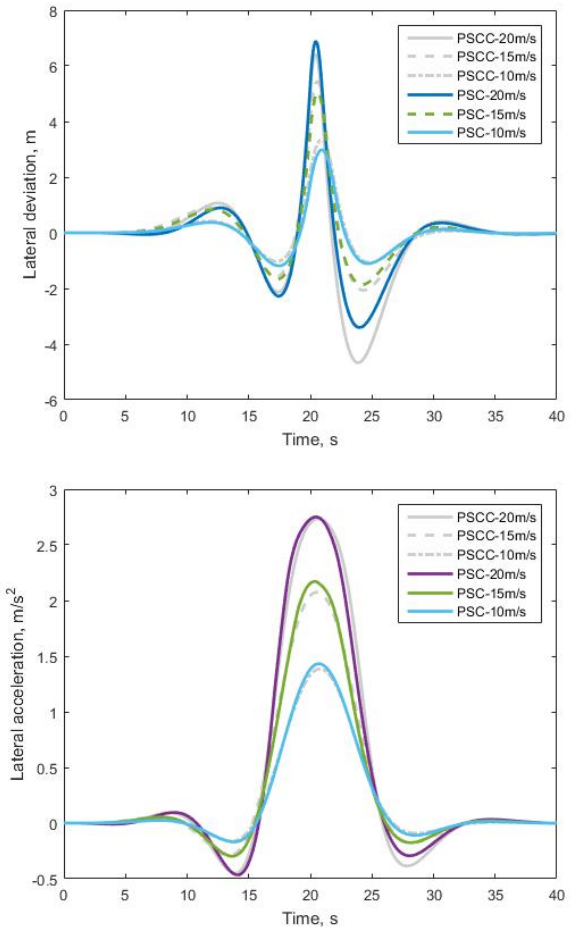


Figure 5.17: PSCC v.s. PSC at different speeds

### 5.6.2 Weight and CG

To investigate the proposed controller's sensitivity to the two most basic parameters weight and CG, the aircraft total mass is varied between 49500kg and 64500kg; the CG is varied between 26% and 32% along the mean aerodynamic chord. The controller has a fixed control gain which is based on the nominal configuration (54500kg, 30%MAC). All the cases turned out to be stable; the

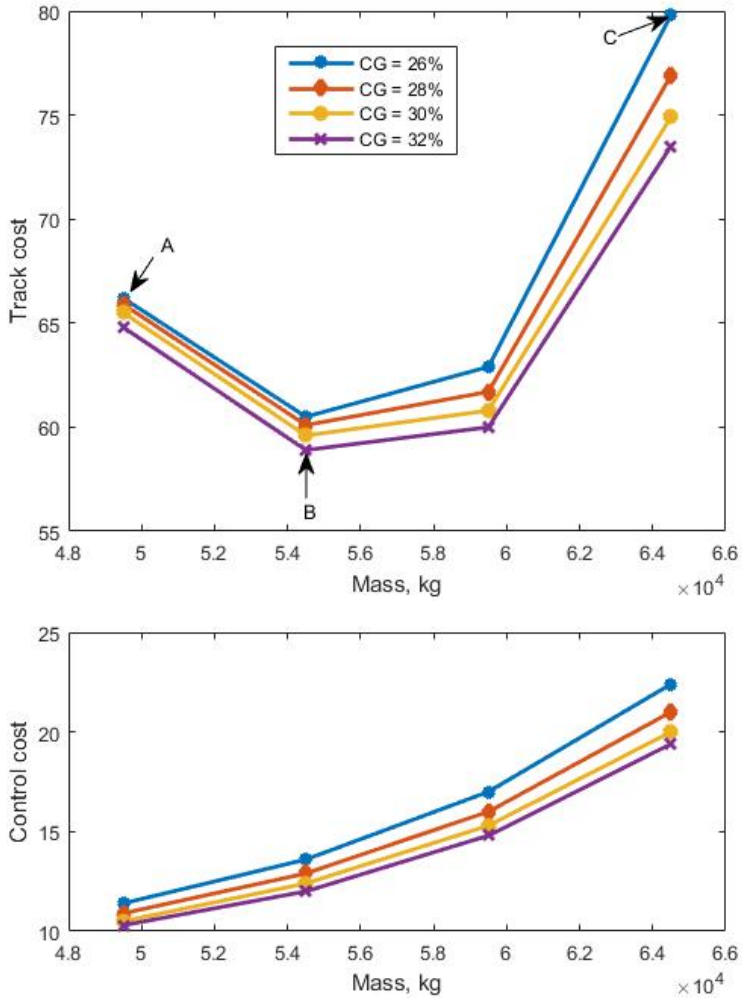


Figure 5.18: Control cost and track cost for different mass and CG position

track cost and control cost are shown in Fig.5.18.

It can be seen that within the range of standard operational mass and CG position, the proposed control law is stable and effective in the presence of uncertainties. Particularly, with a more rearward CG position, the controller achieves a lower track cost with less amount of actuation. Considering aircraft CG is usually moving backward due to the reduction of fuel load, the uncertainties in total mass could be compensated by this effect. Trajectories are plotted for three typical configurations in Fig.5.19. The variation of track cost doesn't result in a big difference of trajectories, which implies that the

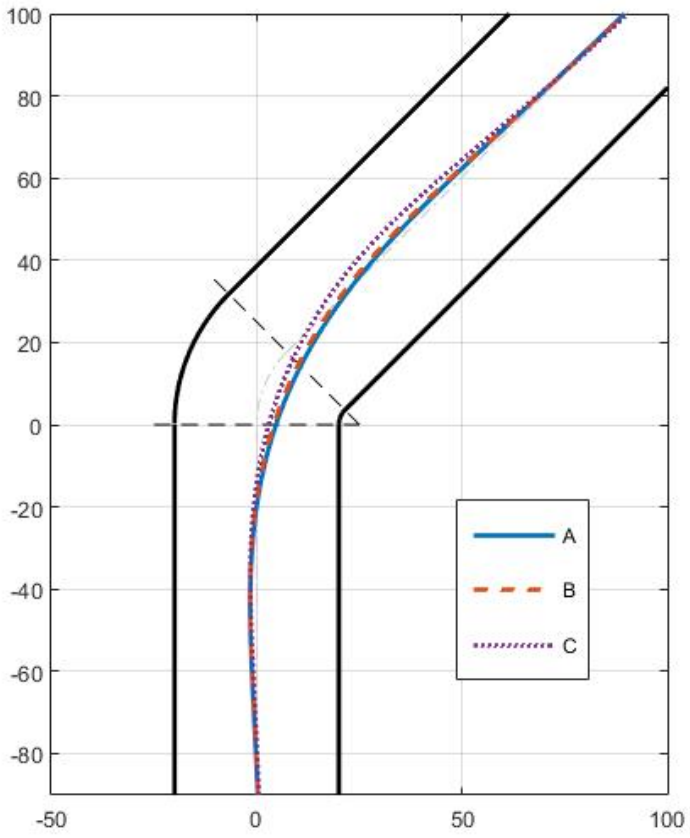


Figure 5.19: Aircraft trajectories for different mass and CG position

controller is robust to varying mass and CG position. Particularly, the larger aircraft mass (configuration C) results in a higher track cost but with lower maximum lateral deviation during the corner. In this case, the aircraft would be further away from the runway boundary due to less corner-cutting.

### 5.6.3 Runway conditions

In addition to the mass and CG, tyre/ground friction force is another factor that would greatly change the aircraft's behaviour on the ground. Tyre/ground forces are mainly affected by the runway condition and tyre characteristic (e.g. tyre pressure). The original tyre model is multiplied by a factor(normalized coefficient of friction) to represent different surface conditions. PSCC is then

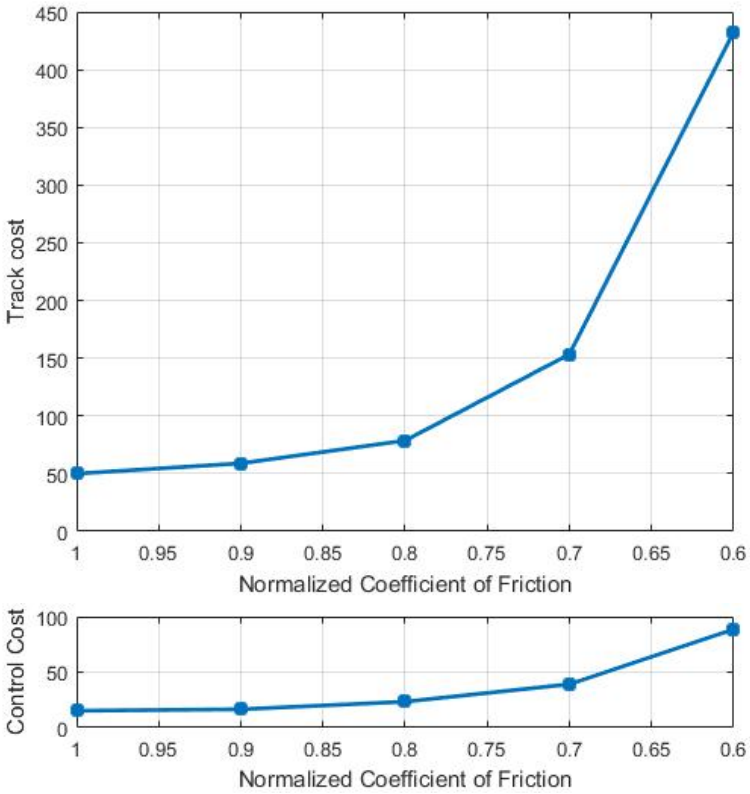


Figure 5.20: Track cost and control cost on different runway conditions

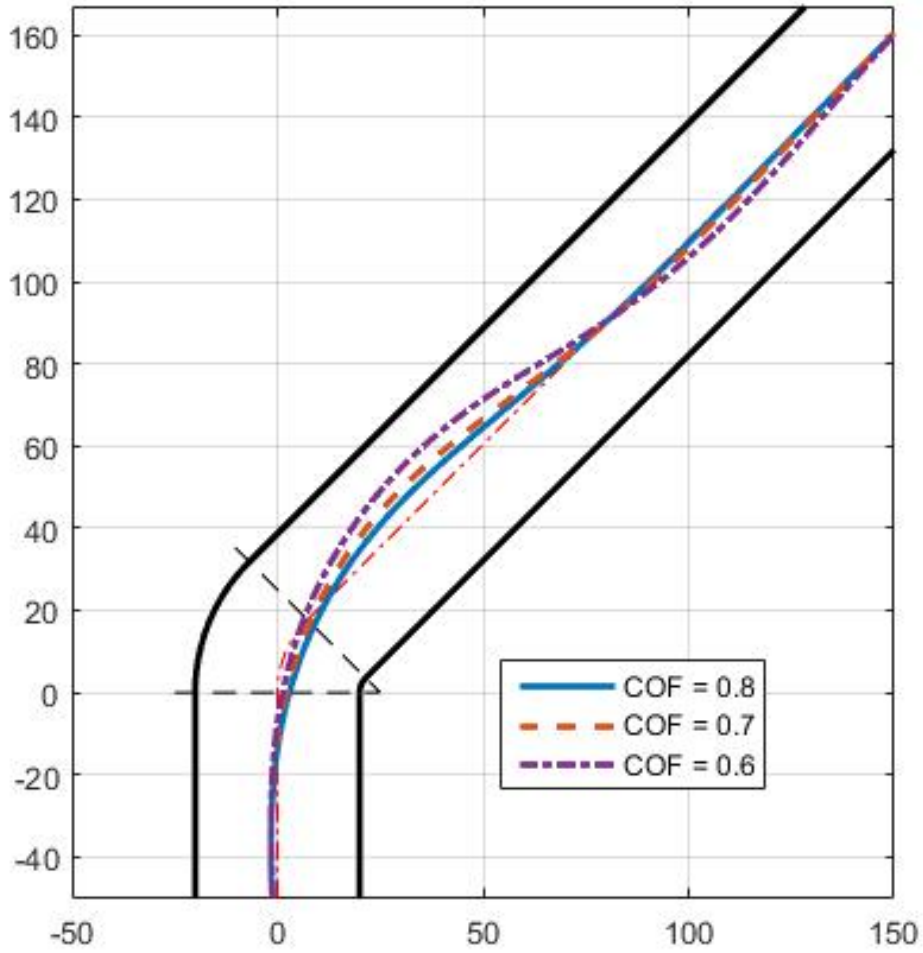


Figure 5.21: Trajectories on different runway conditions

examined on different road conditions with coefficient of friction varying from 0.6 to 1 which is the baseline. The forward speed is set to 15m/s which is a typical exit speed. The track cost and control cost are illustrated in Fig.5.20. With decreased coefficient of friction, both the track cost and control cost increase dramatically. Trajectories for cof of 0.8, 0.7 and 0.6 are depicted in Fig.5.21. The controller can safely cope with COF greater than 0.7 with

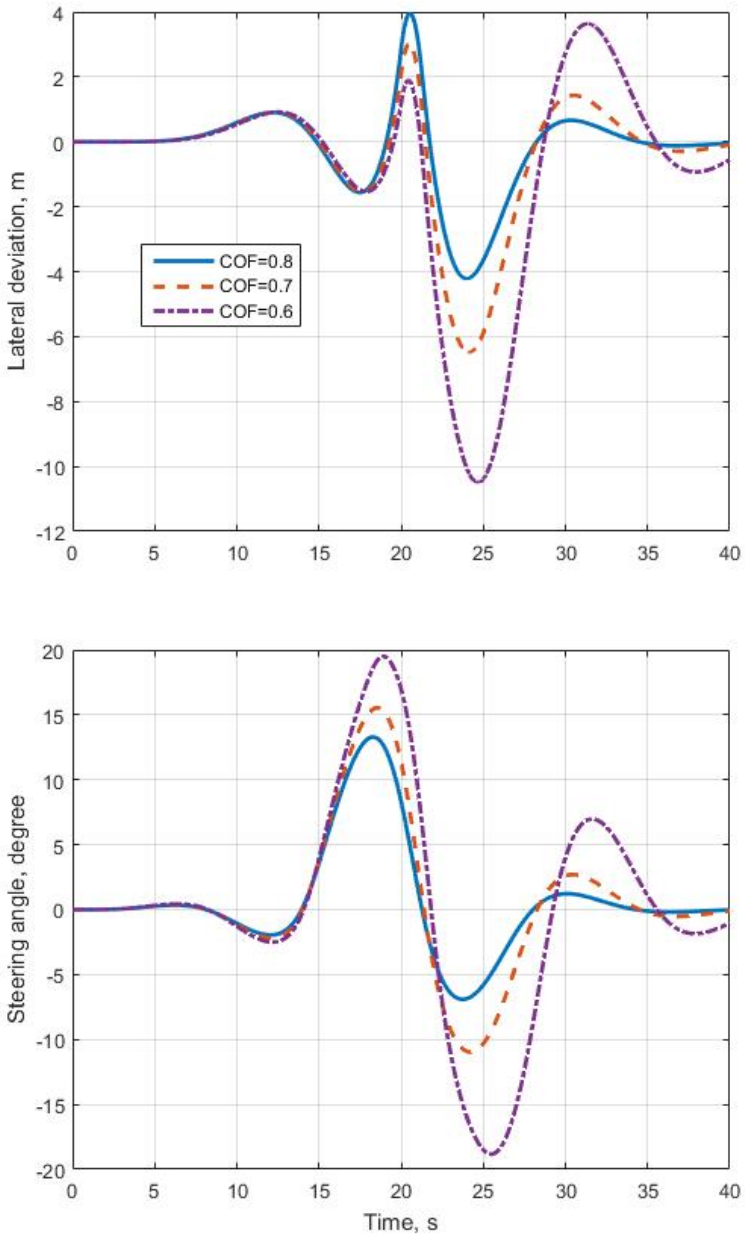


Figure 5.22: Lateral deviation and steering angle on different runway conditions

maximum lateral deviation around 6 meters as shown in Fig.5.22. When COF goes down to 0.6, it becomes challenging to make a 45-degree runway exit manoeuvre. The aircraft overshot the centreline by more than 10 meters before the track error could be corrected by massive steering actuation. Therefore, with COF lower than 0.7, the forward speed must be reduced and the control gain should be re-tuned accordingly.

### 5.6.4 Crosswind disturbance

Aircraft on the ground are subject to disturbances, for example crosswind which is a significant component of prevailing wind perpendicular to the runway centre line. The proposed controllers are examined in the presence of a constant crosswind (varying from 5m/s to 20m/s) from west to east, which generates a negative yaw moment. From the track cost and control cost as illustrated in Fig.5.23, it can be seen PSCC tends to use dramatically increased steering to achieve the same level of total track error. Fig.5.24 and Fig.5.25

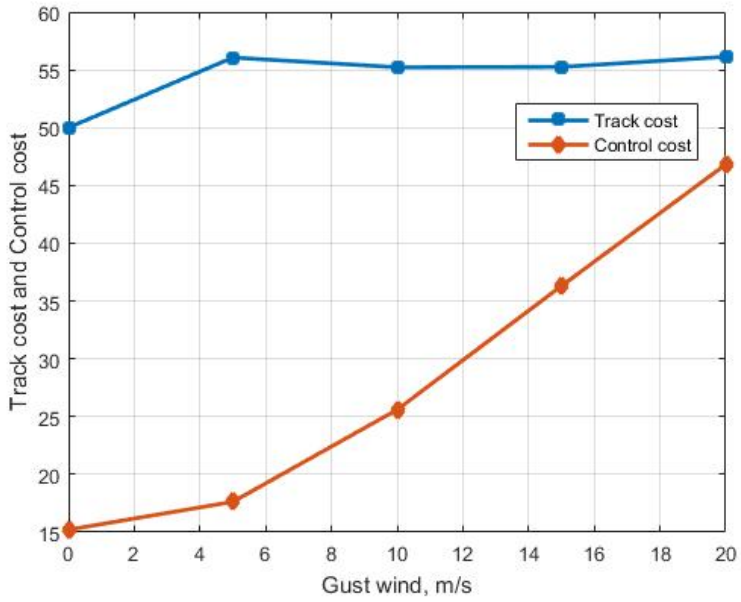


Figure 5.23: Track cost and control cost subject to crosswind

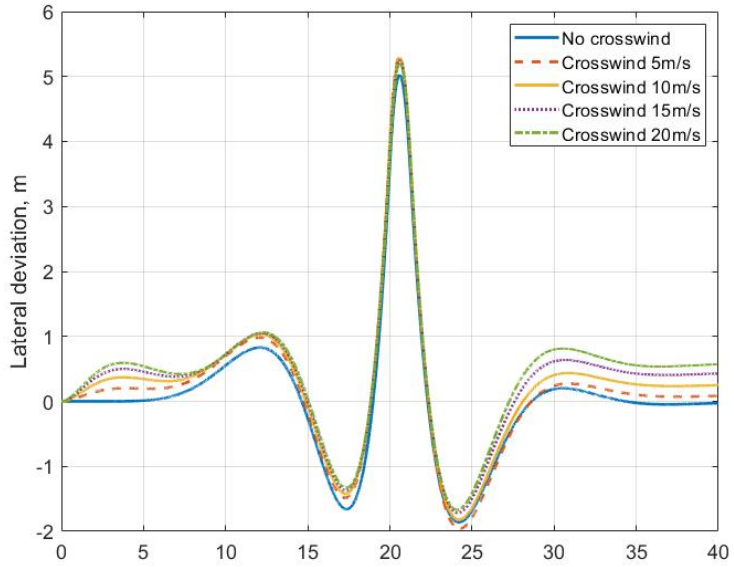


Figure 5.24: Lateral deviation subject to crosswind

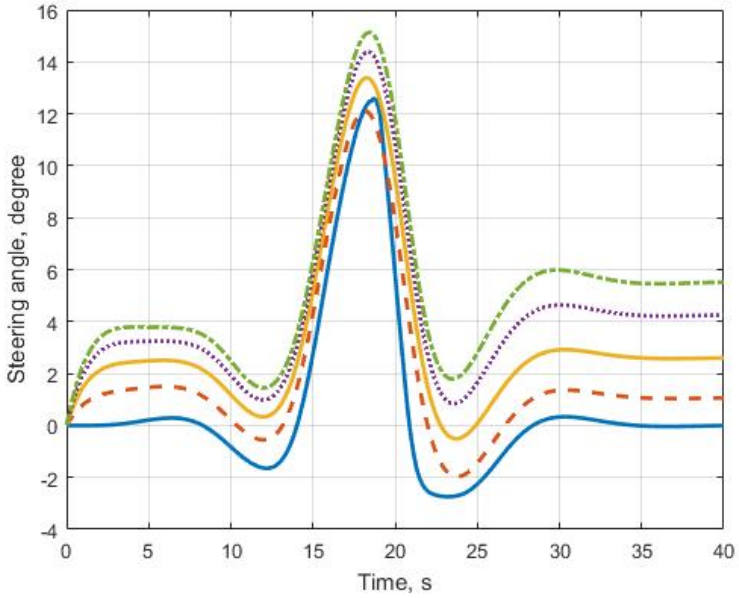


Figure 5.25: Lateral deviation and control input with gust wind

show the lateral deviation and steering input respectively. An extra amount of steering is applied to compensate the negative yaw moment caused by the crosswind. The controller shows good robustness in the presence of crosswind.

## 5.7 Concluding remarks

The presented Predictive Steering Control method can be employed to drive the aircraft to follow a target path. This proposed control law is computationally efficient so that it can be implemented in real-time. The proposed controller is studied when negotiating three generic runway geometries at a wide range of forward speeds. In comparison with a pilot model that represents an expert pilot's operation, PSC achieves better performance by using a linear quadratic method with look-ahead. Taking advantage of a 20s road preview, the controller starts to steer from a large distance prior to the corner. The aircraft takes a preview-oscillation steering strategy to build up an oscillatory yaw momentum such that the aircraft is able to turn more easily, following a larger turning radius. Additionally, PSC is compared with GOC which provides the numerically-optimal solution. The comparison shows that PSC is a near-optimal controller which is very close to the optimal solution. One of the biggest strengths of PSC is that it requires much less computational power such that it can be implemented in real-time.

To make PSC more compact and efficient, the interpolation between control gains for different lateral acceleration levels is replaced by a constant control gain sequence (PSCC). PSCC shows good effectiveness although it leads to a slightly increased track cost. A comprehensive robustness study has been carried out for PSCC with respect to uncertainties (mass, CG, and road conditions) and disturbances (crosswind). PSCC shows good robustness to uncertainty and disturbance under standard operational configurations and conditions. The presented control law mainly concerns lateral control with a constant forward speed. In practice, however, brakes and thrust can also be used to execute a manoeuvre. Future work could focus on longitudinal control

and optimization.

# Chapter 6

# Conclusion and outlook

## 6.1 Summary

The overall objective of this research is to improve the efficiency and security of airport operations via the automation of ground manoeuvres. A highly reliable and robust controller allows more stable and efficient ground manoeuvres than a pilot could achieve, reducing aviation incidents and increasing traffic capacity. In particular, we aim to identify a suitable control method to automate runway exit manoeuvres, especially high-speed runway turnoff; these manoeuvres are executed by following the centreline in different runway geometries. This work is focused on steering control, with the constant forward speed controlled by a PI controller. Three control methods are employed to address this problem: a linear pilot model EPM with single preview point, a numerical off-line optimal controller GOC, and a real-time near-optimal controller PSC.

This study makes contributions to the literature on control of aircraft ground manoeuvres in following ways. Firstly, the Expert Pilot Model is specifically designed for aircraft steering control on the ground, which limited research has been conducted on. The simple Proportional-Integral control algorithm based on steady-state prediction achieves better path following performance compared with average pilots. Secondly, the optimal control strategy

for runway exit manoeuvres is revealed for the first time by using Generalised Optimal Control. It provides a benchmark for controller design in the future. Thirdly, the proposed Predictive Steering Control (PSC) provides advantages over the original LQ controller via an extended prediction horizon of 20s based on steady-state handling equation. It is suitable for real-time implementation and able to achieve near-optimal solutions.

In Chapter 2, a fully parameterised nonlinear aircraft model is presented, providing accessibility to all the aircraft's states. A realistic combined slip tyre model is proposed with parameters chosen to represent nose and main landing gear respectively. The tyre model is able to capture the most important nonlinear effect, i.e. the tyre/ground friction force. Two mathematical tools, bifurcation analysis and dynamic simulation, are used to study aircraft ground dynamics. Bifurcation analysis provides a global picture of aircraft steady turning circle solutions with varied control inputs and operational parameters. The bifurcation diagrams illustrate how turning solutions change with thrust force and steering angle over various CG positions and runway conditions. In conjunction with bifurcation analysis, dynamic simulations are employed to investigate aircraft's transient behaviours when subject to a specific control input. This chapter proves that the proposed aircraft model is able to simulate realistic aircraft ground behaviours.

In Chapter 3, we present an Expert Pilot Model for aircraft steering control on the ground, which can be used to study manually operated ground manoeuvres by pilots. It is tuned to an expert level to investigate high-speed manoeuvres on the ground. This pilot model is developed on the basis of a simple realistic driver model which is initially developed for ground vehicles. It is based on a single preview point located by projecting along a steady turning circle, which is determined by the aircraft's current speed, steering angle, and understeer gradient. We improve the pilot model by an additional yaw rate control, which can significantly reduce over-corrections of the steering angle. The results show that EPM can be successfully used to automatically execute runway exit manoeuvres by following the centreline. It is tuned to represent

the best performance an expert pilot could achieve, and hence provides a lower benchmark for future controller development.

Conversely, in Chapter 4, we explore an upper benchmark for the controller. Generalised Optimal Control (GOC) is employed to numerically investigate the optimal solutions for aircraft runway exit manoeuvres, providing a way to evaluate the best possible effectiveness of a real-time controller. Since GOC is an iterative algorithm and requires calculations in reverse time, it is suitable for off-line investigation rather than real-time implementation. Three scenarios are investigated for the high-speed runway exit manoeuvre. In the case of following the centreline, the cost function is comprised of the track cost and final attitude cost. To investigate the time-optimal solution for fast runway exit manoeuvres, an additional cost component with respect to the final distance to a target point is employed. Consequently, the aircraft executes the runway exit by cutting the corner at high speed. Finally, the optimal control sequence in the case of minimum tyre wear is identified, where an additional cost associated with tyre wear is added to the cost function. This chapter proves that GOC is able to converge to the optimal control input that achieves the minimum of a specific cost function.

In Chapter 5, Predictive Steering Control can be employed to follow a target path. This proposed control law is computationally efficient, and hence suitable for real-time implementation. The proposed controller is studied when negotiating three generic runway geometries at a wide range of forward speeds. The aircraft takes a preview-oscillation steering strategy to achieve an oscillatory yaw momentum such that the aircraft is easy to turn, following a larger turning radius. PSC is a near-optimal controller which gets close to the optimal solution. To make PSC more compact and efficient, the interpolation between control gains for different lateral acceleration levels is replaced by a constant control gain sequence (PSCC). PSCC shows good effectiveness although it leads to a slightly increased track cost. Additionally, PSCC shows good robustness to uncertainty and disturbance under standard operational configurations and conditions.

## 6.2 Future work

A high fidelity aircraft model is able to capture accurate ground dynamics, however, it results in high complexity and heavy calculation burden. The aircraft model could be simplified by a reduction of the model's associated state space dimension or degrees of freedom, while preserving the properties and characteristics of the full order model as much as possible. In order to be applicable to real-world problems, an approximation of the original model, referred to as a reduced order model, is required to be computationally efficient and robust. Future research could consider development of reduced order models, as these would potentially enable alternative control strategies using on-line simulation and optimisation, with acceptable computational speed. The commonly used methods for Model Order Reduction (MOR) include projection-based MOR, e.g. Krylov methods and POD methods, and truncation-based MOR, e.g. Balanced Truncation, Poor Mans TBR and Modal Truncation.

In this research, the proposed controller PSC is focused on steering control, leaving the forward speed separately controlled at a constant level. A fixed forward speed, however, is not commonly considered in real-world operations. Indeed, brakes and thrust are also important to negotiate a specific ground manoeuvre, the efficiency of which could be further improved by the optimal control of forward speed. Taking advantage of a reduced order model, Model Predictive Control (MPC) might be used to optimise lateral and longitudinal behaviours simultaneously. The main advantage of MPC is the fact that it allows states at the current time to be optimized, while taking future time behaviours into account. This is achieved by optimizing a finite time-horizon, implementing the current time solution and then optimizing again repeatedly. It could be interesting to explore how MPC might optimise the control as an alternative to PSC.

Aircraft modelling is subject to uncertainties in the operational parameters, for example, as a result of fuel consumption its mass is decreasing and CG position is moving backward. A controller that could adapt to a system with

varying parameters potentially provides further advantages. A correction solution to catering for these uncertainties is to apply robust control techniques. Another alternative is to investigate adaptive control. Adaptive control is concerned with control law changing itself without the need for a priori information about the bounds on these uncertainties or time-varying parameters. Adaptive control methods, either model reference or self-tuning, usually require identification of the dynamics.

To implement the proposed controller in a real world application, there is a lot of future work to be done. The runway centreline needs to be extracted from sensors, and the delay caused by the sensors must be taken into account when designing a controller. This research is focused on runway exit manoeuvres. However, further control systems should cover the whole phase of taxiing from the runway to the gate. Therefore, a reliable collision avoidance system is desired especially for busy airports.

# References

[1] IATA. 2036 forecast reveals air passengers will nearly double to 7.8 billion. https://www.iata.org/pressroom/pr/Pages/2017-10-24-01.aspx, 2017.

[2] Aviation Safety Boeing Commercial Airplanes. Statistical summary of commercial jet airplane accidents. http://www.boeing.com/resources/boeingdotcom/company/about_bca/pdf/statsum.pdf, August 2015.

[3] IATA. Safety report 2014 51st ed. https://skybrary.aero/bookshelf/books/3049.pdf, April 2015.

[4] JM Biannic, A Marcos, M Jeanneau, and C Roos. Nonlinear simplified lft modelling of an aircraft on ground. In *2006 IEEE Conference on Computer Aided Control System Design, 2006 IEEE International Conference on Control Applications, 2006 IEEE International Symposium on Intelligent Control*, pages 2213–2218. IEEE, 2006.

[5] Matthieu Jeanneau. The airbus on-ground transport aircraft benchmark. In *Nonlinear Analysis and Synthesis Techniques for Aircraft Control*, pages 3–24. Springer, 2007.

[6] Dominique Brière and Pascal Traverse. Airbus a320/a330/a340 electrical flight controls-a family of fault-tolerant systems. In *FTCS-23 The Twenty-Third International Symposium on Fault-Tolerant Computing*, pages 616–623. IEEE, 1993.

[7] Christian Favre. Fly-by-wire for commercial aircraft: the airbus experience. *International Journal of Control*, 59(1):139–157, 1994.

[8] Pascal Traverse, Isabelle Lacaze, and Jean Souyris. Airbus fly-by-wire: a process toward total dependability. In *ICAS 2006, 25th International Congress of the Aeronautical Sciences*, 2006.

[9] Fabrice Villaumé. Brake-to-vacate system. *FAST44–flight, airworthiness, support, technology*, 44:17–25, 2009.

[10] Roland Lenain, Benoit Thuilot, Christophe Cariou, and Philippe Martinet. High accuracy path tracking for vehicles in presence of sliding: Application to farm vehicle automatic guidance for agricultural tasks. *Autonomous robots*, 21(1):79–97, 2006.

[11] Timm Faulwasser and Rolf Findeisen. Nonlinear model predictive control for constrained output path following. *IEEE Transactions on Automatic Control*, 61(4):1026–1039, 2016.

[12] Matthew OT Cole and Theeraphong Wongratanaphisan. Optimal lq feedforward tracking with preview: practical design for rigid body motion control. *Control Engineering Practice*, 26:41–50, 2014.

[13] RS Sharp and V Valtetsiotis. Optimal preview car steering control. *Vehicle System Dynamics*, 35(SUPPL. 1):101–117, 2001.

[14] Robin S Sharp. Optimal linear time-invariant preview steering control for motorcycles. *Vehicle system dynamics*, 44(sup1):329–340, 2006.

[15] Michael Blundell and Damian Harty. *Multibody systems approach to vehicle dynamics*. Elsevier, 2004.

[16] Ahmed A Shabana. *Dynamics of multibody systems*. Cambridge university press, 2013.

[17] Michel Géradin and Alberto Cardona. *Flexible multibody dynamics: a finite element approach*. John Wiley Chichester, England; New York, USA, 2001.

[18] Juan Carlo Garcia Orden, José M Goicolea, and Javier Cuadrado. *Multibody dynamics: Computational methods and applications*, volume 4. Springer Science & Business Media, 2007.

[19] Mathworks. Model and simulate mechanical systems with simmechanics. `http://www.mathworks.com/products/simmechanics/`, 2004.

[20] Prashant Dilip Khapane. Simulation of asymmetric landing and typical ground maneuvers for large transport aircraft. *Aerospace Science and Technology*, 7(8):611–619, 2003.

[21] Etienne Coetzee, Bernd Krauskopf, and Mark Lowenberg. Nonlinear aircraft ground dynamics. In *International Conference on Nonlinear Problems in Aviation and Aerospace*, pages 1–8, 2006.

[22] James Rankin, Bernd Krauskopf, Mark Lowenberg, and Etienne Coetzee. Operational parameter study of aircraft dynamics on the ground. *Journal of Computational and Nonlinear Dynamics*, 5(2):021007, 2010.

[23] Matthieu Jeanneau. Description of aircraft ground dynamics. *GARTEUR FM AG17, Paper No. RP0412731*, 2004.

[24] James Rankin, Etienne Coetzee, Bernd Krauskopf, and Mark Lowenberg. Bifurcation and stability analysis of aircraft turning on the ground. *Journal of guidance, control, and dynamics*, 32(2):500–511, 2009.

[25] Jo Yung Wong. *Theory of ground vehicles*. John Wiley & Sons, 2008.

[26] Fiala E. Seitenkrafte am rollenden luftreifen, vdi-zeitschrift 96, 973, 1954.

[27] Mechanical dynamics inc. adams/tire (6.1) users manual, mechanical dynamics inc. 2301 commonwealth blvd. michigan, usa: Ann arbor; october 1992.

[28] HB Pacejka. Tyre and vehicle dynamics/hans b. pacejka, 2006.

[29] Egbert Bakker, Lars Nyborg, and Hans B Pacejka. Tyre modelling for use in vehicle dynamics studies. Technical report, SAE Technical Paper, 1987.

[30] Egbert Bakker, Hans B Pacejka, and Lars Lidner. A new tire model with an application in vehicle dynamics studies. Technical report, SAE technical paper, 1989.

[31] Hans B Pacejka and Egbert Bakker. The magic formula tyre model. *Vehicle system dynamics*, 21(S1):1–18, 1992.

[32] G Wood, M Blundell, and S Sharma. A low parameter tyre model for aircraft ground dynamic simulation. *Materials & Design*, 35:820–832, 2012.

[33] Duane T McRuer. Human pilot dynamics in compensatory systems-theory, models, and experiments with controlled element and forcing function variations. *AFFDL-TR-65-15*, 1965.

[34] DT McRuer and ES Krendel. Mathematical models of human pilot behavior@, agard ag 188. *North Atlantic Treaty Organization: Advisory Group for Aerospace Research and Development*, 1974.

[35] Kirill Zaychik, Frank Cardullo, and Gary George. A conspectus on operator modeling: past, present and future. In *AIAA Modeling and Simulation Technologies Conference and Exhibit*, page 6625, 2006.

[36] Robert Heffley. Use of a task-pilot-vehicle (tpv) model as a tool for fight simulator math model development. In *AIAA Modeling and Simulation Technologies Conference*, page 7620, 2010.

[37] Rodney D Wierenga. An evaluation of a pilot model based on kalman filtering and optimal control. *IEEE Transactions on Man-Machine Systems*, 10(4):108–117, 1969.

[38] David L Kleinman, S Baron, and WH Levison. An optimal control model of human response part i: Theory and validation. *Automatica*, 6(3):357–369, 1970.

[39] John B Davidson and David K Schmidt. Modified optimal control pilot model for computer-aided design and analysis. 1992.

[40] M Anderson and D Doman. Fixed order optimal pilot models. In *AIAA guidance, navigation and control conference*, 1996.

[41] Ruud Hosman and Henk Stassen. Pilot's perception in the control of aircraft motions. *Control engineering practice*, 7(11):1421–1428, 1999.

[42] Myung-Wook Park, Sang-Woo Lee, and Woo-Yong Han. Development of lateral control system for autonomous vehicle based on adaptive pure pursuit algorithm. In *2014 14th International Conference on Control, Automation and Systems (ICCAS 2014)*, pages 1443–1447. IEEE, 2014.

[43] Ashwin Carvalho, Yiqi Gao, Andrew Gray, H Eric Tseng, and Francesco Borrelli. Predictive control of an autonomous ground vehicle using an iterative linearization approach. In *16th International IEEE Conference on Intelligent Transportation Systems (ITSC 2013)*, pages 2335–2340. IEEE, 2013.

[44] Yiqi Gao, Theresa Lin, Francesco Borrelli, Eric Tseng, and Davor Hrovat. Predictive control of autonomous ground vehicles with obstacle avoidance on slippery roads. In *ASME 2010 dynamic systems and control conference*, pages 265–272. American Society of Mechanical Engineers, 2010.

[45] Craig Earl Beal and J Christian Gerdes. Model predictive control for vehicle stabilization at the limits of handling. *IEEE Transactions on Control Systems Technology*, 21(4):1258–1269, 2012.

[46] Jesse Levinson, Jake Askeland, Jan Becker, Jennifer Dolson, David Held, Soeren Kammel, J Zico Kolter, Dirk Langer, Oliver Pink, Vaughan Pratt, et al. Towards fully autonomous driving: Systems and algorithms. In *2011 IEEE Intelligent Vehicles Symposium (IV)*, pages 163–168. IEEE, 2011.

[47] David H Weir and Duane T McRuer. A theory for driver steering control of motor vehicles. Technical report, 1968.

[48] W Riley Garrott, Douglas L Wilson, and Richard A Scott. Closed loop automobile maneuvers using describing function models. Technical report, SAE Technical Paper, 1982.

[49] Matthew C Best. Real-time characterisation of driver steering behaviour. *Vehicle system dynamics*, 57(1):64–85, 2019.

[50] Konghui Guo and Hsin Guan. Modelling of driver/vehicle directional control system. *Vehicle System Dynamics*, 22(3-4):141–184, 1993.

[51] Charles C MacAdam. Application of an optimal preview control for simulation of closed-loop automobile driving. *IEEE Transactions on systems, man, and cybernetics*, 11(6):393–399, 1981.

[52] Charles C MacAdam and Gregory E Johnson. Application of elementary neural networks and preview sensors for representing driver steering control behaviour. *Vehicle System Dynamics*, 25(1):3–30, 1996.

[53] RS Sharp, DANIELE Casanova, and P Symonds. A mathematical model for driver steering control, with design, tuning and performance results. *Vehicle system dynamics*, 33(5):289–326, 2000.

[54] Ali Y Ungoren and Huei Peng. An adaptive lateral preview driver model. *Vehicle system dynamics*, 43(4):245–259, 2005.

[55] Steven D Keen and David J Cole. Application of time-variant predictive control to modelling driver steering skill. *Vehicle System Dynamics*, 49(4):527–559, 2011.

[56] David J Cole. A path-following driver–vehicle model with neuromuscular dynamics, including measured and simulated responses to a step in steering angle overlay. *Vehicle system dynamics*, 50(4):573–596, 2012.

[57] Luzheng Bi, Mingtao Wang, Cuie Wang, and Yili Liu. Development of a driver lateral control model by integrating neuromuscular dynamics into the queuing network-based driver model. *IEEE Transactions on Intelligent Transportation Systems*, 16(5):2479–2486, 2015.

[58] CJ Nash and David James Cole. Modelling the influence of sensory dynamics on linear and nonlinear driver steering control. *Vehicle system dynamics*, 56(5):689–718, 2018.

[59] Eugene L Allgower and Kurt Georg. *Introduction to numerical continuation methods*, volume 45. SIAM, 2003.

[60] QIN Zhu and Mitsuaki Ishitobi. Chaos and bifurcations in a nonlinear vehicle model. *Journal of Sound Vibration*, 275:1136–1146, 2004.

[61] Zhaoheng Liu and Guy Payre. Global bifurcation analysis of a nonlinear road vehicle system. *Journal of Computational and Nonlinear Dynamics*, 2(4):308–315, 2007.

[62] Z Liu, G Payre, and P Bourassa. Nonlinear oscillations and chaotic motions in a road vehicle system with driver steering control. *Nonlinear Dynamics*, 9(3):281–304, 1996.

[63] Vincent Nguyen, Gregory Schultz, and Balakumar Balachandran. Lateral load transfer effects on bifurcation behavior of four-wheel vehicle system. *Journal of Computational and Nonlinear Dynamics*, 4(4):041007, 2009.

[64] Raman K Mehra and James V Carroll. Global stability and control analysis of aircraft at high angles-of-attack. Technical report, Scientific Systems INC Cambridge MA, 1979.

[65] Harry Kwatny, Jean-Etienne Dongmo, Bor-Chin Chang, Gaurav Bajpai, Murat Yasar, and Christine Belcastro. Aircraft accident prevention: Loss-of-control analysis. In *AIAA Guidance, Navigation, and Control Conference*, page 6256, 2009.

[66] Phanikrishna Thota, Bernd Krauskopf, and Mark Lowenberg. Modeling of nose landing gear shimmy with lateral and longitudinal bending and a non-zero rake angle. In *AIAA Modeling and Simulation Technologies Conference and Exhibit*, page 7099, 2008.

[67] Phanikrishna Thota, Bernd Krauskopf, and Mark Lowenberg. Interaction of torsion and lateral bending in aircraft nose landing gear shimmy. *Nonlinear Dynamics*, 57(3):455–467, 2009.

[68] P Thota. Nonlinear analysis of the influence of tyre inflation prressure on nose landing gear shimmy. In *AIAA Modeling and simulation technologies conference*, pages 10–13, 2009.

[69] Phanikrishna Thota, Bernd Krauskopf, and Mark Lowenberg. Multi-parameter bifurcation study of shimmy oscillations in a dual-wheel aircraft nose landing gear. *Nonlinear dynamics*, 70(2):1675–1688, 2012.

[70] Phanikrishna Thota, Bernd Krauskopf, and Mark Lowenberg. Bifurcation analysis of nose-landing-gear shimmy with lateral and longitudinal bending. *Journal of Aircraft*, 47(1):87–95, 2010.

[71] James Rankin, Bernd Krauskopf, Mark Lowenberg, and Etienne Coetzee. Nonlinear analysis of lateral loading during taxiway turns. *Journal of guidance, control, and dynamics*, 33(6):1708–1717, 2010.

[72] Etienne Coetzee. *Modelling and nonlinear analysis of aircraft ground manoeuvres*. PhD thesis, University of Bristol, 2011.

[73] Anil V Rao. A survey of numerical methods for optimal control. *Advances in the Astronautical Sciences*, 135(1):497–528, 2009.

[74] Matthias Gerdts. A survey on optimal control problems with differential-algebraic equations. In *Surveys in Differential-Algebraic Equations II*, pages 103–161. Springer, 2015.

[75] Oskar Von Stryk and Roland Bulirsch. Direct and indirect methods for trajectory optimization. *Annals of operations research*, 37(1):357–373, 1992.

[76] Nicola Dal Bianco, Enrico Bertolazzi, Francesco Biral, and Matteo Massaro. Comparison of direct and indirect methods for minimum lap time optimal control problems. *Vehicle System Dynamics*, pages 1–32, 2018.

[77] Lev Semenovich Pontryagin. *Mathematical theory of optimal processes*. Routledge, 2018.

[78] TJ Gordon and MC Best. A sequential dual model approach to lap optimisation. In *Proceedings of the 6th International Symposium on Advanced Vehicle Control (AVEC), Hiroshima, Japan*, pages 99–104, 2002.

[79] TJ Gordon and Matt C Best. On the synthesis of driver inputs for the simulation of closed-loop handling manoeuvres. 2006.

[80] Matt C Best. Optimisation of high-speed crash avoidance in autonomous vehicles. 2012.

[81] JPM Hendrikx, TJJ Meijlink, and RFC Kriens. Application of optimal control theory to inverse simulation of car handling. *Vehicle System Dynamics*, 26(6):449–461, 1996.

[82] Enrico Bertolazzi, Francesco Biral, and Mauro Da Lio. Symbolic-numeric efficient solution of optimal control problems for multibody systems. *Journal of computational and applied mathematics*, 185(2):404–421, 2006.

[83] Davide Tavernini, Matteo Massaro, Efstathios Velenis, Diomidis I Katzourakis, and Roberto Lot. Minimum time cornering: the effect of road surface and car transmission layout. *Vehicle System Dynamics*, 51(10):1533–1547, 2013.

[84] Davide Tavernini, Efstathios Velenis, Roberto Lot, and Matteo Massaro. The optimality of the handbrake cornering technique. *Journal of Dynamic Systems, Measurement, and Control*, 136(4):041019, 2014.

[85] Nicola Dal Bianco, Roberto Lot, and Marco Gadola. Minimum time optimal control simulation of a gp2 race car. *Proceedings of the Institution of Mechanical Engineers, Part D: Journal of Automobile Engineering*, 232(9):1180–1195, 2018.

[86] Christian Kirches, Sebastian Sager, Hans Georg Bock, and Johannes P Schlöder. Time-optimal control of automobile test drives with gear shifts. *Optimal Control Applications and Methods*, 31(2):137–153, 2010.

[87] Andreas Wächter and Lorenz T Biegler. On the implementation of an interior-point filter line-search algorithm for large-scale nonlinear programming. *Mathematical programming*, 106(1):25–57, 2006.

[88] Karl Berntorp, Bjrn Olofsson, Kristoffer Lundahl, and Lars Nielsen. Models and methodology for optimal trajectory generation in safety-critical roadvehicle manoeuvres. *Vehicle System Dynamics*, 52(10):1304–1332, 2014.

[89] Giacomo Perantoni and David J.N. Limebeer. Optimal control for a formula one car with variable parameters. *Vehicle System Dynamics*, 52(5):653–678, 2014.

[90] Paola Falugi, Eric Kerrigan, and Eugene Van Wyk. Imperial college london optimal control software user guide (iclocs), 2010.

[91] Michael A. Patterson and Anil V. Rao. Gpops-ii: A matlab software for solving multiple-phase optimal control problems using hp-adaptive gaussian quadrature collocation methods and sparse nonlinear programming. *ACM Trans. Math. Softw.*, 41:1:1–1:37, 2014.

[92] D.J.N. Limebeer, G. Perantoni, and A.V. Rao. Optimal control of formula one car energy recovery systems. *International Journal of Control*, 87(10):2065–2080, 2014.

[93] Mehdi Imani Masouleh and David JN Limebeer. Optimizing the aero-suspension interactions in a formula one car. *IEEE Transactions on Control Systems Technology*, 24(3):912–927, 2016.

[94] William F Milliken, Douglas L Milliken, et al. *Race car vehicle dynamics*, volume 400. Society of Automotive Engineers Warrendale, 1995.

[95] Arthur Earl Bryson. *Applied optimal control: optimization, estimation and control*. Routledge, 2018.

[96] Clive Marsh. *A nonlinear control design methodology for computer-controlled vehicle suspension systems*. PhD thesis, © C. Marsh, 1992.

[97] Alan G Veith. The most complex tire-pavement interaction: tire wear. In *The Tire Pavement Interface*. ASTM International, 1986.

[98] S Knisley. A correlation between rolling tire contact friction energy and indoor tread wear. *Tire science and Technology*, 30(2):83–99, 2002.

[99] N Louam, DA Wilson, and RS Sharp. Optimal control of a vehicle suspension incorporating the time delay between front and rear wheel inputs. *Vehicle system dynamics*, 17(6):317–336, 1988.

[100] G Prokop and RS Sharp. Performance enhancement of limited-bandwidth active automotive suspensions by road preview. *IEE Proceedings-Control Theory and Applications*, 142(2):140–148, 1995.

[101] Brian DO Anderson and John B Moore. *Optimal control: linear quadratic methods*. Courier Corporation, 2007.

# Publications

## Published

1. Huang, Z., Best, M.C. and Knowles, J.A., 2018. Numerical Investigation of Aircraft High-speed Runway Exit Using Generalized Optimal Control. In 2018 AIAA Guidance, Navigation, and Control Conference (p. 0879).

2. Huang, Z., Best, M. and Knowles, J., 2018. An investigation of a high-speed ground manoeuvre under optimal control. Proceedings of the Institution of Mechanical Engineers, Part G: Journal of Aerospace Engineering, p.0954410018821793.

3. Huang, Z., Best, M. and Knowles, J., 2018, October. Optimal Predictive Steering Control for Aircraft Ground Path Following. In 2018 International Conference on Control, Automation and Information Sciences (ICCAIS) (pp. 320-325). IEEE.

## Submitted:

1. Huang, Z., Best, M.C. and Knowles, J.A., Aircraft Autonomous Ground Manoeuvres Based on Optimal Predictive Steering Control. Submitted to Journal of Aerospace Engineering. Current status: under review.